Integrated LIDAR with Optical Phased Arrays in Silicon Photonics

by

Christopher Vincent Poulton

B.S., University of Colorado Boulder (2014)

Submitted to the
Department of Electrical Engineering and Computer Science
in partial fulfillment of the requirements for the degree of

Master of Science in Electrical Engineering and Computer Science

at the

MASSACHUSETTS INSTITUTE OF TECHNOLOGY

September 2016

© Massachusetts Institute of Technology 2016. All rights reserved.

Author . . . .
Department of Electrical Engineering and Computer Science
August 31, 2016

Certified by . . . .
Michael R. Watts
Associate Professor
Thesis Supervisor

Accepted by . . . .
Leslie A. Kolodziejski
Chair, Department Committee on Graduate Students

Integrated LIDAR with Optical Phased Arrays in Silicon Photonics

by

Christopher Vincent Poulton

Submitted to the Department of Electrical Engineering and Computer Science
on August 31, 2016, in partial fulfillment of the
requirements for the degree of
Master of Science in Electrical Engineering and Computer Science

Abstract

Light detection and ranging (LIDAR) has become an ubiquitous ranging technology. LIDAR systems are integral to almost all autonomous vehicles and robotics. Most LIDAR systems today use discrete free-space optical components and utilize a mechanical apparatus for beam steering. Apart from the relative high cost of the system, this mechanical apparatus limits the scan rate of the LIDAR system while increasing both size and complexity. This leads to concerns about long-term reliability, especially in harsh environments.

In this thesis, the design and experimental results of an integrated chip-scale frequency-modulated continuous-wave LIDAR system are presented. This system has the capability of measuring both distance and velocity simultaneously with a 20 mm resolution and a 2 m range. Its functionality is then extended by utilizing optical phased arrays as a transmitter and receiver for solid-state beam steering. The phased array utilized has a grouped cascaded phase shifter architecture and is shown to have a steering range of $46° \times 36°$. This is the first integrated coherent LIDAR system based on optical phased arrays.

In order to have a viable LIDAR system with optical phased arrays, high beam powers and large aperture sizes are needed. A silicon nitride distribution network is used to enable high on-chip power because of the low material nonlinearities. An ultra-high main beam power of 520 mW is reported. A phased array is demonstrated with an ultra-large aperture size of $4 \times 4\,\mathrm{mm}^2$, achieving a record-small and near diffraction limited spot size of $0.021° \times 0.021°$ with a side lobe suppression of 10 dB. This is the largest optical phased array to date by an order of magnitude and shows the scalability of optical phased arrays. Finally, an optical phased array at a visible wavelength of 635 nm is shown with an aperture size of $0.5 \times 0.5\,\mathrm{mm}^2$ and a spot size of $0.064° \times 0.074°$. This demonstration moves large-scale integrated photonics into the visible spectrum and has potential applications in bathymetric LIDAR.

Thesis Supervisor: Michael R. Watts
Title: Associate Professor

Acknowledgments

I first want to thank my advisor, Prof. Michael Watts, who has given me the opportunity to work on this extremely impactful project in a growing field. There were always resources to make it better, including expensive equipment and dedicated fabrication runs, and for that I am extremely thankful. The mixture of academic freedom and practical pressure I have been given has allowed me to grow to be an independent researcher.

I also want to thank Dr. Joshua Conway, the DARPA program manager for this project, for his technical and funding support throughout the project. I am humbled to be his DARPA Riser and grateful that we were included in the DARPA Demo Day. It's been a wonderful experience being involved in the larger DARPA community.

Manan Raval has been one of my best friends in Boston that has not only been a person to bounce ideas off, but also to talk to during the bad times that occurred during this work. He has been extremely supportive and I've enjoyed the many nights at Lord Hobo talking about photonics, the lab, and life in general.

In addition, I want to thank Matthew Byrd for the all of his design and experimental effort that helped propel this work, specifically on the silicon nitride based devices. Much of it would not have been possible without him. It was a wonderful experience to mentor him in the beginning and see him grow into one of the best photonic designer and experimenter I've ever met.

Diedrik Vermeulen was crucial for the success of the demo of this work at the DARPA Demo Day. Without his device packaging knowledge and effort, there might not have been a demo. The many late nights we had in the lab gluing fibers to chips will not be a memory I will forget, for better or for worse.

It's been an honor to continue Ami Yaacobi's Ph.D work, and his initial teachings on phased arrays allowed for this thesis to be written. His personality is greatly missed in the lab. Dave Cole was also monumental in getting the first on-chip LIDAR measurement that took this work off the ground.

The general day-to-day mentorship of Zhan Su and Erman Timurdogan taught

me the technical details of so many different aspects in silicon photonics in the past two years. I thank them both for all of their time and dedication. Because of them, I feel that I have the knowledge to excel at almost anything in silicon photonics.

Finally, I want to thank my parents, Susie and Jonathan Poulton, who sacrificed so much to allow for me to be here, and my brother, Matthew Poulton, who will always be my number one bro. I love you guys, this thesis is dedicated to you.

Contents

1 Introduction 17

1.1 Background on LIDAR 17

1.2 LIDAR with Optical Phased Arrays 20

1.2.1 Phased Array Mathematics and Basic Concepts 22

1.3 Overview of Thesis 29

2 LIDAR on a Chip 31

2.1 Device and FMCW LIDAR Overview 31

2.2 Balanced Photodetector 33

2.3 Laser Diode Characterization 36

2.4 Experimental Results 38

2.4.1 Homodyne Doppler Measurements 38

2.4.2 Stationary Target Measurements 39

2.4.3 Moving Target Measurements 40

2.5 Conclusion 41

3 Grouped Cascaded Phased Array for Integrated LIDAR 43

3.1 Phased Array Design 43

3.1.1 Grouped Cascaded Phase Shifters 43

3.1.2 Phase Shifter and Splitter Design 45

3.1.3 Antenna Design 47

3.2 Experimental Results 50

3.2.1 Phased Array Characterization 50

3.2.2 LIDAR System with Phased Array 53
3.3 Conclusion 55

4 High Power Silicon Nitride Phased Arrays 57
4.1 Splitter Design 58
4.2 Antenna Design 61
4.2.1 Mono-Layer Antenna Design 61
4.2.2 Dual-Layer Antenna Design 64
4.3 Experimental Results 67
4.3.1 Splitter Results 67
4.3.2 Uni-Directional Antenna Results 68
4.3.3 Phased Array Results 70
4.4 Conclusion 73

5 Ultra-Large-Scale Passive Phased Arrays 75
5.1 Ultra-Large Silicon Phased Arrays 76
5.2 Ultra-Large Silicon Nitride Phased Arrays 78
5.3 Conclusion 81

6 Phased Arrays for Visible Light Applications 83
6.1 On-Chip Coupling and Routing Waveguides 85
6.2 Visible Splitters and Antennas 86
6.3 Experimental Results 89
6.4 Conclusion 92

7 Thesis Conclusion 93

List of Figures

1-1 Point cloud from a single scan of a Velodyne HDL-64 LIDAR module. From [5]. 18
1-2 (a) Internal and (b) external view of a Velodyne HDL-64E LIDAR module. From [10]. 20
1-3 (a-f) Overview of notable optical phased array systems. From [16–21]. 21
1-4 (a) The phase distribution of three different α values. (b) The array factors for the three different α values showing steering with a change of α. 23
1-5 (a) The array factors for different antenna pitch values. (b) Maximum steering range of a phased array as a function of antenna pitch. . . . 24
1-6 (a) Example optical phased array antenna based on a long silicon waveguide grating. (b) Element factor, $E(\theta, \phi)$, of the antenna. 25
1-7 Schematic of a (a) tree and (b) cascaded phase shifter architecture for one-dimensional phased arrays. 27
1-8 (a) Thermal phase shifter. From [32]. (b) Illustration of a silicon rib waveguide with vertical PN and measured data of the PN junction. . 28

2-1 (a) Illustration of the effective device consisting of silicon photonic chip with collimating lens. Full device described in [38]. (b) Concept of frequency-modulated continuous-wave LIDAR with triangular modulation. 32
2-2 Layout rendering of the balanced photodetector consisting of an adiabatic coupler and two germanium photodetectors. 33

2-3 (a) Measured response of a single adiabatic coupler. (b) Measured photodetector responsivity. 35

2-4 (a) Measured laser diode frequency as a function of injection current. (b) Back-calculated current ramp to produce a linear frequency sweep. 36

2-5 Example of time gating the photodetector signal to reduce the effects of the transients. 37

2-6 Experimental setup utilizing a 1.5 m motion track. 38

2-7 (a) Concept of homodyne Doppler measurements. (b) Experimental results of the homodyne Doppler measurements with a theoretical line of the speed dependent Doppler shift. (c) Speed error of the data set in (b). 38

2-8 (a) Measured beat frequency at various stationary target distances at 10 mm intervals. (b) Fourier transform of time domain data in (a) showing resolved frequency peaks. (c) Distance error of the measurements shown in (a). 39

2-9 (a) Measured beat frequencies for a moving target while sweeping velocity and distance. (b) Calculated velocity of the data set in (a), black lines show actual velocity. (c) Raw time domain data of the 0.5 m target measurements at four different velocities. 40

2-10 Error of calculated target (a) distance and (b) velocity of the data set in Fig. 2-9(a). 41

3-1 (a) Schematic of a grouped cascaded phase shifter architecture with three groups. (b) Concept of sub-phased arrays formed by a grouped architecture showing the ability to create multiple beams. 44

3-2 (a) Layout of cascaded phase shifters with alternating directional couplers. Inset shows FDTD simulation of the adiabatic bend. (b) FDTD simulation of power coupling as a function of coupling length. 46

3-3 (a) Rendering of a portion of a full etch based antenna. (b) Perturbation strength as a function of perturbation distance. 47

3-4 (a) Perturbation distance needed throughout the antenna to produce uniform emission. (b) Grating pitch needed as a function of perturbation distance for straight up emission at $\lambda = 1550\,\text{nm}$. 49

3-5 (a) 3D rendering of the optical phased array. SEM images of the (b) cascaded phase shifter architecture, (c) close-up of the thermal phase shifters, and (d) the full etch silicon grating based antennas with waveguide width of 400 nm and pitch of $2\,\mu$m. 50

3-6 (a) Near field of the array. (b) Far field of the array when the three phase shifter groups act as three phased sub-arrays, (c) as two phased sub-arrays, (d) as a single phased array. (e) Close up of the far field spot. (f-g) Intensity cuts of the far field spot indicated in (e). 51

3-7 (a) Far field of the array at different thermal and wavelength tuning values. (b) Main beam and grating lobe output of the array seen with an IR card. (c) Free-space data link created with the phased array as a transmitter and a photodetector placed 1 m away. 52

3-8 (a) Schematic of the on-chip LIDAR system with transmitting and receiving phased arrays. (b) Optical micrograph of LIDAR system. (c) Chiplet containing LIDAR system on top of a dime. (d) Packaged LIDAR system that was demonstrated at the 2016 DARPA Demo Day. 53

3-9 (a) Image of targets in the lab placed at different angles away from the chip. (b) Ranging results of each target. (c) Raw photodetector data for each target. 55

4-1 (a) 3D rendering of a silicon nitride MMI splitter showing critical dimensions. (b) EME simulation of the electric field intensity throughout the splitter. (c) FDTD simulation results of the silicon nitride MMI splitter. 59

4-2 (a) 3D rendering of the small silicon nitride MMI splitter in the final splitter tree stage. (b) FDTD simulation results of the small silicon nitride MMI splitter. 60

4-3 (a) Layout of a six-layer tree to a 4 μm antenna pitch. (b) Close-up of the last two stages showing the use of the small MMI. 61

4-4 (a) Cross-section of silicon nitride waveguide mode. (b) Illustration of mono-layer nitride antenna. (c) Needed perturbation pitch for upwards emission as a function of perturbation. (d) Antenna strength as a function of perturbation. 62

4-5 (a) FDTD domain of a small test antenna with one source plane and three DFT planes. (b) Far field of the antenna emission. 63

4-6 (a) Rendering of a uni-directional antenna showing the two offset silicon nitride layers. (b) Uni-directionality of the antenna as a function of horizontal offset. 64

4-7 (a) Single period of the dual-layer antenna with fixed dimensions labeled. (b-e) Cross-sections throughout the antenna period with relevant effective indices. (f) Eigenmode solver results of the effective indices as a function of perturbation. 65

4-8 Far field in the (a) upwards and (b) downwards direction of 16 periods of the 100 nm perturbation uni-directional antenna. 66

4-9 (a) Illustration of an unbalanced tree used to measure the MMI splitter insertion loss. (b) Optical micrograph of fabricated unbalanced tree. (c) Experimental measurements showing an MMI insertion loss of 0.36 dB for the small MMI. 67

4-10 Measured (a) small and (b) large nitride MMI splitter efficiency as a function of wavelength using the cutback method. 68

4-11 (a) Illustration showing how reflections within the silicon substrate causes multiple paths that interfere in the far field. (b) Simulated far field of a point source showing the rings caused by the interference of the multiple paths. From [48]. (c-d) Measured far fields of a mono-layer bi-directional individual antenna and a dual-layer uni-directional individual antenna. (e) Near field of an individual 1 mm-long uni-directional antenna. 69

4-12 (a) Optical micrograph of the $500 \times 264\,\mu\text{m}^2$ silicon nitride array. (b) Image of phased array chiplet on top of a dime. (c) Image of the packaged phased array chiplet that was demonstrated at the 2016 DARPA Demo Day. 70

4-13 (a) Output beams of the phased array. (b) Near field and (c) far field of the silicon nitride phased array. (d-e) Vertical and horizontal intensity cuts of the far field. 72

5-1 Beam size after 30 m of propagation as a function of aperture size. . 76

5-2 (a) Image of the silicon $4 \times 4\,\text{mm}^2$ phased array next to a quarter. (b) Optical micrograph of the same phased array with epoxied input fiber. 77

5-3 (a) Near field and (b) far field of the silicon $2 \times 2\,\text{mm}^2$ phased array. (c) Far field intensity cuts in the array and antenna dimensions. . . . 78

5-4 (a) Image of the silicon nitride $4 \times 4\,\text{mm}^2$ phased array on top of a quarter. (b) Optical micrograph of the same phased array. 79

5-5 (a) Photograph of the main beam of the silicon nitride $4 \times 4\,\text{mm}^2$ array on an IR card. (b) Main beam intensity measurement after approximately 0.05 m and (c) 10 m propagation. Insets show Fresnel propagation simulations in the same domain. 79

5-6 (a) Far field of the main beam of the silicon nitride $4 \times 4\,\text{mm}^2$ phased array on a log scale. (b) Far field intensity cuts of the phased array along the array, θ, and antenna, ϕ, dimensions. 80

6-1 Sellmeier fit of the index of refraction of the silicon nitride used in this process. 84

6-2 Eigenmode simulations of a single layer silicon nitride waveguide as a function of width for (a) red - 635 nm, (b) green - 532 nm, and (c) blue - 445 nm. 86

6-3 FDTD simulation of the efficiency of the (a) red, (b) green, and (c) blue MMI 1×2 splitters. 87

6-4 Far fields of the (a) red, (b) green, and (c) blue antennas. 88

6-5 (a) Image of the red phased array with input light. (b) Non-saturated image of the near field. (c) Output of the red phased array on a white piece of paper. (d) Far field image. 89

6-6 (a) 3D image of $0.5{\times}0.5\,\mathrm{mm}^2$ red array far field spot. Cuts of the far field spot in the (a) array and (b) antenna dimensions. 90

List of Tables

6.1 Parameters of the designed visible antennas. 88

Chapter 1

Introduction

1.1 Background on LIDAR

Light detection and ranging (LIDAR) is a ranging technology based on light. It is similar to radio detection and ranging (RADAR), but utilizes the optical portion of the electro-magnetic spectrum instead of radio waves. This allows for a much higher ranging resolution because optical wavelengths are around 100,000 times smaller than radio waves. Because of this high resolution, applications such as robotics [1] and autonomous vehicles [2] rely heavily on LIDAR technology. LIDAR is also used in applications such as aerial mapping [3] and target tracking [4]. The range of current high-end LIDAR systems is around 100 m with a longitudinal resolution on the order of a centimeter. The angular resolutions are around 0.1°. Millions of points can be ranged in a second while scanning the field-of-view. Fig. 1-1 shows an example point cloud that arises from scanning and ranging the field-of-view of a LIDAR system that is atop a vehicle (from [5]).

LIDAR detection methods of can be split up into two major categories: time-of-flight (TOF) and coherent detection methods. TOF detection methods normally involve transmitting a pulse of light and then directly detecting the time needed for the light to reflect off a target and return back to the receiver module of the LIDAR system. This requires high speed electronics since the TOF timing must be precise. For example, light travels about 0.33 m in 1 ns so GHz speed electronics are necessary.

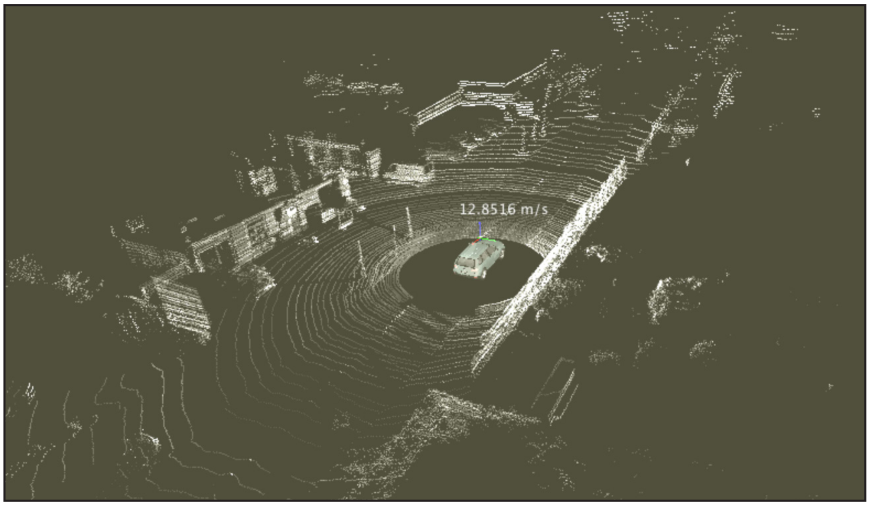

Figure 1-1: Point cloud from a single scan of a Velodyne HDL-64 LIDAR module. From [5].

Coherent detection methods differ from TOF methods in that they coherently beat the received signal with a local oscillator (LO). Frequency-modulated continuous-wave (FMCW) is a commonly used coherent detection method in both RADAR [6] and LIDAR [7] and is what is utilized in this work. In this method, a low-speed beat frequency that is proportional to the distance of the target is measured instead of the direct TOF. More detail on FMCW LIDAR can be found in Sec. 2.1.

A major difference between TOF and coherent detection methods is the resulting signal power. The received power that returns back to the system can be estimated by assuming that when the pulse reflects off a target, it scatters isotropically. This can be modeled by the equation

$$P_{RX} = P_{TX} \frac{\rho A_{RX}}{4\pi R^2} \tag{1.1}$$

where P_{RX} is the power of the received light, P_{TX} is the power of the transmitted light, ρ is the reflectivity of the target, A_{RX} is the area of the receiver, and R is the distance from the target to the receiver. The TOF methods directly measure this received power which can be very low. Because of this, Geiger mode avalanche photodiodes (APD) or photomultiplier tubes (PMT) are used [8,9]. However, for coherent detection methods, this received signal is first beaten with a LO which increases the signal power. Since it is coherent, the power that is observed is proportional to $\sqrt{P_{RX}P_{LO}}$, where P_{LO} is the power of the LO. This signal boost from the local oscillator can allow for the use of conventional photodetectors.

Another notable difference between TOF and coherent detection methods is the effect of cross-talk from other sources, e.g. ambient light or possibly nearby LIDAR systems. Since pulsed TOF LIDAR utilizes high-gain photodetectors and looks for any received light, it is difficult for the system to know if the received signal is the reflection of the transmitted pulse. Therefore, light from nearby sources can trigger the detection routines, which results in cross-talk. On the other hand, coherent detection methods will only receive a significant signal if the received light is coherent with the local oscillator. Effectively, this means that outside light sources are rejected when the coherent beating occurs between the received signal and the local oscillator since their signal contributions are not boosted and are negligible.

Current LIDAR systems rely on rotating the device in order to scan the field-of-view in one dimension (normally horizontal). Mechanical rotation can allow for a full 360° scan. However, this mechanical rotation requires a bulky apparatus that is not intrinsically robust to harsh environments that may induce vibrations, such as an off-road vehicle. Furthermore, mechanical rotation limits the scan rate to tens of Hz. In order to scan in the other dimension (normally vertical), multiple laser sources emitting at different angles are commonly used. Though a simple solution, many laser sources (∼10–64) are needed to give an adequate field-of-view with high resolution. Fig. 1-2(a) shows the internals of a high-end LIDAR system, the Velodyne HDL-64E, and Fig. 1-2(b) shows a photograph of the LIDAR system (from [10]).

A wavelength of 905 nm is commonly used in pulsed LIDAR systems. This is for a variety of reasons. First, 905 nm has relatively good transmission through the atmosphere. Second, inexpensive laser diodes with high power outputs are available at this wavelength along with efficient silicon avalanche photodiodes. However, 905 nm is not necessarily eye safe. Currently LIDAR manufacturers mention that since the device is scanning, it is Class 1 safe, but it is unclear how safe these systems are when they are not scanning. The LIDAR devices in this work utilize light with an eye safe

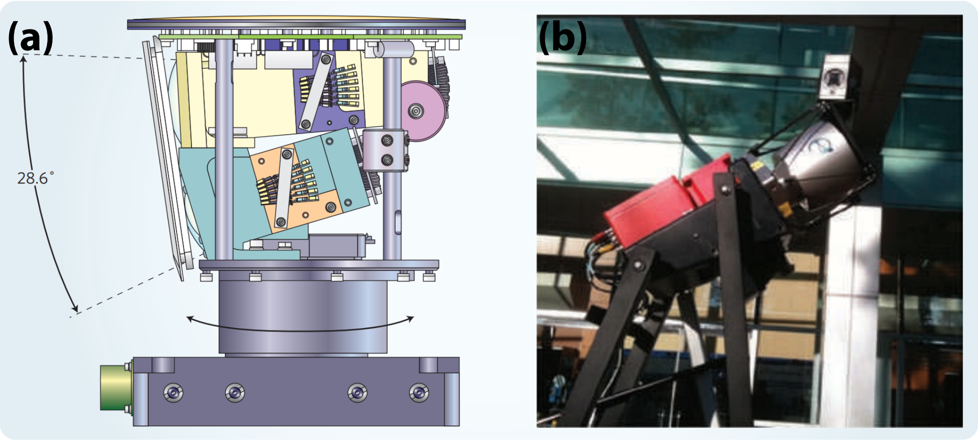

Figure 1-2: (a) Internal and (b) external view of a Velodyne HDL-64E LIDAR module. From [10].

wavelength of 1550 nm. 1550 nm was also chosen because silicon is transparent at this wavelength and germanium can be used as a detector. There are also inexpensive sources and other optical components at 1550 nm due to its use in telecom.

1.2 LIDAR with Optical Phased Arrays

At the moment, there is a need for a low-cost small-scale solid-state (non-mechanical) LIDAR. Silicon photonics promises a viable path to reduce the cost and form factor of LIDAR systems. The primary application of silicon photonic technology has been data communication. A plethora of work has been done on silicon photonic optical modulators and optical data links [11–15]. This work has led to silicon photonics being at the forefront of a new generation of data communication transceivers.

During the advancement of commercial large-scale silicon photonics foundry processes for data communication applications [22, 23], there has also been the development of nanophotonic optical phased arrays. Phased arrays are devices that comprise of an array of antennas. The antenna amplitudes and phases are controlled in order to generate arbitrary shaped emitted radiation patterns due to interference. Phased arrays at radio frequencies have been utilized for decades and have applications in data communication [24], astronomy [25], and RADAR [26]. Electronic phased arrays are considered to be the de facto way to do solid-state electronic beam steering for

RADAR systems and have a rich history [27]. Phased arrays at optical frequencies were first brought to silicon photonics in 2009 by Prof. Roel Baets's group at Ghent University [16]. This work actually demonstrated many of the common aspects we see in nanophotonic optical phased arrays today, including long gratings as antennas and both thermal and wavelength steering. Since 2009, there has been a variety of innovations in the silicon photonic optical phased array field. Large-scale two-dimensional phased arrays with complex radiation patterns have been shown [17]. A high-performance optical phased array created within a hybrid III/V platform with an on-chip laser and optical amplifiers was demonstrated [18]. Monolithic two-dimensional optical phased arrays have been realized in a commercial CMOS fabrication process driven by CMOS electronics on a single monolithic chip [19]. A phased array based on high-speed phase shifters for projection applications was demonstrated [20]. Finally, ultra-large-angle beam steering of has been achieved with a small spot size [21]. Images of these phased arrays are shown in Fig. 1-3(a-f).

As seen from these examples, the field of optical phased arrays is starting to focus on the system level and their use seems like an elegant solution to a solid-state LIDAR system. The usage of standard 300 mm wafer CMOS foundries that silicon photonic

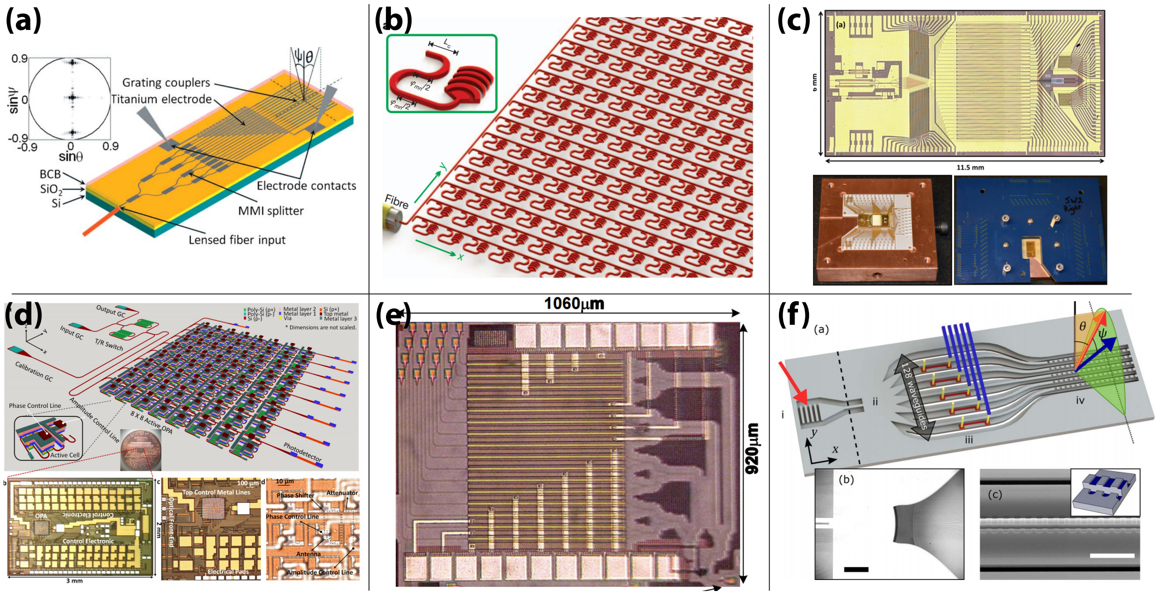
(a)
0.9
sinψ
0
-0.9
-0.9
0
0.9
sinθ
ψ
θ
Grating couplers
Titanium electrode
BCB
SiO$_2$
Si
Electrode contacts
MMI splitter
Lensed fiber input
(b)
L_c
Fibre
y
x
(c)
(a)
11.5 mm
(d)
Output GC
Input GC
T/R Switch
Calibration GC
Phase Control Line
Amplitude Control Line
8 x 8 Active OPA
Photodetector
Active Cell
3 mm
(e)
1060μm
920μm
(f)
(a)
i
ii
iii
iv
θ
ψ
y
x
(b)
(c)

Figure 1-3: (a-f) Overview of notable optical phased array systems. From [16–21].

technology currently utilizes [28] can reduce the production cost of individual chips to under \$10, making LIDAR systems commercially viable for a range of applications. By combining steerable optical phased arrays with on-chip lasers [29,30] and on-chip photodetectors [31], a stand-alone chip-sized LIDAR system can be realized and is the ultimate vision of this work.

1.2.1 Phased Array Mathematics and Basic Concepts

In order to understand the operation of a phased array, the mathematics of a one-dimensional optical phased array, and the basic terms and ideas used throughout this thesis will be covered in this section. A one-dimensional phased array is comprised of an array of N antennas placed along a line (z-axis in spherical coordinates $\{r,\theta,\phi\}$) at location r_n that have an individual phase, ψ_n, and field amplitude, A_n. Assuming that we are observing the emission pattern of such an array from the far field and individual emission patterns of each antenna look similar and can be described by a single function, $E(\theta,\phi)$, the emitting electric field of a phased array can be expressed as

$$E_{tot}(\theta,\phi) = \sum_{n=0}^{N-1} e^{jkr_n\cos\theta}(A_n e^{j\psi_n}E(\theta,\phi)) = E(\theta,\phi)\sum_{n=0}^{N-1} A_n e^{j(kr_n\cos\theta+\psi_n)} \tag{1.2}$$

where $k = 2\pi/\lambda$. The $E(\theta,\phi)$ portion of this equation is called the *element factor* of the array and is determined by the emission pattern of a single antenna. The term in the sum is called the *array factor* which is the effect of arraying the antennas. If we assume that we have a uniform linear array with fixed spacing, d, and uniform amplitude, then Eq. (1.2) can be simplified to

$$E_{tot}(\theta,\phi) = E(\theta,\phi)\sum_{n=0}^{N-1} e^{j(nkd\cos\theta+\psi_n)} \tag{1.3}$$

Finally, if we assume a linearly progressive phase from element to element, α, we get

$$E_{tot}(\theta,\phi) = E(\theta,\phi)\sum_{n=0}^{N-1} e^{jn(kd\cos\theta+\alpha)} = E(\theta,\phi)\frac{e^{jN(kd\cos(\theta)+\alpha)}-1}{e^{j(kd\cos(\theta)+\alpha)}-1} =$$
$$E(\theta,\phi)e^{j(N-1)(kd\cos(\theta)+\alpha)/2}\frac{\sin(N(kd\cos(\theta)+\alpha)/2)}{\sin((kd\cos(\theta)+\alpha)/2)} \tag{1.4}$$

The exponential term of Eq. (1.4) is only a phase factor and is unity if the array is centered at the origin. Therefore, we are left with only the $sinc()$-like function as the array factor. The first thing to note from this $sinc()$ function is that it does have a maximum point where a beam is created in the far field by the phased array. The physical reason that a beam is created by an array of antenna elements is that the emitted radiation constructive interferes only at certain angles. At other angles, it destructively interferes, and no light is observed. This is independent of the emission pattern of the antenna as seen by the factoring of the element and array factors. The second point about this equation is that its maximum location depends on the linear phase difference, α, between the antennas. The maximum of this equation is when $\sin((kd\cos(\theta)+\alpha)/2) = 0$, which occurs when $\theta = \cos^{-1}(\frac{\lambda}{2\pi d}(-\alpha \pm 2\pi m))$, where m is an integer. Thus, by changing α, we are changing the θ at which the array factor has a maximum and physically steering a beam in the θ direction. Fig. 1-4(a-b)

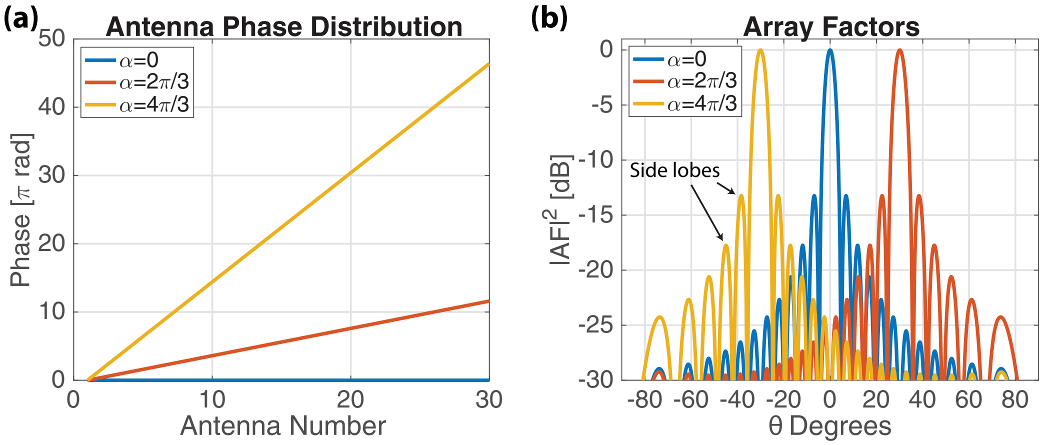

Figure 1-4: (a) The phase distribution of three different α values. (b) The array factors for the three different α values showing steering with a change of α.

shows the array factor of a 30-antenna phased array with a $d = 0.4\lambda$ for three different values for α. The beam created by the phased array is steered with the change of α. As expected from the *sinc*() relationship, there are small *side lobes* on each beam.

Finally, the relationship $\theta = \cos^{-1}(\frac{\lambda}{2\pi d}(-\alpha \pm 2\pi m))$ can have multiple solutions since m can be any integer. Physically, this causes additional beams, also called *grating lobes* or higher-order beams, to be emitted from the phased array. These beams are suppressed when the antenna spacing (or pitch), d, is less than 0.5λ. When this is the case, only a single solution to $\theta = \cos^{-1}(\frac{\lambda}{2\pi d}(-\alpha \pm 2m\pi))$ exists that occurs when $m = 0$. As an example, the array factors for a 30-antenna phased array with different pitches are shown in Fig. 1-5(a). At every pitch increase of λ, two additional beams, one on each side, are created.

By having additional beams, power is radiated from the phased array in multiple directions which is undesirable for many applications such as ranging and data communication. Furthermore, since the additional beams are effectively aliases, the steering range of the phased array is limited because there is no benefit in steering beyond the spacing of two consecutive beams. Fig. 1-5(b) shows the full angle steering range of a phased array as a function of the pitch of the antennas. Only at pitches that are less than 0.5λ is a full steering range of 180° achieved. Even at a pitch of λ, only a steering range of 60° is possible. For optical phased arrays, this is currently

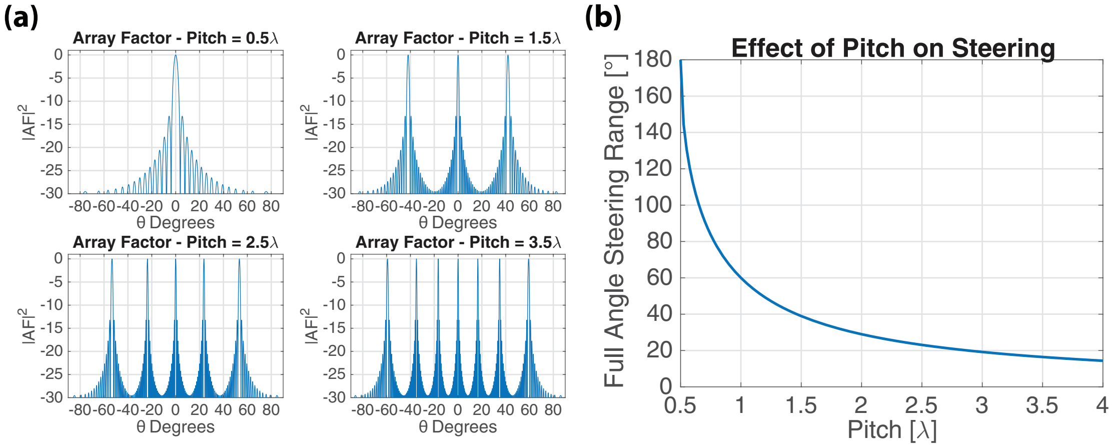

Figure 1-5: (a) The array factors for different antenna pitch values. (b) Maximum steering range of a phased array as a function of antenna pitch.

a very limiting factor. Since standard 220 nm height silicon waveguides are ~400 nm wide and have to be placed ~1 μm apart to minimize evanescent cross-talk, the pitch is limited to about λ at 1550 nm. The largest steering range shown with an optical phased array with uniform pitch (as described in this analysis) is 51° with a pitch of $2.0\,\mu\text{m} = 1.3\lambda$ [32]. Utilizing a non-uniform pitch can result in an increase of steering range but with an inherent loss of transmission power in the main beam. This was demonstrated in [21] to achieve a steering range of 80°.

The array factor in Eq. (1.4) is only a function of θ and not a function of ϕ. This is expected since the one-dimensional array acts as a one-dimensional aperture and can only confine light in a single dimension. In order to collimate light in the other dimension, the element factor, $E(\theta, \phi)$, must be a function of ϕ and also have a peak much like the array factor. Optical phased arrays usually use grating based antennas in order to emit light out of the plane of the chip. For one-dimensional arrays, these antennas are oriented in the orthogonal spacial-dimension of the array in order to act as the second dimension of the total aperture of the array and confine light in the ϕ dimension. A longer grating allows for a larger aperture in the antenna dimension and allows for a small spot size in the ϕ dimension. Fig. 1-6(a) shows an example of an optical antenna based on a grating within a waveguide, and Fig. 1-6(b) shows the element factor of this antenna, $E(\theta, \phi)$.

The element factor of this antenna greatly confines the light in the ϕ dimension because it acts as a one-dimensional aperture. A longer antenna would further confine

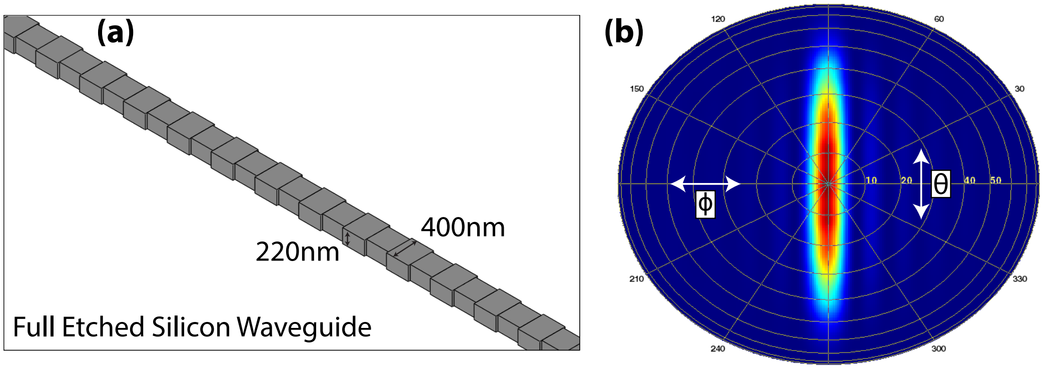

Figure 1-6: (a) Example optical phased array antenna based on a long silicon waveguide grating. (b) Element factor, $E(\theta, \phi)$, of the antenna.

the light in this dimension. The antenna is also θ dependent like the array factor since it is not a point source and has a finite width. This θ dependence allows for the suppression of the grating lobes caused by the array factor. In this example, the antenna emits straight upwards and has almost no power at $|\theta| > 50°$ so any grating lobes at $>\pm 50°$ will have minimal power. This suppression of the grating lobes is normally desirable and allows for more power in the main beam, even if the antenna pitch is $>0.5\lambda$. Another useful aspect of the element factor is that it can allow for steering in the ϕ direction. By tuning the response of the element factor to steer its peak throughout the ϕ dimension, two-dimensional steering can be accomplished with a one-dimensional phased array. For optical phased arrays, this is normally done through wavelength tuning since the antennas are grating based. For a grating with a single order, the wavelength dependence of the emission angle, ϕ, is given by $\sin(\phi) = n_{eff} - \frac{\lambda}{\Lambda}$, where n_{eff} is the effective index of refraction of the guided mode, and Λ is the pitch of the grating [33].

Another important parameter of phased arrays is the aperture size, which is the number of antennas multiplied by the pitch, Nd. The aperture size determines the angular spot size of the beam, many times denoted as just *spot size*. This characteristic is a measure of how collimated the beam is and how much the beam diffracts and increases in physical size during propagation. A more collimated beam can propagate farther and still have a small physical beam size. This is important for ranging and data communication applications. The spot size is normally reported as a full-width half-maximum (FWHM) power size and has the units of radians or degrees. The spot size in radians can be approximated from Eq. (1.4) at small α and large Nd as

$$SpotSize = \frac{2.78\lambda}{\pi N d} \tag{1.5}$$

Eq. (1.5) shows that the spot size is inversely proportional to the aperture size of the array. For a given aperture size, the spot size is proportional to the wavelength of the emitted light. This is expected because larger wavelengths diffract more [34]. Chap. 5 will discuss some of the implications of the spot size.

The splitting and phase shifting architecture of one-dimensional optical phased arrays can be subdivided into two main categories: a *tree architecture* with a tree-like splitting network with individual phase shifters, or a *cascaded phase shifter architecture*. A tree-like splitting network with individual phase shifters consists of a 1×N splitter network, where N is the number of antennas. This 1×N network can be created by having cascaded layers of 1×2 splitters, having a single 1×N splitter, or any other combination of splitters to have N outputs at the last layer of the tree. After the splitting network, each antenna has an individually controlled phase shifter placed before it. A schematic of this architecture is shown in Fig. 1-7(a). A cascaded phase shifter architecture consists of a bus waveguide with alternating directional coupler taps and phase shifters. Thus, the phase shifters are cascaded, changing the phase of one of the phase shifters will change the phase of all antennas after it. A schematic of this architecture is shown in Fig. 1-7(b) with all of the phase shifters at the same phase.

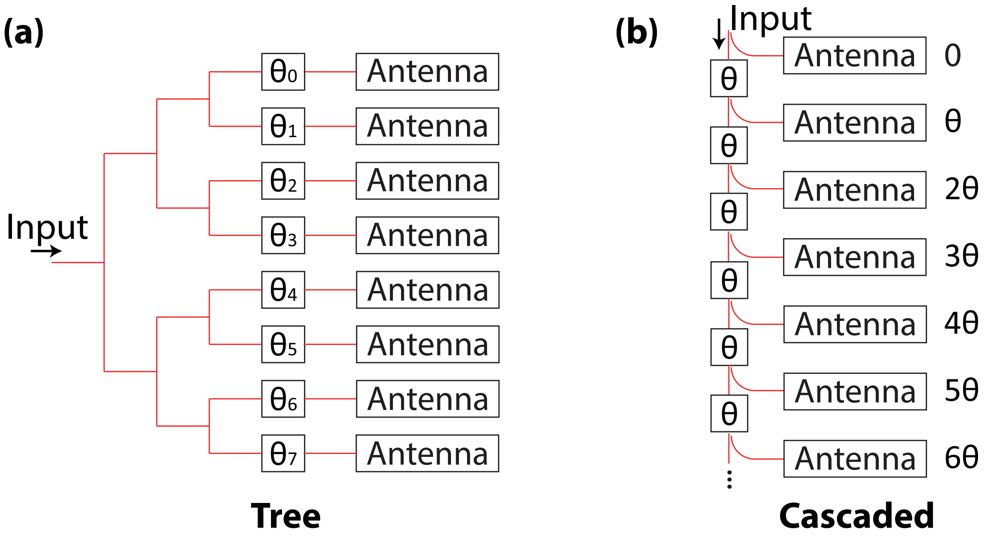

Figure 1-7: Schematic of a (a) tree and (b) cascaded phase shifter architecture for one-dimensional phased arrays.

There are advantages and disadvantages to using each architecture. The tree architecture is very simple and inherently scalable in the photonics. However, since each antenna needs individual phase control, there are many control signals to the system. For silicon-photonic-only chips, this can be difficult when the number of antennas is in the hundreds or greater since there is limited electrical contact pad space. The addition of CMOS electronics, either 3D heterogeneous [22] or monolithic integration [23], can alleviate this issue. For a cascaded architecture, it is not as scalable in the photonics since the cascaded phase shifter portion of the circuit often has a large footprint. However, for linear beam steering applications, a cascaded architecture allows for a single control signal that is tied to all of the phase shifters. This can greatly reduce system control complexity.

Phase modulation in optical phased arrays is primarily done using either the thermo-optic effect [19, 32] or the plasma-dispersion effect [20] in silicon waveguides. The index of refraction of silicon is heavily dependent on temperature with a thermo-optic coefficient of $1.8 \times 10^{-4}\,\mathrm{K}^{-1}$ [35]. Therefore, the thermo-optic effect allows for compact phase shifters ($<10\,\mu$m). The small size of these phase shifters make them very useful for the cascaded phase shifter architecture. However, thermal phase shifters can require a lot of power. In order to achieve a 2π phase shift with a silicon thermo-optical phase shifter, electrical power on the order of 10 mW is needed. Therefore, if an optical phased array has 100 antennas, roughly 1 W of power is needed to fully steer the beam. Thermal phase shifters also suffer from cross-talk if not properly isolated. Furthermore, they are limited to time constants on the order of a few microseconds, which limits steering speed. An example thermal phase shifter is shown in Fig. 1-8(a) (from [32]). Another way to realize a phase shifter is to create a PN junction in silicon and utilize the plasma-dispersion effect by injecting

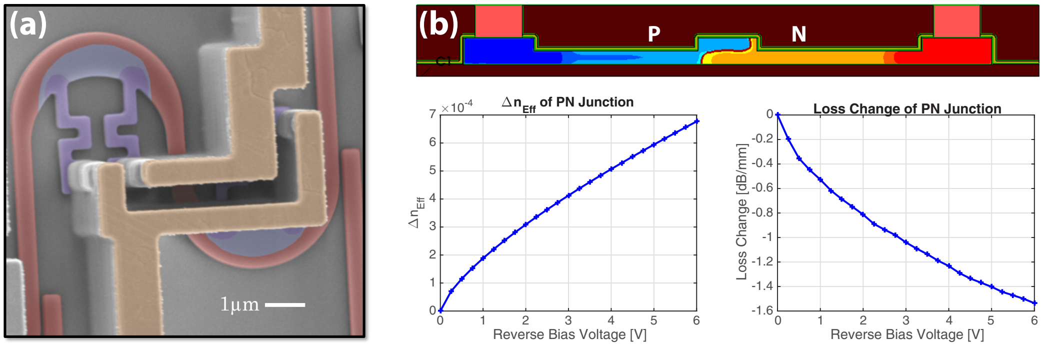

Figure 1-8: (a) Thermal phase shifter. From [32]. (b) Illustration of a silicon rib waveguide with vertical PN and measured data of the PN junction.

or removing carriers from the silicon waveguide. This changes the index of refraction of the waveguide slightly and changes the phase of the guided light [36]. However, by changing the number of carriers in the phase shifter, the optical loss also changes. This can broaden the spot size. Plasma-dispersion phase shifters do not suffer from cross-talk and can be driven at GHz speeds. However, they are fairly long, on the order of 100 μm to multiple millimeters depending on if they are carrier injection or carrier depletion phase shifters. Because of this, they can have high optical loss. A carrier depletion mode PN junction designed during this work is illustrated in Fig. 1-8(b). The measured change of effective index and loss as a function of voltage of this junction are also included.

1.3 Overview of Thesis

This thesis is structured as follows. Chap. 2 shows the first transmitting and receiving LIDAR module in silicon photonics. On-chip edge-couplers are used as a transmitter and receiver. The coherent detection method frequency-modulated continuous-wave LIDAR is utilized with an on-chip local oscillator and germanium photodetectors. Simultaneous distance and velocity measurements are taken. This system is further expanded on in Chap. 3 by utilizing phased arrays as a transmitter and receiver. The design and characterization of this phased array is described and the initial results of the LIDAR system is presented at the end of the chapter. Though this is the first coherent LIDAR demonstration based on optical phased arrays, this system is still constrained by input power limitations and relatively small aperture size. Looking towards the future, Chap. 4 covers the design and experimental results of the first optical phased array based on silicon nitride waveguides and antennas. Silicon nitride is utilized in order to increase the possible input power to the phased array, which is crucial for a long-range LIDAR system. A main beam output power of 520 mW is shown. Afterwards, Chap. 5 demonstrates record-breaking ultra-large-scale $4\times4\,\mathrm{mm}^2$ aperture optical phased arrays. These phased arrays are shown to be near diffraction limited showing the fidelity of the fabrication process and ability to scale the phased arrays even further. Finally, Chap. 6 shows one-dimensional optical phased arrays at visible wavelengths which has applications in bathymetric LIDAR and more.

Chapter 2

LIDAR on a Chip

This chapter demonstrates a chip-based device to perform ranging and velocity measurements and shows a combined transmitting and receiving LIDAR module in silicon photonics technology for the first time. It is based on frequency-modulated continuous-wave (FMCW) LIDAR [7]. FMCW LIDAR is a coherent detection method that offers an advantage over time-of-flight (TOF) detection techniques in an integrated setting. This is because Geiger-mode avalanche photodiodes [8, 37] and high-speed electronics are not required, and modest germanium photodetectors and simple electronics can be utilized. This allows for a simpler and more cost effective implementation.

2.1 Device and FMCW LIDAR Overview

The effective silicon photonic LIDAR device that this chapter covers is shown in Fig. 2-1(a). The full device was originally designed for heterodyne interferometry and is described in [38]. LIDAR measurements can be taken by only measuring the measurement arm. It was fabricated using 193 nm immersion lithography on a 220 nm-thick silicon-on-insulator (SOI) wafer with 2 μm buried oxide (BOX). It consists of an input edge-coupler based on a silicon inverse-taper. On chip, the input optical power is split using an adiabatic splitter to act as a local oscillator (LO) and transmitted signal (TX). The TX signal is coupled off-chip with an edge-coupler and then is

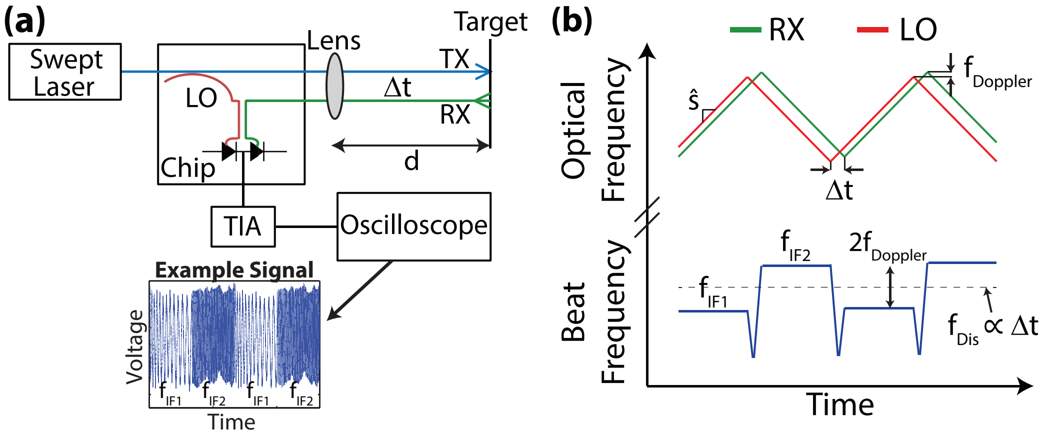

Figure 2-1: (a) Illustration of the effective device consisting of silicon photonic chip with collimating lens. Full device described in [38]. (b) Concept of frequency-modulated continuous-wave LIDAR with triangular modulation.

collimated with a lens and incident to a target. Light reflected off the target (RX) is received through another edge-coupler and is beaten against the LO and input to on-chip balanced germanium photodetectors. The photodetectors are similar to those described in [22]. An external transimpedance amplifier (TIA) is used to convert the photocurrent to a voltage that is analyzed by an oscilloscope.

When the input laser to the device is swept in frequency, FMCW LIDAR can be performed. The concept of FMCW LIDAR with triangular modulation is illustrated in Fig. 2-1(b). Because there is a time delay, Δt, between the on-chip LO signal and the RX signal due to the propagation time to the target, the two signals have a different optical frequency when beaten together because of the frequency swept input laser. When the LO and RX signal are beaten together, for a stationary target, a single electrical beat frequency, f_{Dis}, occurs that is proportional to the distance to the target. This frequency is given by $f_{Dis} = \Delta t \hat{s} = \frac{2d}{c}\hat{s}$, where Δt is the time delay of the LO and RX signal, $\hat{s}$ is the sweep rate of the laser, d is the distance to the target, and c is the speed of light. For a moving target, two distinct beat frequencies, f_{IF1} and f_{IF2}, occur in different time regions depending whether the laser is sweeping upwards or downwards. The difference of these two beat frequencies is the twice Doppler shift that occurs when the transmitted light hits the moving target, $f_{IF1} - f_{IF2} = 2f_{Doppler}$. The average of the two beat frequencies is proportional to the time-of-flight distance to the target, $\frac{f_{IF1}+f_{IF2}}{2} = f_{Dis}$.

2.2 Balanced Photodetector

The most important component of the device shown in Fig. 2-1(a) is the on-chip balanced detector that beats the LO and the RX signals and produces an electrical signal whose frequency contains information about the distance and velocity of the target. A layout rendering of the balanced photodetector is shown in Fig. 2-2. It consists of two inputs, the LO and the RX, that are coupled together using an adiabatic coupler based on mode-evolution [39]. The two outputs of the adiabatic coupler are input to separate on-chip germanium photodetectors. These photodetectors are connected in series, and thus their currents subtract at the electrical node that connects them. This current at this point of the circuit is the *signal* current that is input to an amplifier.

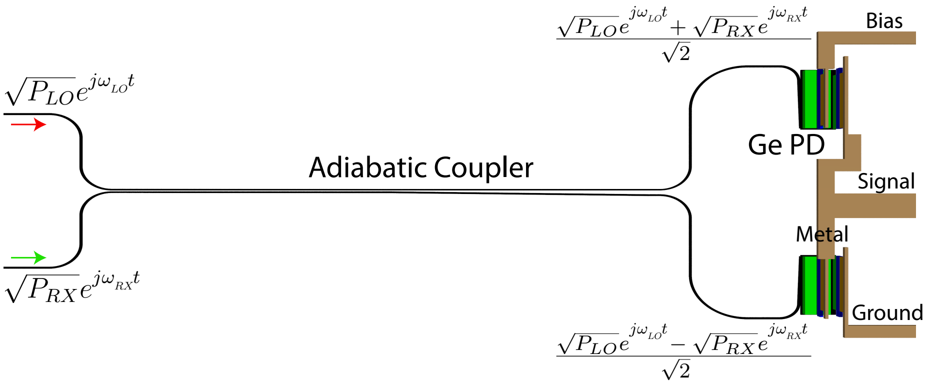
$\frac{\sqrt{P_{LO}}e^{j\omega_{LO}t} + \sqrt{P_{RX}}e^{j\omega_{RX}t}}{\sqrt{2}}$
Bias
$\sqrt{P_{LO}}e^{j\omega_{LO}t}$
Ge PD
Adiabatic Coupler
Signal
Metal
$\sqrt{P_{RX}}e^{j\omega_{RX}t}$
Ground
$\frac{\sqrt{P_{LO}}e^{j\omega_{LO}t} - \sqrt{P_{RX}}e^{j\omega_{RX}t}}{\sqrt{2}}$

Figure 2-2: Layout rendering of the balanced photodetector consisting of an adiabatic coupler and two germanium photodetectors.

To show that this detector does produce the desired beat frequency between the LO and the RX signals, we can describe the input to the balanced photodetector by the vector

$$Input = \begin{bmatrix} \sqrt{P_{LO}} e^{j\omega_{LO}t} \\ \sqrt{P_{RX}} e^{j\omega_{RX}t} \end{bmatrix} \tag{2.1}$$

where P_{LO} and P_{RX} are the optical powers, and ω_{LO} and ω_{RX} are the optical frequencies of the LO and the RX signal, respectively. Utilizing the transfer matrix of the adiabatic coupler, the output of the adiabatic coupler and thus the input to the two photodetectors can be found

$$AfterCoupler = (\frac{1}{\sqrt{2}} \begin{bmatrix} 1 & 1 \\ 1 & -1 \end{bmatrix}) \begin{bmatrix} \sqrt{P_{LO}} e^{j\omega_{LO}t} \\ \sqrt{P_{RX}} e^{j\omega_{RX}t} \end{bmatrix} = \frac{1}{\sqrt{2}} \begin{bmatrix} \sqrt{P_{LO}} e^{j\omega_{LO}t} + \sqrt{P_{RX}} e^{j\omega_{RX}t} \\ \sqrt{P_{LO}} e^{j\omega_{LO}t} - \sqrt{P_{RX}} e^{j\omega_{RX}t} \end{bmatrix} \tag{2.2}$$

The current that each photodetector produces can be found by multiplying each output by its complex conjugate along with the responsivity of the photodetector, R. In our mathematical formation, this is done with a vector element-wise product.

$$\begin{aligned} Currents = \frac{R}{2} \begin{bmatrix} \sqrt{P_{LO}} e^{j\omega_{LO}t} + \sqrt{P_{RX}} e^{j\omega_{RX}t} \\ \sqrt{P_{LO}} e^{j\omega_{LO}t} - \sqrt{P_{RX}} e^{j\omega_{RX}t} \end{bmatrix} \odot \begin{bmatrix} \sqrt{P_{LO}} e^{-j\omega_{LO}t} + \sqrt{P_{RX}} e^{-j\omega_{RX}t} \\ \sqrt{P_{LO}} e^{-j\omega_{LO}t} - \sqrt{P_{RX}} e^{-j\omega_{RX}t} \end{bmatrix} = \\ \frac{R}{2} \begin{bmatrix} P_{LO} + P_{RF} + 2\sqrt{P_{LO}P_{RF}} \cos((\omega_{LO} - \omega_{RX})t) \\ P_{LO} + P_{RF} - 2\sqrt{P_{LO}P_{RF}} \cos((\omega_{LO} - \omega_{RX})t) \end{bmatrix} \end{aligned} \tag{2.3}$$

Finally, since the photodetectors are in series, the two currents subtract to get our final current signal

$$Signal = 2R\sqrt{P_{LO}P_{RF}} \cos((\omega_{LO} - \omega_{RX})t) \tag{2.4}$$

We see that the output current signal of the balanced photodetector is a sinusoid with a frequency that is the difference of the optical frequencies of the LO and the RX signal as desired, i.e. it is the beat frequency between the two. There is also no DC component to the signal. This is desirable because a DC component could saturate the TIA after the photodetectors. Additionally, since the signal arises through coherent mixing of the LO and the RX optical signals, it is proportional to the square root of the product of the LO and the RX optical powers. Therefore, the signal is amplified by the LO.

The performance of the balanced detector is dependent on the performance of the adiabatic splitter and the germanium photodetectors. The adiabatic splitter should split exactly 50/50 or there will be some undesired DC photocurrent and a portion of the AC signal will be subtracted out. An individual adiabatic splitter was measured, and the results are shown in Fig. 2-3(a). Over a wide bandwidth, the splitting ratio of the splitter is near 50/50, showing good performance. For the photodetectors, the output current signal is proportional to the responsivity, so a high responsivity is crucial. Fig. 2-3(b) shows the measured responsivity of a single photodetector. A high responsivity of 1 A/W is measured at a wavelength of 1550 nm. At longer wavelengths, the responsivity drops off because germanium has a lower absorption at these wavelengths.

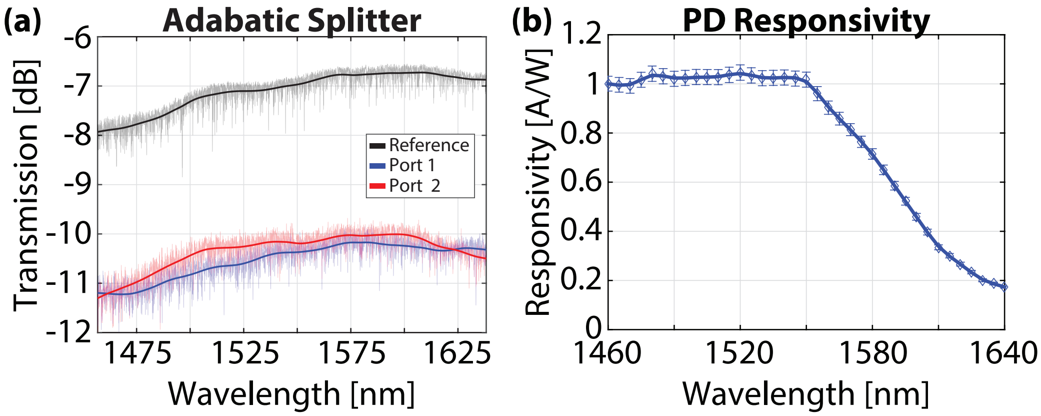

Figure 2-3: (a) Measured response of a single adiabatic coupler. (b) Measured photodetector responsivity.

2.3 Laser Diode Characterization

The other important component of the LIDAR system shown in Fig. 2-1(a) is the laser diode itself. Although it is off-chip, the laser diode determines the resolution of the device. A linear optical frequency sweep is needed in the FMCW scheme shown in Fig. 2-1(b) in order to achieve constant beat frequencies. If the sweep is not linear, then the beat frequencies continuously increase or decrease in time [40]. If our detection scheme is a simple discrete Fourier transform (DFT) module, then the frequency resolution is greatly decreased because of spectral leakage into neighboring frequency bins. This fundamentally limits the ranging resolution of the LIDAR device. There are some signal processing algorithms that allow a non-linear laser sweep [41–43] but are outside the scope of this thesis.

A 40 mW JDSU laser diode at 1543 nm is used here as the laser source. The laser diode can be swept by modulating the injection current in a triangular fashion. The injection current modulates the optical frequency due to a combination of the plasma-dispersion effect and the stronger (but slower) thermo-optic effect. However, modulating the injection current linearly does not necessarily produce a linear frequency sweep. In order to engineer a current sweep to produce a linear frequency sweep, the frequency of the laser diode was measured at various injection currents using an optical spectrum analyzer and is shown in Fig. 2-4(a). As Fig. 2-4(a) indicates,

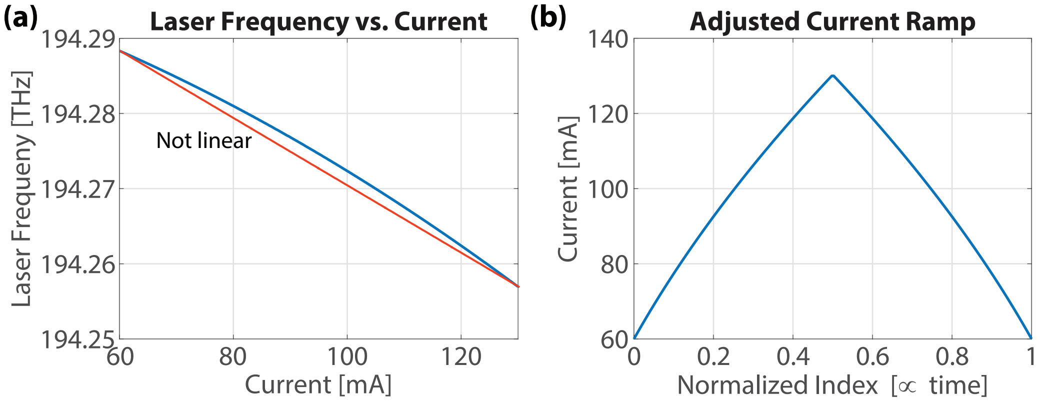

Figure 2-4: (a) Measured laser diode frequency as a function of injection current. (b) Back-calculated current ramp to produce a linear frequency sweep.

the laser diode does not have a linear frequency response with current. However, this curve can be back-calculated to produce an adjusted current ramp that results in a linear frequency sweep (Fig. 2-4(b)). It is also important to note that the different frequency responses of the thermo-optic and the plasma-dispersion effect makes the adjusted current ramp invalid at high sweep frequencies since it was calculated using the DC response [44].

Even with this adjusted current ramp, the frequency sweep of the laser will not be exactly linear. This is due to the discontinuities at the edge of the sweeps and the relaxation time of the laser, which causes a transient response. In order to reduce spectral leakage while doing DFT analysis, time-gating is utilized in our DFT module as shown in Fig. 2-5. Only a portion of each time domain frequency region undergoes the DFT calculation, the portion that contains the transients is not included. The DFT calculated region is made as long as possible without the effect of spectral leakage due to the non-linearities because having a long observation time allows for a smaller DFT resolution.

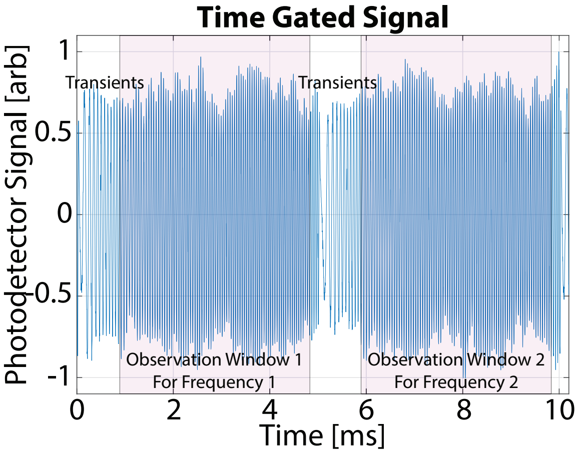

Figure 2-5: Example of time gating the photodetector signal to reduce the effects of the transients.

2.4 Experimental Results

The following experimental results were taken on the setup shown in Fig. 2-6. It consisted of a 1.5 m long Aerotech motorized stage with speed control up to 300 mm/s. The target used was a cube reflector. The silicon photonic LIDAR device is on a $6 \times 25\,\mathrm{mm}^2$ chip. Light was input to the chip using a cleaved SMF-28 fiber and the output TX light was collimated with a 20× objective.

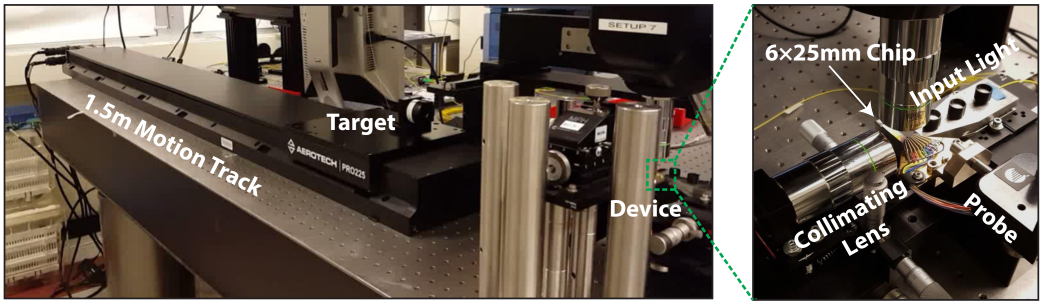

Figure 2-6: Experimental setup utilizing a 1.5 m motion track.

2.4.1 Homodyne Doppler Measurements

First, in order to test the receiving capabilities of the device and the electronics, homodyne Doppler measurements were taken. The concept of this measurement is shown in Fig. 2-7(a). This measurement does not consist of sweeping the input laser and directly determines the Doppler shift of a moving target. The TX/RX signal undergoes a Doppler shift when hitting a moving target. When the RX is

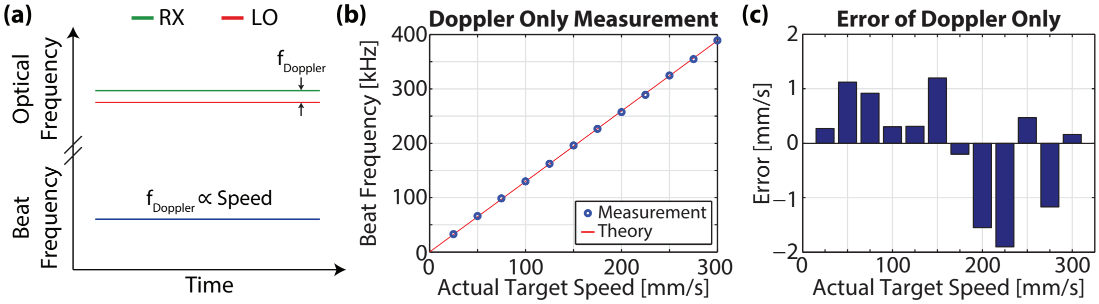

Figure 2-7: (a) Concept of homodyne Doppler measurements. (b) Experimental results of the homodyne Doppler measurements with a theoretical line of the speed dependent Doppler shift. (c) Speed error of the data set in (b).

beaten against the LO, the Doppler beat frequency is produced. When the target is not moving, there is no beat frequency between the RX and the LO. The speed of the target was varied utilizing the motorized stage, and the beat frequency was measured when the target was 1 m away from the device (Fig. 2-7(b)). The beat frequency matched the theoretical Doppler shift for each speed. The speed error for each measurement is shown in Fig. 2-7(c). The maximum absolute error was 2 mm/s. The average and maximum relative error were 0.7% and 2.2%, respectively, thus showing the accuracy of the receiving module of the device.

2.4.2 Stationary Target Measurements

FMCW measurements were then taken by modulating the injection current of the laser diode. As mentioned previously, the injection current was modulated with an arbitrary function generator, and the driving function was designed for a linear optical frequency sweep in a triangular fashion. Measurements were first taken on a stationary target at varying known distances at 10 mm intervals and, for this experiment, the laser injection current triangular frequency was 100 Hz, and the resulting optical frequency sweep rate was 6.4 THz/s. Fig. 2-8(a) shows the measured beat frequency at each distance. The target distance ranged from 0.5 m to 2.0 m. As expected, the beat frequency is proportional to the distance to the target. Fig. 2-8(b) shows the Fourier transform of the raw data for different distances spaced at 10 mm intervals. Each peak is resolved in the frequency domain. Finally, a histogram of the error in

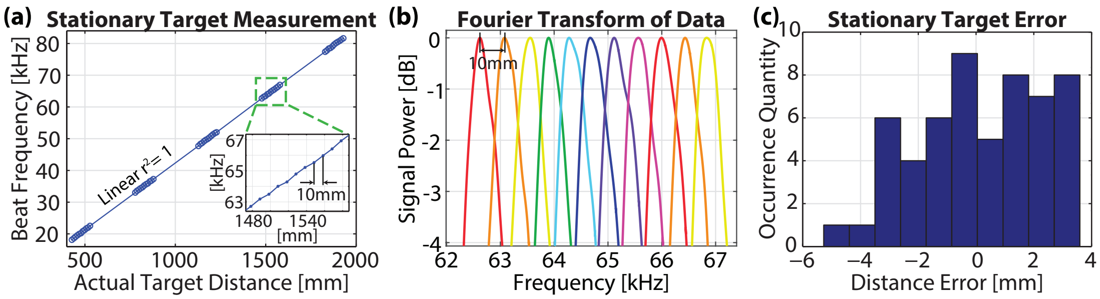

Figure 2-8: (a) Measured beat frequency at various stationary target distances at 10 mm intervals. (b) Fourier transform of time domain data in (a) showing resolved frequency peaks. (c) Distance error of the measurements shown in (a).

the distance measurements is shown in Fig. 2-8(c). Absolute errors were less than 10 mm for distances up to 2 m, showing a noise-limited resolution of 20 mm. The maximum relative error was 0.75%. Measurements taken on separate days were seen to have had similar error figures.

2.4.3 Moving Target Measurements

FMCW measurements were then taken on a moving target at various speeds and distances. The four velocities measured were 75, 150, 225, and 300 mm/s at distances ranging from 0.5 m to 2.0 m. In this experiment, the laser current triangular frequency was increased to 5 kHz in order to increase the laser sweep rate to 190 THz/s. This was to ensure that the Doppler shift frequency would be less than the beat frequency seen for a stationary target. The two measured beat frequencies in the different time domain regions for each measurement are shown in Fig. 2-9(a) along with the average beat frequency. The calculated velocity of the target for each measurement

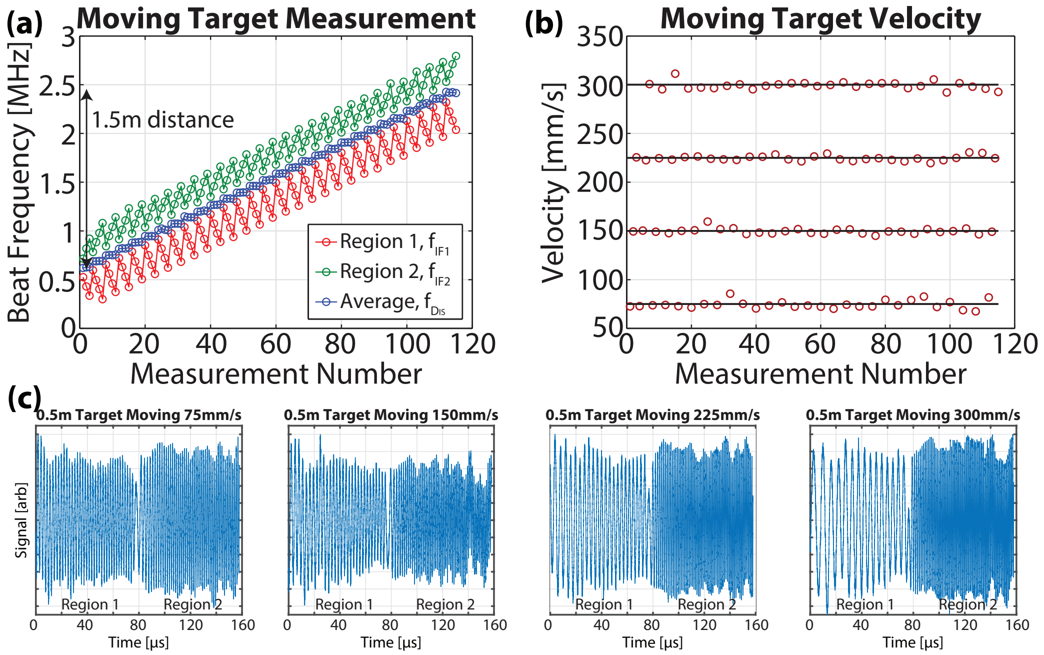

Figure 2-9: (a) Measured beat frequencies for a moving target while sweeping velocity and distance. (b) Calculated velocity of the data set in (a), black lines show actual velocity. (c) Raw time domain data of the 0.5 m target measurements at four different velocities.

is shown in Fig. 2-9(b). The raw data for the experiments when the target was at 0.5 m is plotted in Fig. 2-9(c). The two frequency regions are clearly seen. As the target velocity increases, the difference of the two frequencies increase as expected, but their average remains the same since the target is at a constant distance.

A histogram of the distance error of these measurements is shown in Fig. 2-10(a), and a histogram of the error of velocity is shown in Fig. 2-10(b). The distance measurement had a maximum absolute error of 20 mm and a maximum relative error of 3.2%. The average relative error of the velocity measurement was 1.9%. The overall increase of error in this experiment is caused by the faster laser sweep being slightly non-linear. Further optimizations on the linearity of the sweep could be performed using optoelectronic feedback [45–47].

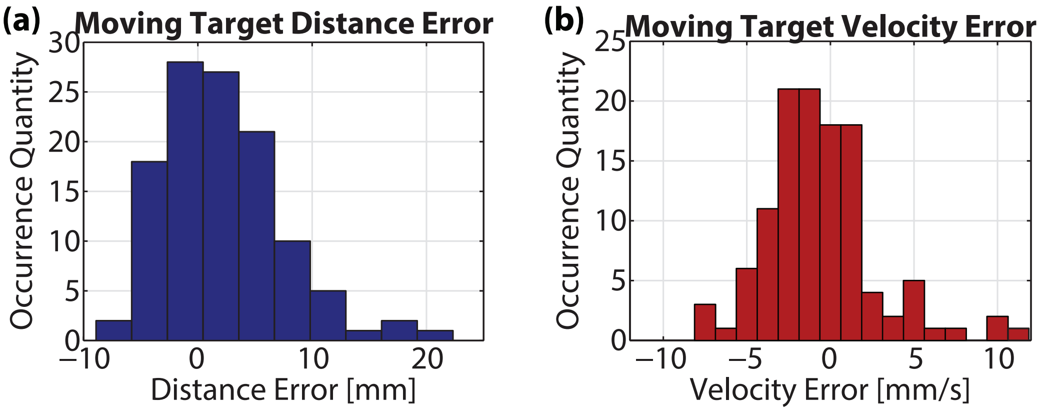

Figure 2-10: Error of calculated target (a) distance and (b) velocity of the data set in Fig. 2-9(a).

2.5 Conclusion

In conclusion, a silicon photonic FMCW LIDAR system with transmitting and receiving waveguides and photodetectors has been demonstrated. Homodyne Doppler measurements and LIDAR with simultaneous distance and velocity measurements were performed with a 2 m range, 20 mm resolution, and respectable error figures. This work demonstrates a chip-based device to perform ranging and velocity measurements and shows a combined transmitting and receiving LIDAR module in silicon photonic technology for the first time. Furthermore, the device was fabricated in a state-of-the-art CMOS foundry on a 300 mm wafer and can be mass-produced at a low chip cost.

Chapter 3

Grouped Cascaded Phased Array for Integrated LIDAR

In Chap. 2, a silicon photonic frequency-modulated continuous-wave (FMCW) LIDAR module was shown. However, this device could not perform beam steering since edge-couplers were used for transmitting and receiving. The purpose of this chapter is to develop a phased array that can replace the edge-couplers in order to realize a silicon photonic LIDAR module that has steering capability. This phased array needs to have simple control so it can be easily integrated into the system developed in Chap. 2 but still have an adequate aperture size in order to effectively collimate and receive a beam.

3.1 Phased Array Design

3.1.1 Grouped Cascaded Phase Shifters

A phased array with a cascaded phased shifter architecture was designed in order to be placed in a FMCW LIDAR system. The primary reason for this choice of architecture was that an antenna count of at least 50 elements was needed. This number of antennas was necessitated by the required aperture size for a small spot size and the demand for a large receiving area. Due to the large antenna count, using a tree architecture would require over 100 electrical input signals to drive such a system. 3D integrated CMOS electronics [22] were not available on this fabrication run, and incorporating this number of signals in a single photonic-only system was considered too risky for a first iteration of an integrated LIDAR system with phased arrays. Unlike previous phased arrays with a cascaded architecture [32], it was decided to have the phase shifters grouped into three separate electrical signals, instead of only one, in order to correct for any phase noise in the device due to fabrication errors. This architecture is shown in Fig. 3-1(a) and is called a *grouped cascaded phase shifter architecture*. Each continuous third of the phase shifters are connected to a distinct electrical signal and allows the control of the linear phase ramp within only those phase shifters. If the three portions have different built-in passive linear phase ramps due to fabrication errors, then the grouped phase shifters can correct it. This allows for a more robust device than if there were only a single control signal, which would not allow for any phase noise correction. More groups allow for greater correction at the cost of additional input signals to the phased array. Three groups were chosen because the full LIDAR system could still be controlled with an available 9-pin DC probe.

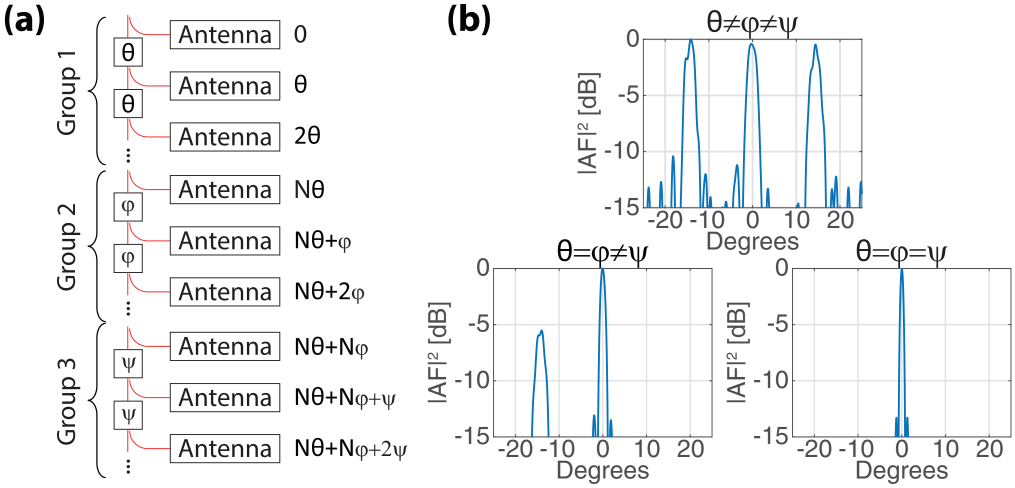

Figure 3-1: (a) Schematic of a grouped cascaded phase shifter architecture with three groups. (b) Concept of sub-phased arrays formed by a grouped architecture showing the ability to create multiple beams.

Another interpretation of this architecture is that we are separating the phased array into three sub-phased arrays that are independently controlled. This concept is shown in Fig. 3-1(b) utilizing an example with a 50-element, 1.3λ pitch, grouped cascaded phased array. When the three phase shifter groups are set to different values, three distinct first-order beams are seen within the far field. This is each sub-phased array emitting a separate beam from the others since its linear phase ramp is distinct. When two of the phase shifter groups are set to the same value, two beams are seen within the far field with one having a smaller spot size than the other. This is because the two sub-phased arrays that have the same phase values are now acting as a single phased array with a larger aperture. Finally, all three phase groups can be set to the same value so a single, small spot size beam is emitted.

3.1.2 Phase Shifter and Splitter Design

Thermal phase shifters based on adiabatic bends were used as phase shifters in this phased array [32,48]. The adiabatic bend consists of a single-mode 400 nm-wide silicon waveguide that is increased in width as it is bent 180°. It is increased to a width of 1 μm with an outer radius of 6 μm. Silicon tethers are placed on the inner wall of the bend which are electrically contacted with tungsten plugs to a copper routing layer. Because of the design of the adiabatic bend, the guided light does not interact with these tethers, thereby allowing for a low-loss electrically contacted bend. This bend, including the contact tethers, was simulated with finite-difference time-domain (FDTD) simulations to have an efficiency of 99.5%. To create an electrical resistor with the majority of the resistance within the waveguide, the tethers are heavily N-doped and the waveguide is lightly N-doped. This allows for an efficient thermal phase shifter since most of the Joule heating occurs in the waveguide with a high overlap with the optical mode.

In order to tap off light in-between each thermal phase shifter, directional couplers were used. This was done by placing a 400 nm-wide silicon waveguide adjacent to the thermal phase shifter right before the adiabatic bend. An example layout of this, including the N-doping and the routing metal, is shown in Fig. 3-2(a). The coupling

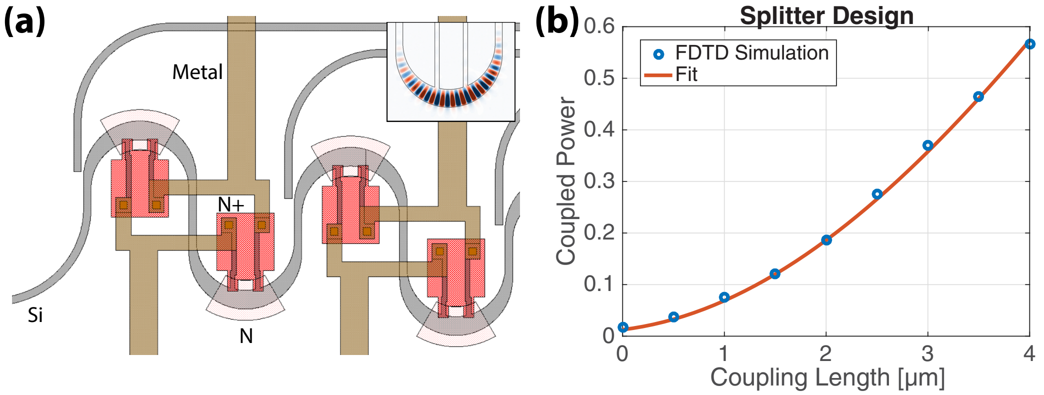

Figure 3-2: (a) Layout of cascaded phase shifters with alternating directional couplers. Inset shows FDTD simulation of the adiabatic bend. (b) FDTD simulation of power coupling as a function of coupling length.

percentage of this coupler was simulated in FDTD, and the results are shown in Fig. 3-2(b) with a fitted theoretical $sin()^2$ curve. The coupling strengths of the directional couplers were synthesized to produce uniform power to each antenna by increasing the coupling strength between subsequent couplers. In previous work, this has been performed utilizing a hyperbolically increasing coupling strength [32, 48], $c_n[n]$, given by

$$c_n[n] = \frac{1}{N + \frac{1}{c_N} - n} \tag{3.1}$$

where N is the total number of antennas, n is the index (1-based) of the current antenna, and c_N is the fixed coupling of the last antenna which can take any value. When $c_N = 1$, the last directional coupler will couple all the light from the bus. Not doing this can be useful, since otherwise, the last few directional couplers can have a large coupling length in order to achieve high coupling values. This can greatly change the phase response of these directional couplers. If the phase response of the directional coupler is not accounted for with passive delay structures (as it is not done in this work), then having a different phase response in the last few directional couplers breaks the passive linear phase ramp between the antennas and can be detrimental to the phased array performance. However, if $c_N \neq 1$, there is some power loss given by $(1/c_N - 1)/(N + 1/c_N - 1)$. Therefore, in this work, we set $c_N = 1/4$ to have a power loss of <10% but still have similar directional couplers throughout the structure.

Eq. (3.1) assumes that the phase shifters in-between the antennas are lossless. However, in this work, more rigor was desired, and the loss of the phase shifter was included in the coupler synthesis. If a phase shifter efficiency, η, is included in-between each directional coupler, then the strength of the coupling to produce uniform power to each antenna is given by the formula

$$c[n] = \frac{1-\eta}{\eta^{n-N}(\eta + \frac{1-\eta}{c_N}) - \eta} \tag{3.2}$$

The full derivation of this formula is outside the scope of this section but can be derived by solving the recurrence relation $c[n] = \eta(1 - c[n])c[n+1]$ with the initial condition $c[N] = c_N$. As expected, it can be seen by using L'Hôpital's rule that the limit of Eq. (3.2) when $\eta \rightarrow 1$ is identical to Eq. (3.1). Eq. (3.2) with an estimated $\eta = 0.99$, along with the fitted FDTD coupler values shown in Fig 3-2(b), were used for the directional coupler design and synthesis for 50 couplers and antennas.

3.1.3 Antenna Design

The antenna used in this phased array was based on a grating in a silicon waveguide. The grating is created by periodically perturbing inwards with a full etch in a 400 nm-wide, 220 nm-thick silicon waveguide. Utilizing a full etch instead of ridge etch mitigates the risk of over or under etching the waveguide. Polycrystalline silicon

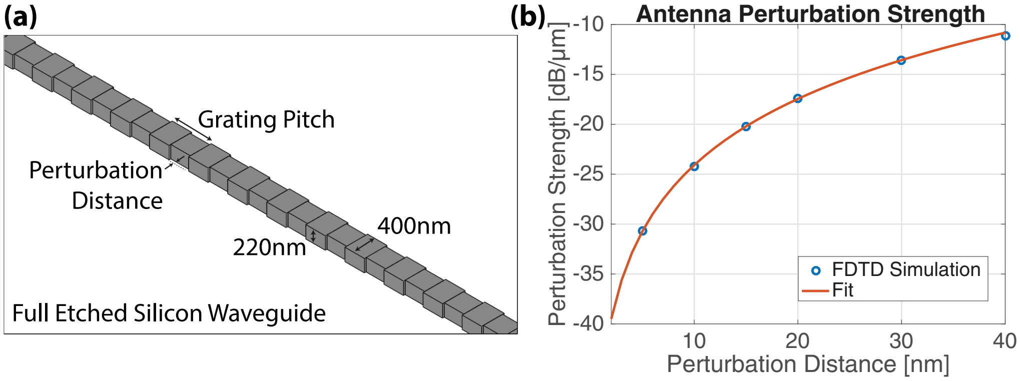

Figure 3-3: (a) Rendering of a portion of a full etch based antenna. (b) Perturbation strength as a function of perturbation distance.

overlays can reduce this risk [49] but are not available in this fabrication process. A rendering of a portion of this antenna is shown in Fig. 3-3(a).

These perturbations cause a portion of the guided light within the waveguide to be scattered. The strength of the perturbation was simulated as a function of the inwards perturbation distance using an FDTD simulation. In this simulation, light passed through a waveguide with 12 perturbations and the total power left in the waveguide mode was measured. A graph of the perturbation strength as a function of perturbation distance is shown in Fig. 3-3(b). The unit of the perturbation strength is in %/μm which is conveniently plotted in dB/μm. For example, 0.1%/μm=-30 dB/μm, which means that 0.1% of the light is emitted after 1 μm. For 500 μm-long antennas, which was our goal antenna length for this device, Fig. 3-3(b) shows that the relevant perturbation distances range from 7 nm to around 20 nm. Although this is a small range, our fabrication process has a 1 nm mask resolution that allows for perturbations of this size to be fabricated and different perturbation distances to be resolved.

If a uniform perturbation is used in the antenna, then there is a fixed delay rate along the antenna, and exponential emission occurs in the near field. Though simple to design, this makes the effective length of the antenna shorter than the physical length because certain portions of the antenna emit more than others. This increases the spot size from a rectangular aperture diffraction limited spot in the antenna dimension. Furthermore, a phased array with an exponential emission pattern is less efficient at receiving than one with a uniform emission pattern. Any incoming light to the phased array will effectively be a plane wave with a uniform intensity pattern. The mismatch between this plane wave and the emitted mode denotes a less efficient receiver antenna. Another interpretation of why a uniform perturbation is less efficient at receiving is to note that forward-backward symmetry along the antenna is not broken. As a result, any received light will be split equally towards and away from the output of the receiving phased array. Therefore, uniformly emitting antennas were designed instead of exponentially emitting antennas. This is done by hyperbolically increasing the antenna strength.

This can be derived by solving the following differential equation relating the guided and scattered power and the perturbation strength

$$\frac{dW(x)}{dx} = -W(x)P(x) = -S(x) \tag{3.3}$$

where $W(x)$ is the power of the guided light in the antenna at location x, $P(x)$ is the perturbation strength at location x, and $S(x)$ is the power of the light scattered at location x. If $S(x)$ is set to be uniform, $S(x) \equiv c$, then $P(x)$ is solved to be $P(x) = \frac{c}{c_1 - x}$, where c_1 is some constant. The mathematical formulation in Eq. (3.3) can be used to solve for an arbitrary emission pattern.

Fig. 3-4(a) shows the perturbation distance required at a length away from the end of the antenna to realize uniform emission, i.e. a hyperbolically increasing perturbation strength. However, when the perturbation distance is changed throughout different grating periods, the optical lengths also change because the effective index changes. If this problem is not corrected, different grating periods will emit at different angles. Therefore, the physical grating pitch must increase as the perturbation distance increases. Fig. 3-4(b) shows the needed grating pitch for a given perturbation distance in order to maintain a grating optical length of 1.55 μm. This will make the antenna emit straight upwards with an input light of 1550 nm.

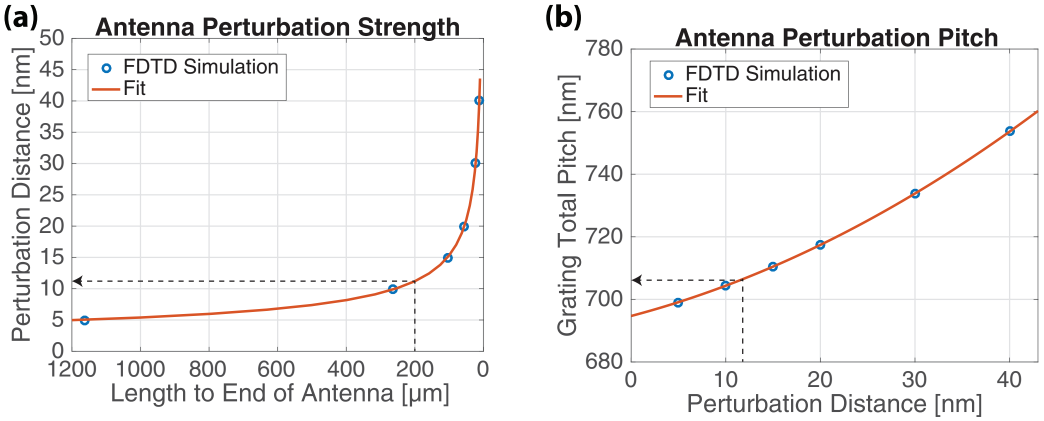

Figure 3-4: (a) Perturbation distance needed throughout the antenna to produce uniform emission. (b) Grating pitch needed as a function of perturbation distance for straight up emission at $\lambda = 1550$ nm.

3.2 Experimental Results

3.2.1 Phased Array Characterization

Fig. 3-5(a) shows a 3D rendering of the optical phased array. The phased array consists of 50 grating-based antennas placed at a 2 μm pitch. The array factor of this device predicts a main beam full-width half-maximum (FWHM) intensity spot size of 0.80° in the lateral direction and grating lobes at ±51° when the main beam is centered at 0°. The antenna length is 500μm and, as mentioned before, the antennas are designed to have a uniform emission pattern. The element factor of this antenna predicts a 0.16° FWHM intensity confinement along the antenna direction. The optical phased array was fabricated using 193 nm immersion lithography on a 300 mm silicon-on-insulator wafer with 220 nm silicon height and 2 μm buried oxide. Scanning electron microscope (SEM) images of the device are shown in Fig. 3-5(b-d) after etching the top silica cladding.

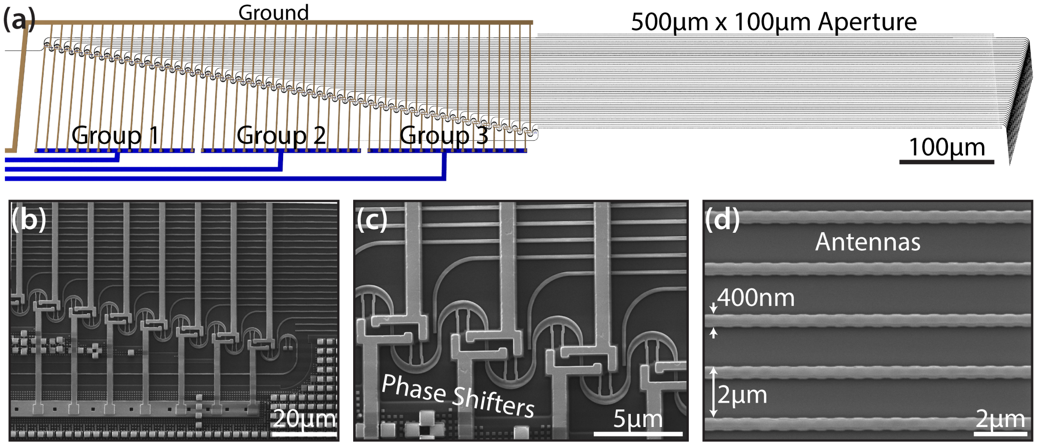

Figure 3-5: (a) 3D rendering of the optical phased array. SEM images of the (b) cascaded phase shifter architecture, (c) close-up of the thermal phase shifters, and (d) the full etch silicon grating based antennas with waveguide width of 400 nm and pitch of 2 μm.

1550 nm light was input into the phased array, and the near field emission pattern was measured (Fig. 3-6(a)). Uniform emission is seen in the antenna dimension, showing that the hyperbolically increasing antenna strength worked as designed. In the array dimension, there is a slight increase of power to each antenna, showing that the directional couplers were weaker than designed. Fig. 3-6(b-d) shows the far field emission patterns of the phased array when mimicking the simulations in Fig. 3-1(b).

Fig. 3-6(b) shows the measured far field intensity of the phased array when the three grouped cascaded phase shifters are set to different voltages. Three distinct beams in the far field are measured corresponding to each group respectively. Fig. 3-6(c) shows the far field when group 2 and group 3 are pointed in the same direction. The spot size of this merged beam is smaller as the effective aperture of the phased sub-array is increased. Fig. 3-6(d) shows the far field when all three groups are pointed in the same direction showing a single, uncorrupted beam within the NA of the lens (NA=0.4, angle radius=23.6°). The beam has the smallest spot size when the three groups are controlled by slightly different voltages, 5.6 V, 5.5 V and 5.1 V in this case, proving the benefit of adding voltage control groups within the cascaded phase shifter architecture. In order to accurately measure the spot size, a lower NA lens (NA=0.25) was used and the intensity profile is shown in Fig. 3-6(e). The FWHM intensity of the beam is measured to be 0.85°×0.18° and is in good agreement with the theoretical value of 0.80°×0.16°. Small side lobes are observed on the side of the beam at angle offsets that agree with the theoretical array factor. The side lobes have

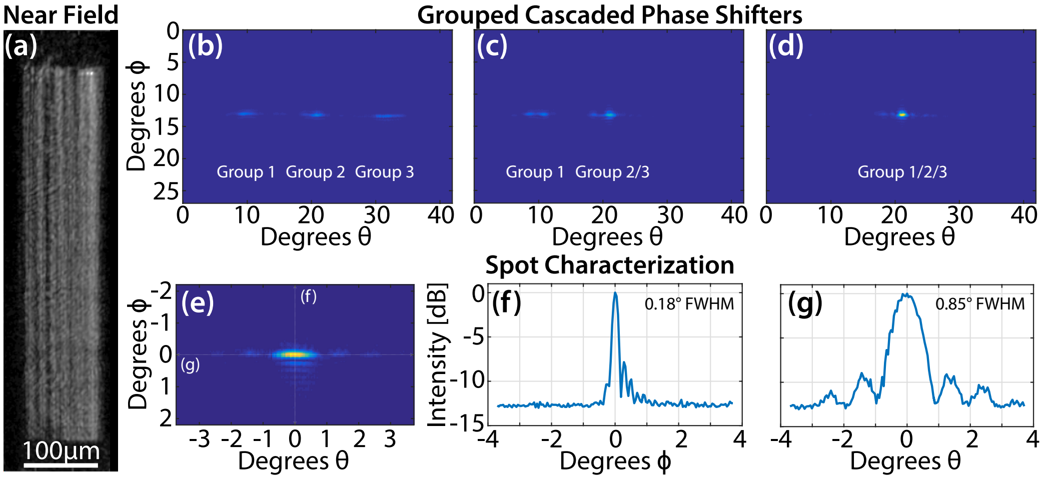

Figure 3-6: (a) Near field of the array. (b) Far field of the array when the three phase shifter groups act as three phased sub-arrays, (c) as two phased sub-arrays, (d) as a single phased array. (e) Close up of the far field spot. (f-g) Intensity cuts of the far field spot indicated in (e).

8 dB suppression. Intensity cuts of the beam in Fig. 3-6(e) are shown in Fig. 3-6(f,g).

Fig. 3-7(a) shows the far field of the device when steered using both thermal and wavelength tuning. Thermal tuning only steers in the lateral direction, θ, while wavelength tuning primary steers in the antenna direction, ϕ, but also slightly in the lateral direction because of the inherent optical path length mismatch in the cascaded phase shifters. With thermal steering using 0–1.2 W electrical tuning power, and wavelength tuning from 1454 nm to 1641 nm, a steering range of 46°×36° is achieved.

Fig. 3-7(b) shows the output of the phased array when an IR card is placed adjacent to it. A strong main and grating lobe are clearly visible. Another grating lobe on the other side of the main lobe is blocked by the electrical tuning probe, and therefore is not captured by the card. The grating lobes have similar powers to the main beam because of an imperfection in the design of the antennas, which can be mitigated simply by increasing the antenna width [50] from 400 nm to 610 nm. Despite strong grating lobes, the power in the main beam was measured to be 1 mW, limited primary by the non-linearities of the silicon waveguides.

With current device specifications, a lens-free free-space data link can be easily created. We modulated the input laser signal with a PRBS at 1 Mbps using an external LiNbO$_3$ modulator and transmitted the data through the phased array to free-space. The output from the phased array evolved into a beam size of $\sim$1.5×0.3 cm^2

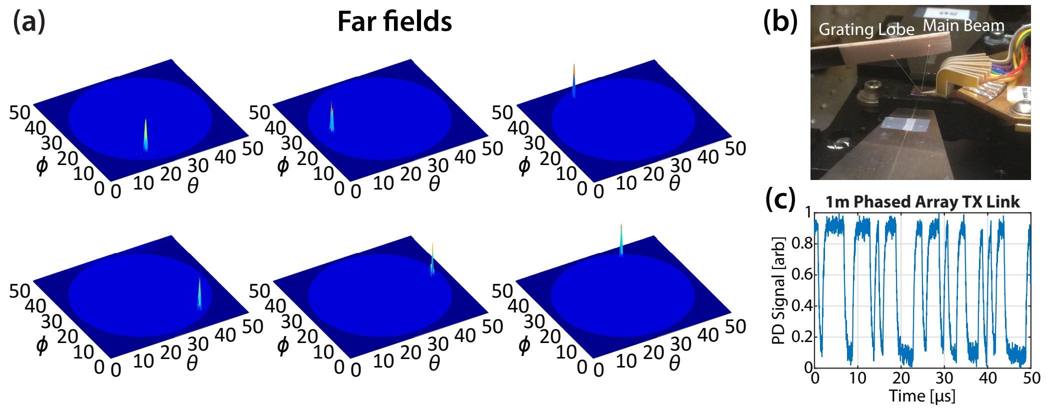

Figure 3-7: (a) Far field of the array at different thermal and wavelength tuning values. (b) Main beam and grating lobe output of the array seen with an IR card. (c) Free-space data link created with the phased array as a transmitter and a photodetector placed 1 m away.

after one meter and was received by an InGaAs photodetector. Fig. 3-7(c) plots the signal captured by the photodetector, where data speed was mainly limited by the photodetector used in the experiment. This is the first demonstration of a lens-free transmitter free-space optical data link using a phased array. Farther distances could be enabled by using a lens at the photodetector for more efficient power collection.

3.2.2 LIDAR System with Phased Array

Utilizing the phased array shown in the previous section, a LIDAR system was created by using a transmitter (TX) and receiver (RX) phased array. A schematic of this system is shown in Fig. 3-8(a). It is similar to the system shown in Chap. 2. The LIDAR system consists of a single input to the chip which is a silicon inverse-taper edge-coupler. 10% of the input light is tapped off the input with a directional coupler to act as a local oscillator (LO). The remaining 90% of the light is input to a transmitting phased array that is incident to a target. The light that reflects off the target is collected with a receiving on-chip phased array and is beaten with the LO and input to on-chip balanced germanium photodetectors. The electrical signal is amplified off-chip with a transimpedance amplifier (TIA) and is input to an oscil-

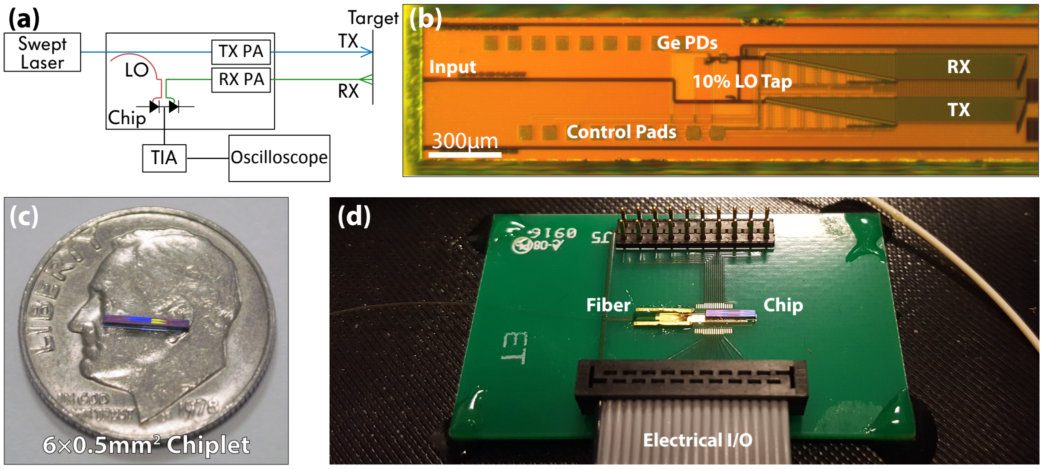

Figure 3-8: (a) Schematic of the on-chip LIDAR system with transmitting and receiving phased arrays. (b) Optical micrograph of LIDAR system. (c) Chiplet containing LIDAR system on top of a dime. (d) Packaged LIDAR system that was demonstrated at the 2016 DARPA Demo Day.

loscope for analysis. Fig. 3-8(b) shows an optical micrograph of the system with the major components labeled. The system is controlled using 9 electrical pads: 3 for the TX array, 3 for the RX array, 2 for the signal and bias of the balanced PDs, and 1 for ground.

To give a sense of size of this LIDAR system, Fig. 3-8(c) shows a $6{\times}0.5\,\mathrm{mm}^2$ chiplet that contains the system on top of a dime. The LIDAR system itself actually only has a footprint of $2.5{\times}0.5\,\mathrm{mm}^2$. This chiplet was packaged utilizing wirebonds from the on-chip pads to gold pads on a PCB and epoxying a fiber to the edge of the chip. The LIDAR operation of this packaged chiplet was demonstrated at the 2016 DARPA Demo Day in Washington D.C. A photo of the packaged device within a 3D printed housing is shown in Fig. 3-8(d).

In order to test the steered LIDAR operation of the device, three targets were set up in the laboratory at different incident angles from the chip as shown in Fig. 3-9(a). The targets were created with reflective tape. By steering the transmitting and receiving phased arrays simultaneously, each of the targets could be measured separately. The distance to each target is shown in Fig. 3-9(b), and the raw data from the photodetectors are shown in Fig. 3-9(c). A clean frequency is seen in the raw data that was proportional to the distance to the target. No noticeable cross-talk between targets was measured, indicating that the beam was confined to be incident on a single target. Unfortunately, the angle range shown, about 20°, was near the limit that could be measured due to thermal cross-talk between the phase shifters and the balanced photodetectors. Future iterations of the device will ensure that the photodetectors are thermally isolated from the phased arrays. Alternatively, electro-optic phase shifters will be utilized.

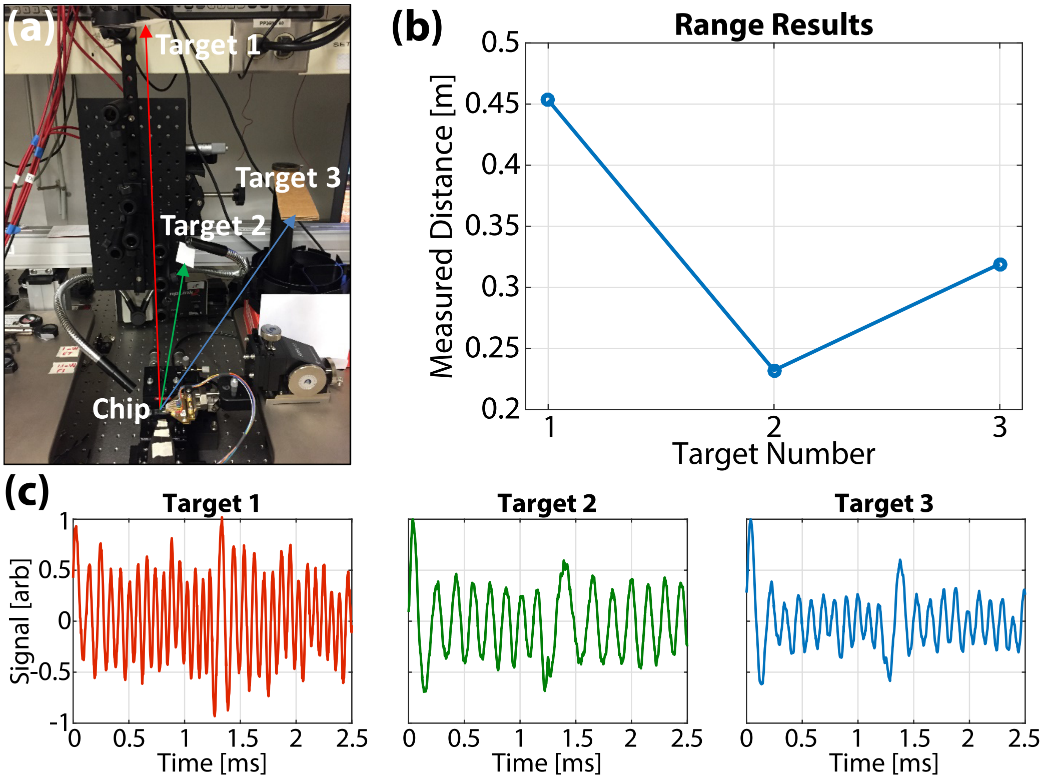

Figure 3-9: (a) Image of targets in the lab placed at different angles away from the chip. (b) Ranging results of each target. (c) Raw photodetector data for each target.

3.3 Conclusion

In conclusion, a phased array with a grouped cascaded phase shifter architecture has been demonstrated. A spot size of 0.85°×0.18° and a steering range of 46°×36° were measured. A FMCW LIDAR system was created with a transmitting and receiving phased array, and initial results were shown. This FMCW LIDAR system was the first demonstration of a coherent integrated LIDAR system based on optical phased arrays and paves the way for LIDAR on a chip technology in the future.

Chapter 4

High Power Silicon Nitride Phased Arrays

The silicon-based phased array shown in Chap. 3 was power limited because of two-photon absorption and free-carrier absorption. The goal of this chapter is to establish the framework of passive silicon nitride (SiN) only phased arrays and demonstrate a high-power phased array that could not be achieved in silicon. Silicon nitride is a CMOS compatible material and has a higher optical bandgap than silicon [51] and a low $\chi^{(3)}$ non-linearity [52]. Because of this, silicon nitride waveguides can handle power on the order of watts [53], unlike silicon where two-photon absorption and free-carrier absorption dominates at powers of tens of milliwatts at 1550 nm. This property makes silicon nitride commonly used in integrated photonics for low-loss waveguides [54, 55], non-linear and quantum optics such as comb generation [56, 57], and quantum squeezing [58] and is also why silicon nitride was investigated here for high-output power phased arrays.

By utilizing silicon nitride in the splitter distribution network, the allowed input power to the array can be much higher than in silicon. However, silicon nitride does have some disadvantageous qualities. The index contrast of silicon nitride waveguides is low, thereby limiting the minimum bending radius to around 150 μm as compared to 5 μm in silicon. The thermo-optical coefficient of silicon nitride is small [59], making a tree splitter architecture more desirable than a cascaded phase shifter architecture.

The fabrication process used here has two plasma-enhanced chemical vapor deposited (PECVD) silicon nitride layers that are 200 nm thick with a 100 nm gap between them. In runs that include silicon and silicon nitride, the first nitride layer is 100 nm above the silicon layer. This allows for waveguide transitions between the layers. The long-term vision for phased arrays incorporating silicon nitride is to create the tree splitter distribution network in silicon nitride waveguides, then transition to a silicon layer for individual antenna phase shifting and emission.

4.1 Splitter Design

In order to split and distribute the input light into the antennas, 1×2 couplers were investigated. Higher order 1×N couplers were ruled out because of the inherent phase non-uniformity in the ports seen in many types of 1×N couplers [60]. Such non-uniformity would require phase compensation either actively or passively and would add complexity to the system. Simple adiabatic Y-junctions [61] were first investigated but, because these splitters require a small minimum spacing, they performed inadequately with efficiencies less than 90% when simulated with the constraints of our design rules. Instead, multi-mode interference (MMI) splitters were designed. Two different sizes were designed, a smaller MMI for the last stage of the tree to minimize evanescent crosstalk and a larger, more efficient MMI for the rest of the stages. Fig. 4-1(a) shows a to-scale rendering of the designed large MMI splitter. It consists of a waveguide input to a larger multi-mode waveguide region with two output waveguides. The input waveguide can support multiple modes, but only the fundamental mode should be input into the device. Consequently, an adiabatic linear taper must be used to achieve the desired waveguide size without exciting higher order modes. When the light from the input waveguide enters the larger multi-mode region, it excites numerous modes. The width and length of the multi-mode region are designed such that when these modes are excited, the input field will be self-imaged in two locations as seen in Fig. 4-1(b). The two output waveguides are then positioned at these locations. The approximate length of a 1×2 MMI splitter is $L_{MMI} = \frac{3\pi}{8\Delta\beta}$, where

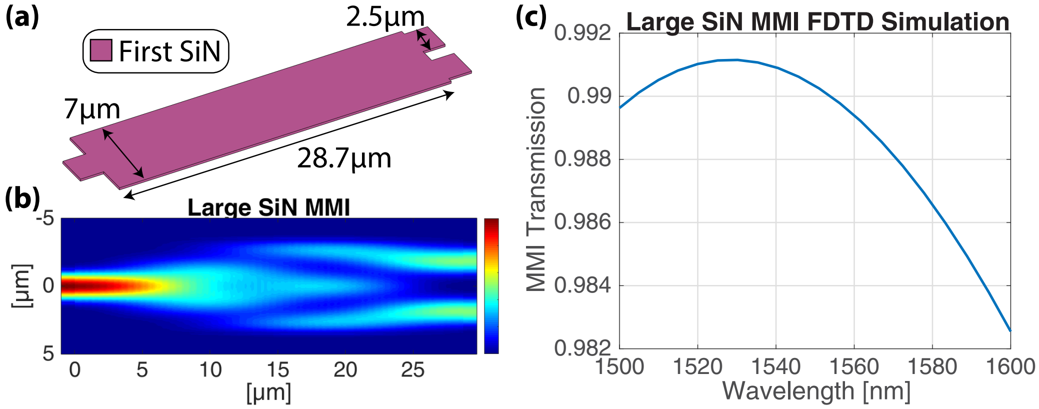

Figure 4-1: (a) 3D rendering of a silicon nitride MMI splitter showing critical dimensions. (b) EME simulation of the electric field intensity throughout the splitter. (c) FDTD simulation results of the silicon nitride MMI splitter.

$\Delta\beta$ is the difference of the propagation constants of the first and second mode of the multi-mode waveguide [62]. This assumes that the excitation of modes other than the fundamental and second order mode are negligible. Though this approximation is useful for intuition and estimation of the correct length of an MMI, a combination of eigenmode expansion (EME) and rigorous finite-difference time-domain (FDTD) simulations were used in this work to design the MMI length and the gap between the output waveguides. Because MMIs are based on multi-mode interference, they can suffer from small optical bandwidths as the effective index difference between the fundamental and higher-order modes changes with wavelength due to both material and waveguide dispersion. However, in silicon nitride, because the index contrast is low, the effective index differences do not change greatly with a change of wavelength. This allows for a splitter that is relatively broadband. Fig. 4-1(c) shows the MMI efficiency as simulated in FDTD. Efficiencies of over 98% were observed within the 1500-1600 nm band, showing the device works well in the S, C, and L bands. At a wavelength of 1550 nm, 99% efficiency is achieved.

The desired pitch of the silicon nitride array antennas is 4 μm. The larger MMI designed above is 7 μm wide which when used as a last stage splitter only allows for a 1 μm gap. This is not large enough to ensure that there is not crosstalk between adjacent MMIs. In order to prevent this, a smaller MMI was designed whose width of 5 μm allows for a 3 μm gap between splitters at the last stage as seen in Fig. 4-2(a). This gap is large enough to ensure that there is no evanescent coupling between adjacent MMIs. Fig. 4-2(b) shows the efficiency of the small MMI in FDTD. It is limited to slightly over 94% at 1550 nm, but because there is only one stage of these splitters in the splitter tree, it was considered adequate.

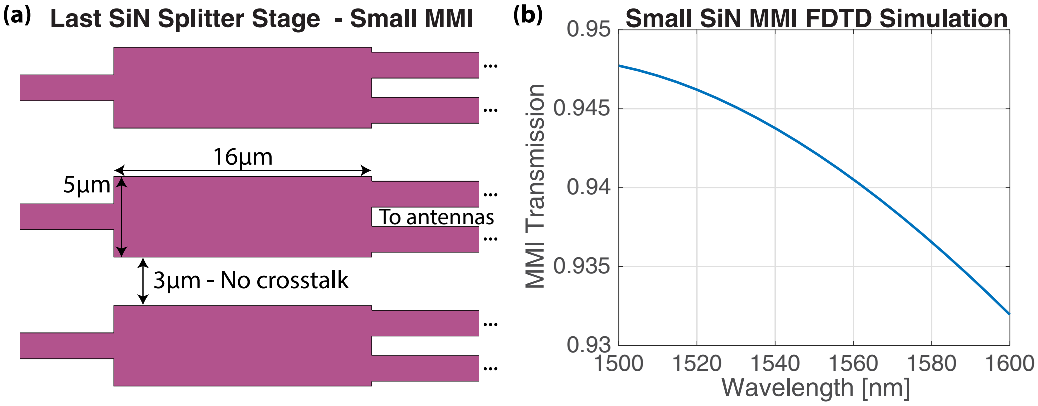

Figure 4-2: (a) 3D rendering of the small silicon nitride MMI splitter in the final splitter tree stage. (b) FDTD simulation results of the small silicon nitride MMI splitter.

In order to couple into the splitter distribution network, an on-chip edge-coupler based on an inverse-taper was utilized. This inverse-taper was realized in the first nitride layer for ease of transition into the single-layer MMI splitters. The input width of the inverse-taper was 320 nm based on simulated modal overlaps with an input SMF-28 fiber mode. The inverse-taper was linearly tapered over 300 μm to a single-mode width of 1.5 μm. This taper length was determined utilizing EME simulations to ensure minimal loss. The MMI tree utilized sinusoidal-shaped s-bends between the MMI stages. These s-bends were designed such that the largest bend radius, which occurs at the beginning and end of the s-bend, was 200 μm or greater. Tapers were used in-between stages to convert the single-mode routing waveguide width to the input width of the MMIs. A 50 μm-long taper was used for the large MMIs, whereas no taper was needed for the small MMIs since the routing and input waveguide widths were the same. An image of the layout of a six-layer tree to a 4 μm antenna pitch is shown in Fig. 4-3(a). Fig. 4-3(b) shows the last two stages of the splitter tree. In theory, this distribution scheme should produce low-loss results. Considering the six-layer splitter tree, the estimated loss from the splitters are $\eta_s = (0.99)^5(.94) = 0.89$. The approximate length of this distribution tree is about 0.14 cm, so, assuming a moderate propagation loss of 2 dB/cm, the waveguide loss is $\eta_r = 0.14\,cm \times 2\,dB/cm = 0.93$. Thus, we get a total efficiency of $\eta_t = \eta_s \eta_r = 0.83 = 0.81\,dB$ loss.

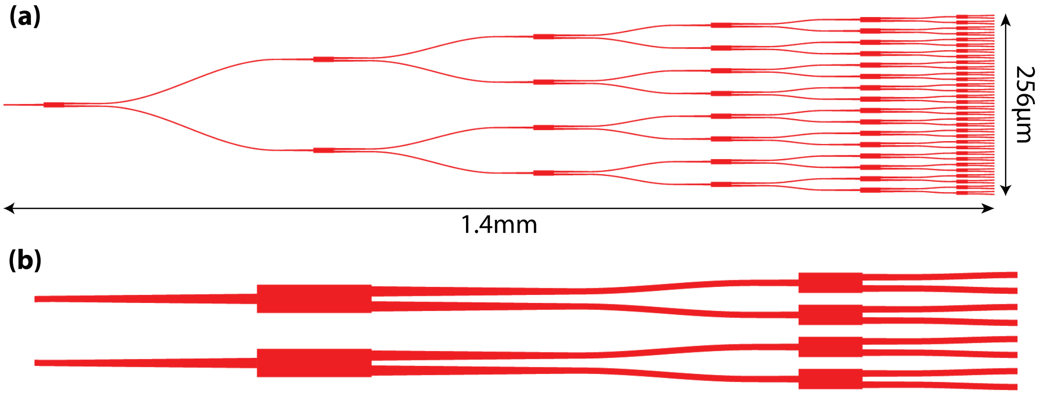

Figure 4-3: (a) Layout of a six-layer tree to a 4 μm antenna pitch. (b) Close-up of the last two stages showing the use of the small MMI.

4.2 Antenna Design

Silicon nitride antennas can be realized similarly to those in silicon by creating inward perturbations on the side of the waveguide. In this section, mono-layer and dual-layer designs are presented. The mono-layer design has no layer transitions and allows for a low-risk approach to test our silicon nitride splitter tree but suffers from symmetric emission in the vertical direction. The dual-layer design allows for uni-directional emission because vertical symmetry can be broken. This has many benefits for phased arrays in order to increase power output.

4.2.1 Mono-Layer Antenna Design

For the mono-layer design, the width of the antenna was chosen to be 1.5 μm, the same as the single-mode routing waveguide for simplicity (Fig. 4-4(a)). The antenna design process is similar to that in Sec. 3.1.3. The antenna is perturbed inwards periodically to scatter light. The period of this perturbation is designed such that the light emits upwards at 1550 nm. It was decided to keep the perturbation length fixed at 500 nm and alter the non-perturbed length in order to maintain straight-up emission as shown in Fig. 4-4(b). The perturbation pitch and perturbation strength as functions of perturbation distance are plotted in Fig. 4-4(c-d). As done in Chap. 3, the perturbation strength is found by simulating a waveguide in FDTD with a few perturbations and assessing how much light remains in the waveguide after the perturbations. An example simulation domain is shown in Fig. 4-5(a). In silicon nitride, lower perturbation strengths such as $-30\,\mathrm{dB}/\mu\mathrm{m}$ have perturbation values around 100 nm. This is very different than the silicon antennas where similar strengths require perturbations on the order of 10 nm. This shows a benefit of using silicon nitride antennas since the feature sizes are larger and are easier to resolve in a wafer-scale projection lithography based fabrication process. Furthermore, the slope of perturba-

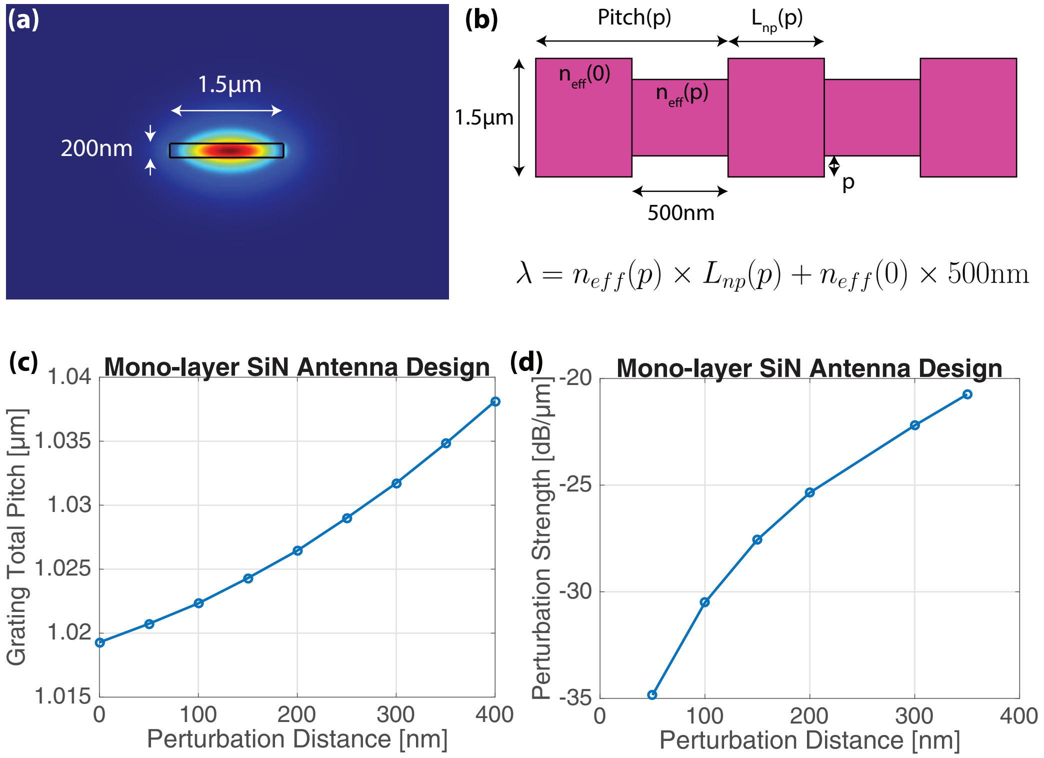

Figure 4-4: (a) Cross-section of silicon nitride waveguide mode. (b) Illustration of mono-layer nitride antenna. (c) Needed perturbation pitch for upwards emission as a function of perturbation. (d) Antenna strength as a function of perturbation.

tion strength against perturbation distance is much less than in silicon meaning that a slight bias of perturbation distance in fabrication is not as detrimental and would not greatly increase or decrease the perturbation strength throughout the antenna. The antenna pitch and strength FDTD simulation results were fitted and used for antenna synthesis in layout.

Though a full >0.5 mm antenna cannot be simulated with FDTD, a portion can be simulated in order to confirm that the antenna emits upwards and that the far field is centered on the main beam. Fig. 4-5(a) shows the domain of an FDTD simulation in order to check the far field. This is actually the same simulation used in order to find the perturbation strength. It consists of a waveguide with 12 perturbations on it. There are three discrete Fourier transform (DFT) planes: one at the end of the waveguide to check the perturbation strength, one at the top of the domain to observe the emission pattern in the far field, and one on the side to measure how much power radiates completely sideways. Fig. 4-5(b) shows the far field of the 300 nm perturbation antenna (with a constant pitch). As designed, it emits straight upwards. The power is centered so the main lobe will have a greater power than the side lobes.

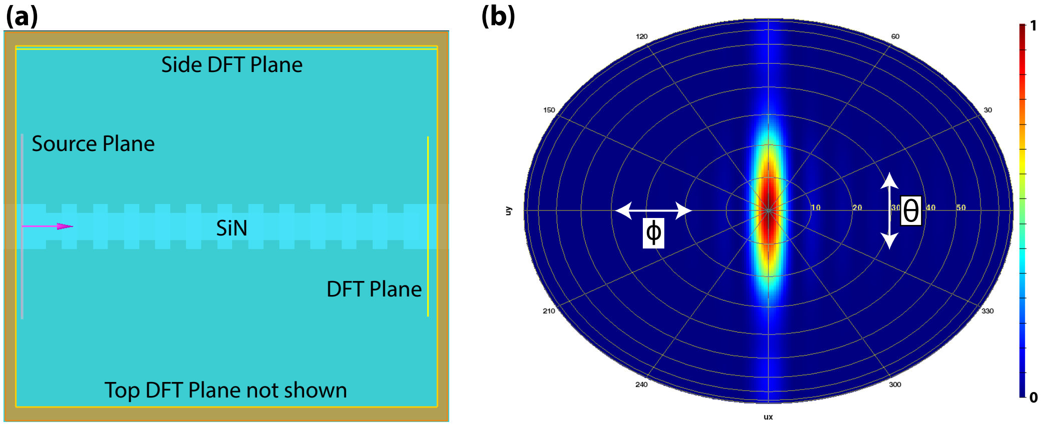

Figure 4-5: (a) FDTD domain of a small test antenna with one source plane and three DFT planes. (b) Far field of the antenna emission.

4.2.2 Dual-Layer Antenna Design

In our fabrication process, there are two layers of silicon nitride with a gap of 100 nm between them. This allows for the design of uni-directional antennas that utilizes a dual-layer waveguide that breaks vertical symmetry. The concept for uni-directionality with multiple layers is well known in fiber grating couplers and used in a variety of platforms such as monolithic CMOS [63], SiN-on-Si [64], and Ge-on-Si [65]. The basic concept is to have scattering elements that are offset vertically and horizontally. If these offsets are $\lambda/4$, constructive interference will occur in the upwards direction and destructive interference will occur in the downwards direction. Like the mono-layer antenna design, inwards perturbations on a waveguide can act as scattering elements. By having two perturbed waveguides on top of each other with a gap between, they can be vertically and horizontally offset. Fig. 4-6(a) shows a rendering of a dual-layer antenna. Two identical silicon nitride antennas are placed on top of each other with a horizontal offset between them. However, these antennas are not the same as the mono-layer antennas, and the entire antenna must be designed with a similar process as before.

The first step in designing the uni-directional antenna was to determine the horizontal offset needed. To find this, FDTD simulations of an antenna with a perturbation of 100 nm was used with perturbed and non-perturbed lengths that were

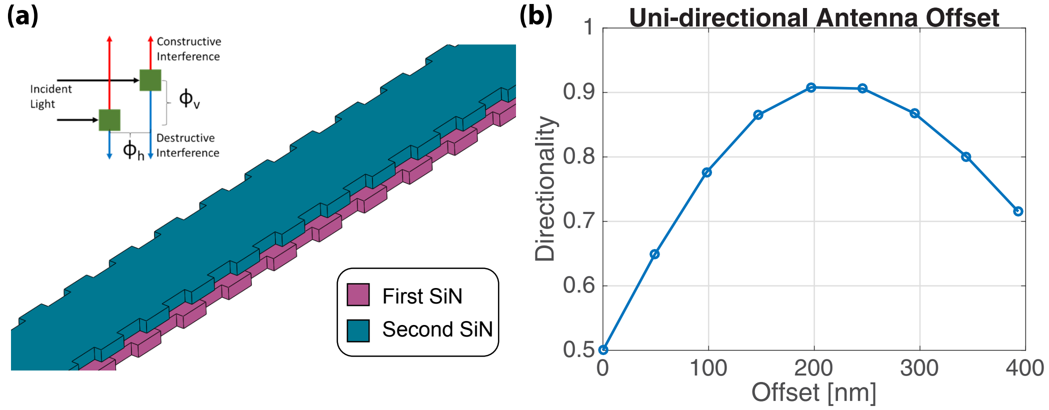

Figure 4-6: (a) Rendering of a uni-directional antenna showing the two offset silicon nitride layers. (b) Uni-directionality of the antenna as a function of horizontal offset.

estimated to emit straight-up. The offset between the first and second layers was swept, and the resulting directionalities of the antenna are plotted in Fig. 4-6(b). At an offset of approximately 210 nm, over 90% of the light is emitted upwards. This is the optimal offset for a wavelength of 1550 nm, and the directionality is limited to around 90% because the vertical offset between the two layers is not $\lambda/4$. In our platform, the vertical offset is constrained to be optimum for the laser devices.

Now that the offset between the two layers has been determined, the rest of the antenna can be designed. This process is similar to the mono-layer design. Fig. 4-7(a) shows a single period and the relevant lengths and cross-sections within it. The non-perturbed section length, L_f, is fixed at 500 nm. At this point, the only length that is not determined is the length of the perturbation, $L_p(p)$, where p is the perturbation value. In order to find this length, the antenna is designed to emit straight-upwards, i.e. the optical length of a period is equal to a wavelength. There are four cross-sections within a single period as shown in Fig. 4-7(b-e). Two of the cross-sections are when either the top or the bottom nitride is perturbed. Assuming the two nitride layers have similar indices of refraction, these cross-sections are mirror images of each other and can be described by a single effective index, $n_a(p)$. Another cross-section is when there is no perturbation that has a constant effective index, n_{full}. Finally, there is a cross-section that both the top and bottom nitride layers are perturbed which is described by $n_s(p)$. $n_a(p)$ and $n_s(p)$ are both functions of the perturbation value and

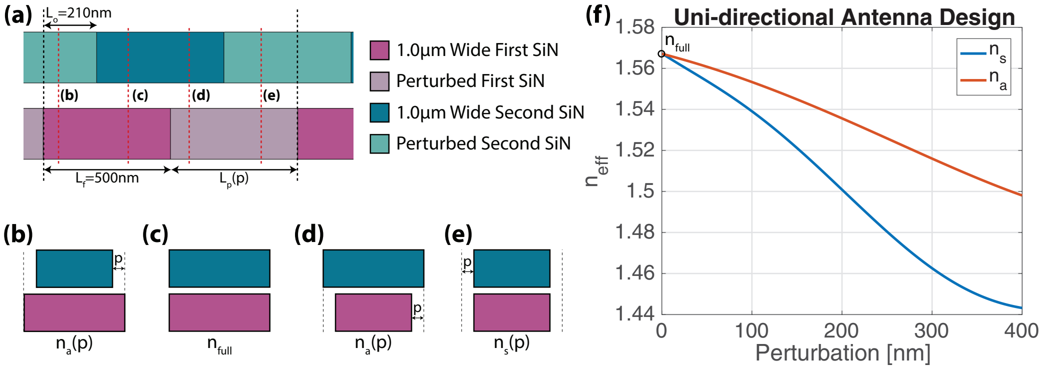

Figure 4-7: (a) Single period of the dual-layer antenna with fixed dimensions labeled. (b-e) Cross-sections throughout the antenna period with relevant effective indices. (f) Eigenmode solver results of the effective indices as a function of perturbation.

can be solved for in a 2D eigenmode solver. Fig. 4-7(f) shows the $n_a(p)$ and $n_s(p)$ values as a function of perturbation. When the perturbation value is 0, both $n_a(p)$ and $n_s(p)$ are equal to n_{full}.

All of these quantities can be related by defining the optical length to be equal to a wavelength as shown in Eq. (4.1). Then, $L_p(p)$ can be solved for as shown in Eq. (4.2).

$$\lambda \equiv L_o n_a(p) + (L_f - L_o)n_{full} + L_o n_a(p) + (L_p(p) - L_o)n_s(p) \rightarrow \tag{4.1}$$

$$L_p(p) = \frac{\lambda + L_o(n_{full} + n_s(p) - 2n_a(p)) - L_f n_{full}}{n_s(p)} \tag{4.2}$$

With all of the lengths designed for a given perturbation, the last step is to determine the perturbation strength at each perturbation. This is carried out in the same way as the mono-layer antenna, that is, it is found by simulating a waveguide with a few perturbations and determining how much light remains in the waveguide. After finding the perturbation strength and lengths as a function of perturbation, they are fit to polynomial functions and used for antenna synthesis in layout.

Finally, the far field of a portion of the antenna in the upwards and downwards direction can be analyzed. This is shown in Fig. 4-8(a-b) for 16 periods of the 100 nm perturbation antenna. The upwards direction has a single lobe that is slightly wider than the mono-layer design but is still centered. The downwards direction has an order of magnitude less peak power, and the total directionality of this portion of the antenna is calculated to be 91%.

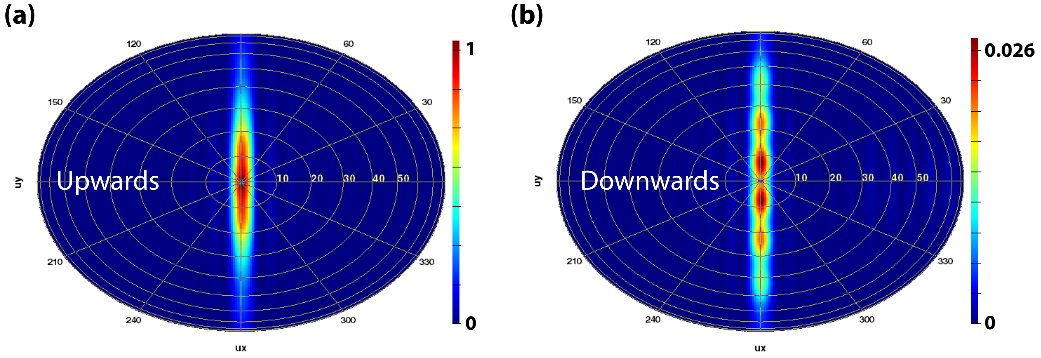

Figure 4-8: Far field in the (a) upwards and (b) downwards direction of 16 periods of the 100 nm perturbation uni-directional antenna.

4.3 Experimental Results

The experimental results presented in this section were measured on a single passive silicon nitride reticle. The chips were fabricated on a 300 mm silicon wafer with a 6 μm buried oxide (BOX) under the first layer of silicon nitride. It contains two layers of silicon nitride as described before (and shown in [66]). There is a dicing trench that etches down to the silicon handle wafer that allows for dicing and fiber edge coupling.

4.3.1 Splitter Results

In order to experientially test the insertion loss of the MMI splitters, an unbalanced tree was fabricated, and the cutback method was employed. An illustration of an unbalanced tree is shown in Fig. 4-9(a). Each output of the unbalanced tree has passed through a different number of splitters. When plotting the transmission of each output on a graph as a function of the number of splitters that the path went through, the slope of the line will be the insertion loss of the splitter. Fig. 4-9(b) shows an optical micrograph of the measured unbalanced tree, and Fig. 4-9(c) plots the results of the cutback method on the small silicon nitride MMI. The slope of

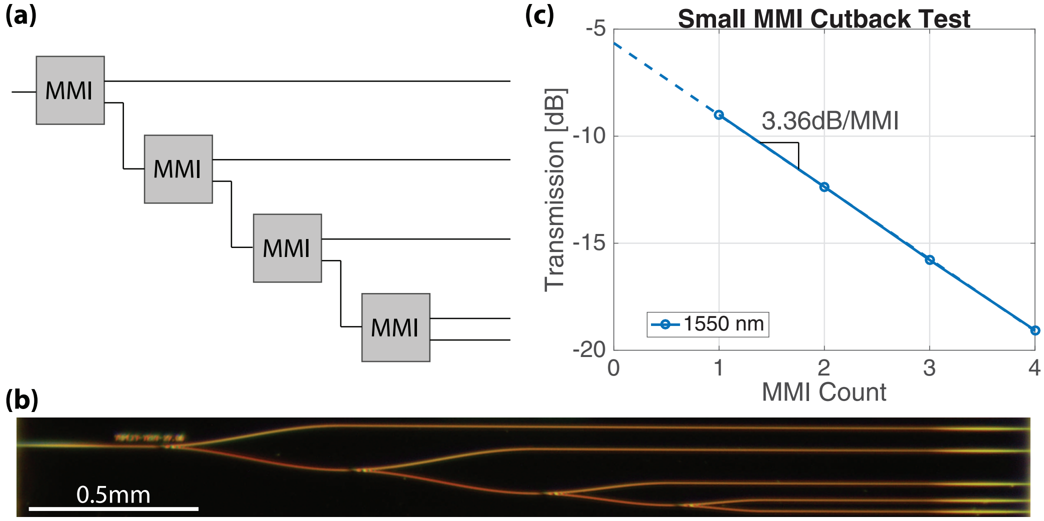

Figure 4-9: (a) Illustration of an unbalanced tree used to measure the MMI splitter insertion loss. (b) Optical micrograph of fabricated unbalanced tree. (c) Experimental measurements showing an MMI insertion loss of 0.36 dB for the small MMI.

the line is 3.36 dB/MMI. The 3 dB portion is expected because of the 1×2 splitter operation. Thus, the 0.36 dB is the excess insertion loss.

The cutback method was carried out on both the small and the large MMI splitters for different wavelengths, and the results are shown in Fig. 4-10(a-b). The small MMI has an efficiency around 92% at a wavelength of 1550 nm which is close to the simulated value of 94%. The efficiency of the large MMI at 1550 nm is around 98% which is also close to the simulated value of 99%. However, the accuracy of the large MMI measurement may be compromised by only having 4 layers in the unbalanced tree. Because the MMI has such low loss, in order to have a more accurate measurement, more tree layers should be used in the future. We see the 98% as a lower-bound of the efficiency. Overall, these experimental results for the silicon nitride MMI splitters show that the devices perform similar to simulation.

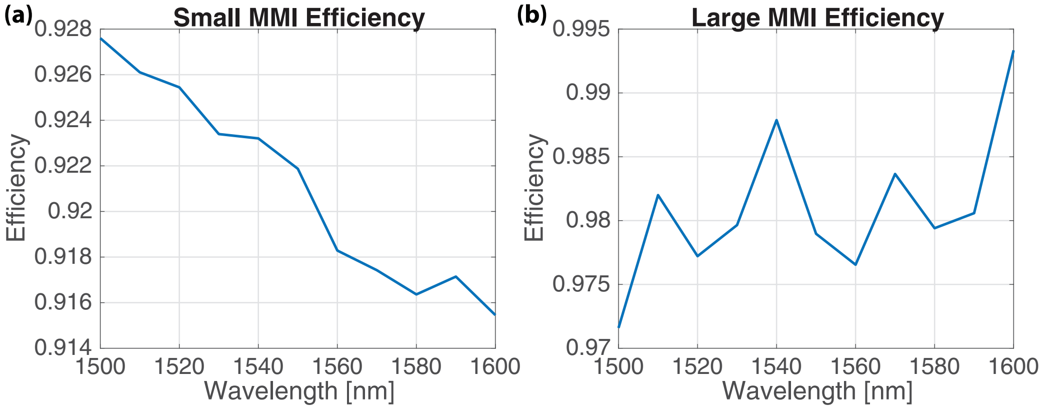

Figure 4-10: Measured (a) small and (b) large nitride MMI splitter efficiency as a function of wavelength using the cutback method.

4.3.2 Uni-Directional Antenna Results

Individual uni-directional antennas without a splitter tree were included on the mask in order to analyze antenna performance and directionality. Individual mono-layer antennas were also included as a control. In order to test the uni-directionality, the interaction between the downwards emitted light and the silicon substrate can be measured. This idea is shown in Fig. 4-11(a). The downwards emission will enter the substrate and reflect multiple times producing many possible paths. This causes rings in the far field since at certain angles these reflections will constructively and destructively interfere as shown in the illustration in Fig. 4-11(b). This illustration is for a bi-directional point source emitter. An individual antenna will be confined in a single dimension because the antenna acts as a one-dimensional aperture. This allows for a portion of the rings to be seen in the unconfined dimension in the far field. The far field of the mono-layer antenna is shown in Fig. 4-11(c). The rings caused by the bi-directionality of the antenna is clearly seen as expected. The far field of the uni-directional antenna is shown in Fig. 4-11(d). Almost no rings are seen in the far field showing qualitatively that the antennas are uni-directional. There are a few ring fringes on the side of the antenna emission showing that some angles are not as uni-directional as others. This is expected from the simulated far fields in Fig. 4-8(a-b) since the emission at the larger angles, though smaller, has less directionality which results in fringes with greater visibility.

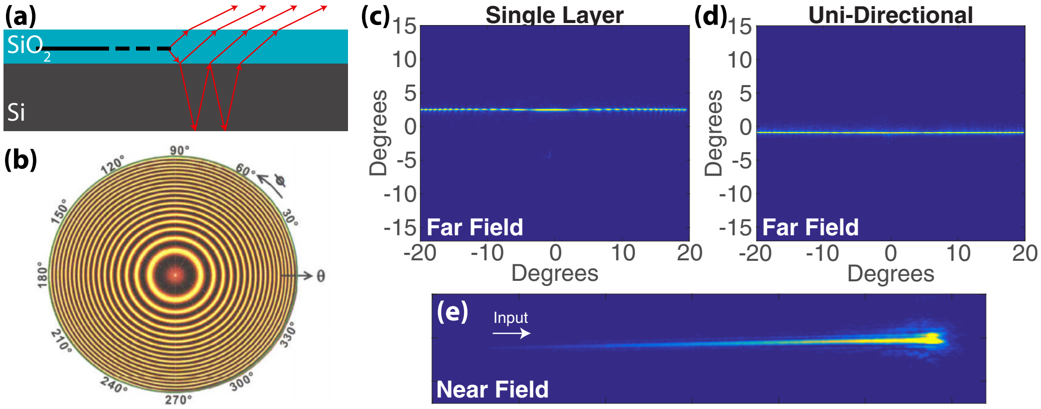

Figure 4-11: (a) Illustration showing how reflections within the silicon substrate causes multiple paths that interfere in the far field. (b) Simulated far field of a point source showing the rings caused by the interference of the multiple paths. From [48]. (c-d) Measured far fields of a mono-layer bi-directional individual antenna and a dual-layer uni-directional individual antenna. (e) Near field of an individual 1 mm-long uni-directional antenna.

Fig. 4-11(e) shows the near field of the 1.0 mm-long uni-directional antenna. This antenna was designed to emit uniformly, but it can be seen that most of the emission occurs in the later portions of the antenna. This was due to a layout error. During the antenna synthesis, the wrong perturbation sizes were used and the beginning of the antenna was too weak. This does not effect the uni-directionality but does increase the far field confinement, since the effective one-dimensional aperture length is decreased. Some power is also lost since not all of it is radiated. Because there was not an output on the antenna test structure, the power lost cannot be accurately measured. This layout error has been fixed for future runs.

4.3.3 Phased Array Results

Fig. 4-12(a) shows an optical micrograph of a silicon nitride phased array with 64 antennas with a pitch of 4 μm (500×264 μm^2 aperture). This is a phased array with mono-layer antennas because of the layout error mentioned in the uni-directional antennas. This micrograph is of a chiplet that was diced out of a larger chip that was packaged by epoxying a cleaved SMF-28 fiber to the inverse-taper edge-coupler. To gain a sense of this chiplet scale, a photo of a similar chiplet on top of a dime is shown in Fig. 4-12(b). A box was 3D printed that allowed the placement of the chiplet and a fiber output. The final packaged device within the box is shown in Fig. 4-12(c). This device was demonstrated for the 2016 DARPA Demo Day in Washington D.C.

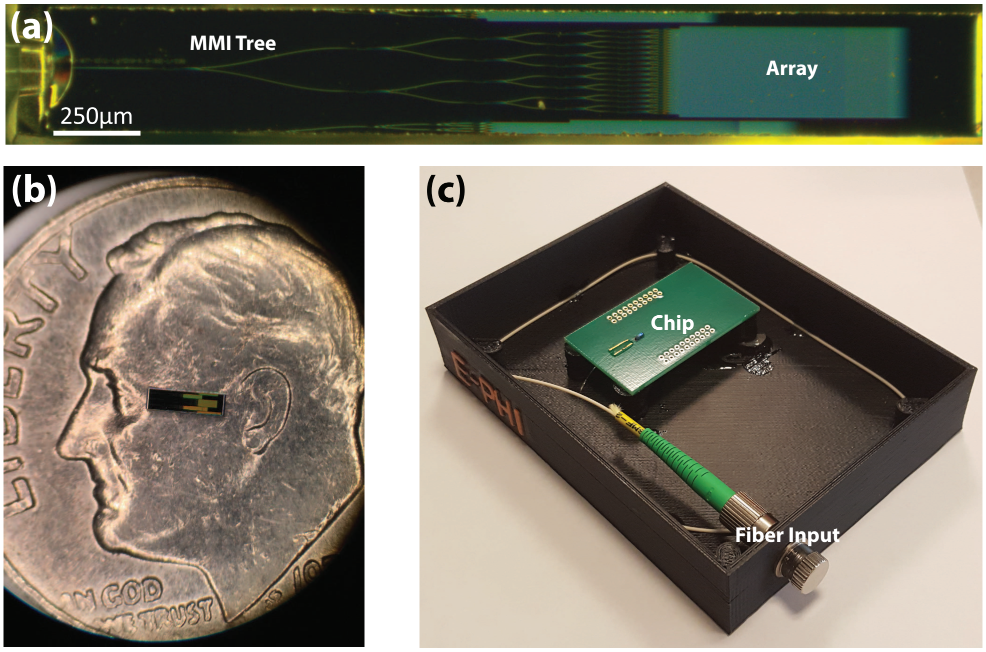

Figure 4-12: (a) Optical micrograph of the 500×264 μm^2 silicon nitride array. (b) Image of phased array chiplet on top of a dime. (c) Image of the packaged phased array chiplet that was demonstrated at the 2016 DARPA Demo Day.

In order to characterize the output of the phased array, a full chip was used instead of a packaged chiplet. A lensed fiber with a 6.5 μm spot diameter ($1/e^2$) was placed at the facet to couple to the edge-coupler with 1550 nm light. The edge-coupler efficiency with this fiber was estimated to be -2.15 dB, based on measurements of a straight waveguide. Fig. 4-13(a) shows three of the five output beams of the phased array on an IR card. As seen in the figure, the main beam contains the majority of the output power.

The near field of the phased array is shown in Fig. 4-13(b) utilizing an IR camera (Goodrich SU640KTS-1.7RT). Care was taken to ensure that the camera was not saturated by utilizing a variable optical attenuator to decrease the input power to the array. Individual antennas have near uniform power at the beginning of the antenna, showing that the splitter distribution network worked as designed. An exponential decay is seen in the antenna dimension. This is expected since the antennas were designed to have a constant perturbation strength with a 5% power at the end of the 500 μm antenna. A constant perturbation strength over a hyperbolically increasing perturbation strength was chosen in order to mitigate any risk associated with the antenna in this first silicon nitride fabrication run. The main risk of a uniformly emitting antenna is having the pitch not change correctly with the increase of perturbation strength throughout the antenna. This greatly increases the spot size since different locations of the antenna will emit at different angles. The near field image shows about 15% power at the end of the array, indicating that the antennas are weaker than designed. This is easily fixed in upcoming iterations.

Fig. 4-13(c) shows the imaged far field of the array. A full-width half-maximum (FWHM) spot size of $0.31^\circ \times 0.2^\circ$ is measured. This is near the theoretical diffraction limit of $0.31^\circ \times 0.16^\circ$. The reason for the increase of spot size in the antenna dimension is that the antennas were designed to have an exponential emission pattern instead of a uniform emission pattern. Fig. 4-13(d-e) show the horizontal and vertical cuts of the far field of the array. A *sinc*() function is seen in both cuts further indicating that the array is near diffraction limited. The side lobe suppression is $\sim$10 dB.

In order to test the high-power operation of the phased array, a 10 W Er/Yb doped

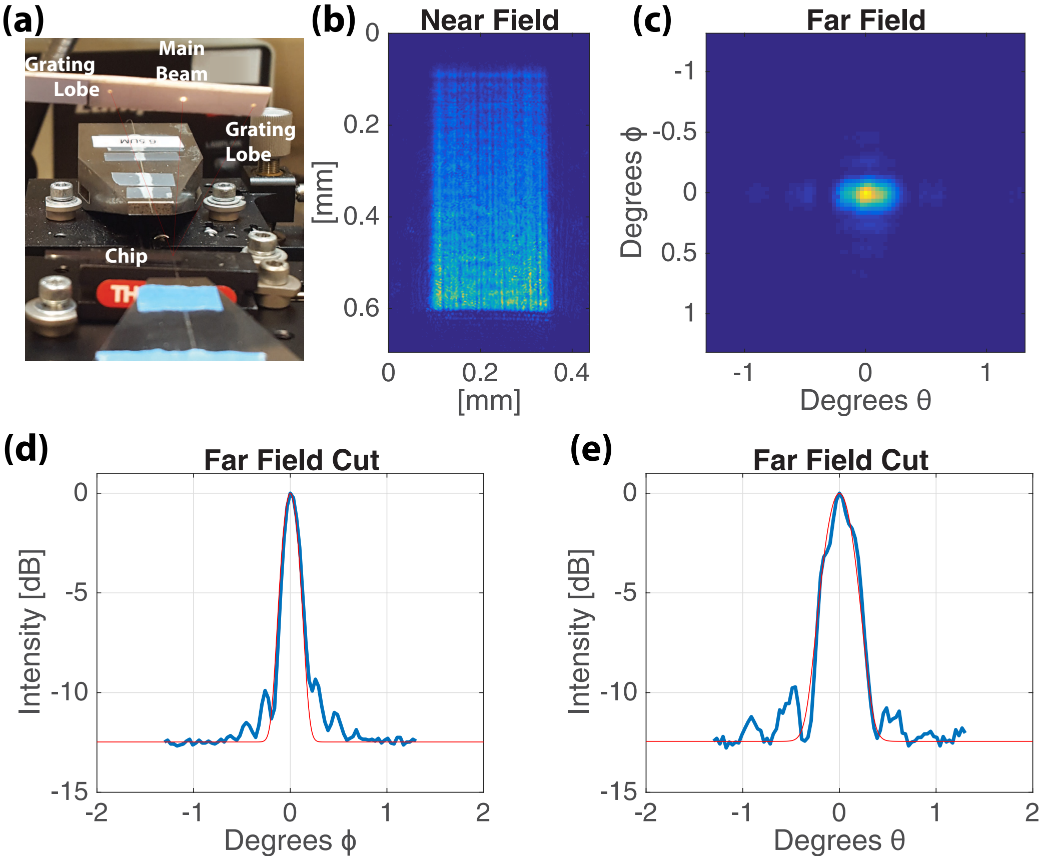

Figure 4-13: (a) Output beams of the phased array. (b) Near field and (c) far field of the silicon nitride phased array. (d-e) Vertical and horizontal intensity cuts of the far field.

fiber amplifier (Optilab EYDFA-40-R) was used as a source. 1584 nm light from a Keysight 81600B was used to pump the EYDFA. 1584 nm light instead of 1550 nm was used because the EYDFA operates in the L-band. The EYDFA has an output to a free-space beam with a beam diameter of 0.44 mm. In order to efficiency couple this to the phased array, a 0.38 mm beam diameter collimator to SMF-28 fiber was used (Thorlabs CFS2-1550-APC) to couple the free-space beam to a fiber. After coupling to SMF-28 fiber, a fiber-based polarization controller was used to ensure that the light was TE polarized, and then a lensed fiber was incident to the on-chip edge-coupler. A Thorlabs S145C integrating sphere photodiode power sensor was used to measure the power output of the main beam of the phased array. The maximum power output of the main beam was measured to be **520 mW** limited by the efficiency of the system, including the free-space collimator and the on-chip edge-coupler. 4 W was estimated to be in the fiber incident to the chip, giving a fiber to main beam efficiency of around $-9\,\mathrm{dB}$.

4.4 Conclusion

In conclusion, a high-power silicon nitride based phased array has been demonstrated. A spot size of $0.31^\circ \times 0.2^\circ$ and a main beam power of $520\,\mathrm{mW}$ were measured. This nearly diffraction limited spot and extremely high power indicate that the nitride splitter tree worked very well with minimal loss and phase noise. In the future, a hybrid optical phased array system in a silicon-nitride-on-silicon platform [67] with a silicon nitride splitting network and silicon phase shifters can be implemented. Within the silicon, individual antenna phase shifters can be realized using either the thermo-optic [19] or electro-optic [20] effect.

Chapter 5

Ultra-Large-Scale Passive Phased Arrays

In previous chapters, both active silicon and passive silicon nitride phased arrays were demonstrated. However, these phased arrays were relatively small-scale with aperture sizes of $500 \times 100\,\mu\text{m}^2$ and $500 \times 264\,\mu\text{m}^2$, shown in Chap. 3 and Chap. 4, respectively. Currently the smallest divergence angle measured in an optical phased array is 0.14° [21], which we estimate to be a $\sim 500 \times 500\,\mu\text{m}^2$ effective aperture. For LIDAR on a chip technology to be commercially viable, a large phased array aperture size is crucial. This purpose of this chapter is to demonstrate an ultra-large-scale optical phased array that has an aperture size of multiple millimeters.

There are two reasons that a large aperture is needed for LIDAR systems: one related to transmitting and the other to receiving. For transmitting, the aperture size determines the diffraction limited spot size and thus how much the beam diffracts while propagating. Commercial LIDAR systems today can range multiple hundreds of meters. In order to have adequate lateral resolution at those distances, a small beam size is needed. Fig. 5-1 shows the calculated full-width half-maximum (FWHM) beam size after propagating a modest 30 m as a function of aperture size.

With the phased array sizes described in the previous chapters, the beam size after 30 m is around 100 mm. A LIDAR device with this size of beam would have this lateral resolution at this distance. For autonomous vehicle applications, this

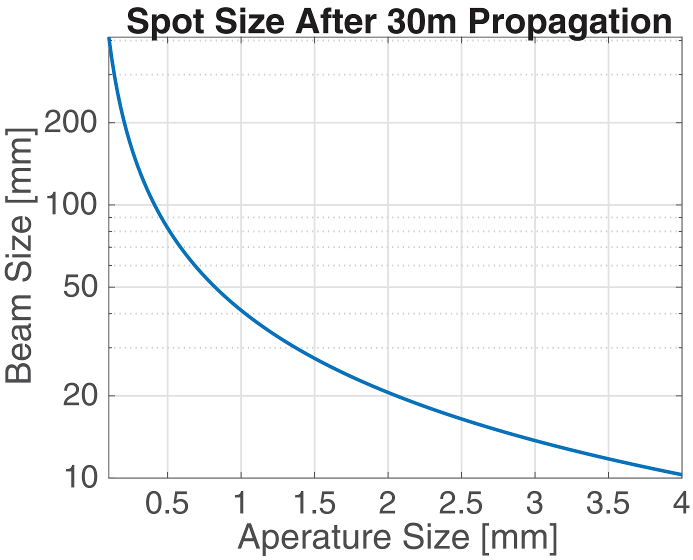

Figure 5-1: Beam size after 30 m of propagation as a function of aperture size.

resolution is not small enough to detect objects such as sign poles. Furthermore, if a target is smaller than this beam size, then not all of the light is reflected by the target, and power is lost.

The second reason that a large aperture is needed is in order to have a large receiving area for long-distance ranging. LIDAR systems are normally photon starved because the reflection from the target scatters in all directions. This makes the received power follow an inverse-square dependence of the target distance. From Eq. (1.1), the received power of the system is proportional to the area of the receiver and can allow for more light to be collected by the receiver.

5.1 Ultra-Large Silicon Phased Arrays

In order to test the scalability of optical phased arrays, passive phased arrays up to $4{\times}4\,\text{mm}^2$ in silicon were first fabricated. These phased arrays utilized a tree architecture with the 1×2 MMI-like splitter described in [68]. The measured insertion loss of this splitter within our fabrication process was $\sim$0.15 dB. The small bend radius of silicon waveguides allows for a compact tree distribution network that can utilize 90° bends instead of only sinusoid shaped s-bends. The full-etch based silicon antennas used were similar to those described in Sec. 3.1.3 but redesigned at a larger width in order to reduce the power of the grating lobes. Optical micrographs of the silicon $4{\times}4\,\mathrm{mm}^2$ phased array are shown in Fig. 5-2(a-b).

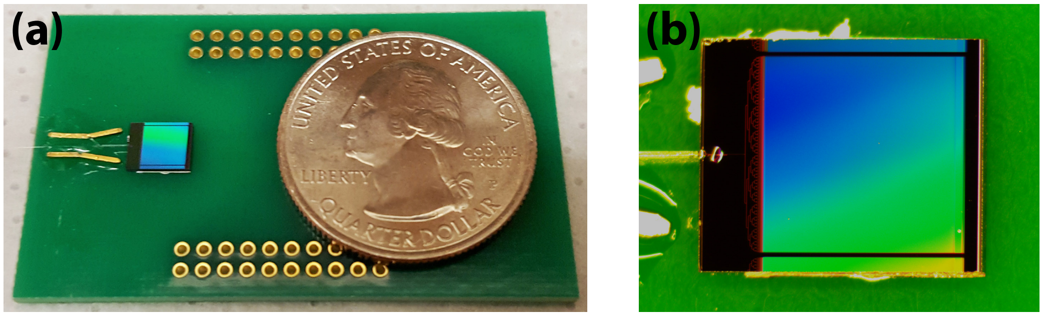

Figure 5-2: (a) Image of the silicon $4{\times}4\,\mathrm{mm}^2$ phased array next to a quarter. (b) Optical micrograph of the same phased array with epoxied input fiber.

The near field of the $2{\times}2\,\mathrm{mm}^2$ silicon phased array with uniformly emitting antennas is shown in Fig. 5-3(a). This phased array had a $2\,\mu$m antenna pitch with an antenna count of 1024. The near field is near uniform along the antenna dimension, indicating that the increasing antenna strength along the antenna is close to the designed value. Fig. 5-3(b) shows the far field of the phased array. A *sinc*() function is not observed along the array dimension, signifying that the silicon tree splitter network has strong phase noise. In the antenna dimension, a *sinc*() function is seen. Far field intensity cuts are plotted in Fig. 5-3(c). A FWHM spot size of $0.046^\circ{\times}0.055^\circ$ is measured where $0.04^\circ{\times}0.04^\circ$ is diffraction limited. Even though this array is close to the diffraction limit, strong side lobes at $-5.4\,\mathrm{dB}$ and a high noise floor are measured. This indicates that this phased array is emitting at many angles because of the phase noise within the tree splitter network. We attribute the source of this phase noise to the high index contrast of silicon. Fabrication noise within the silicon layer produces a large phase noise in the splitter network. With active tuning, this issue could likely be resolved. However, since only passive runs were available at this time, in order to try to fix this issue, large-scale phased arrays were then fabricated in silicon nitride. Silicon nitride is a low index contrast material which should result in lower fabrication induced phase noise.

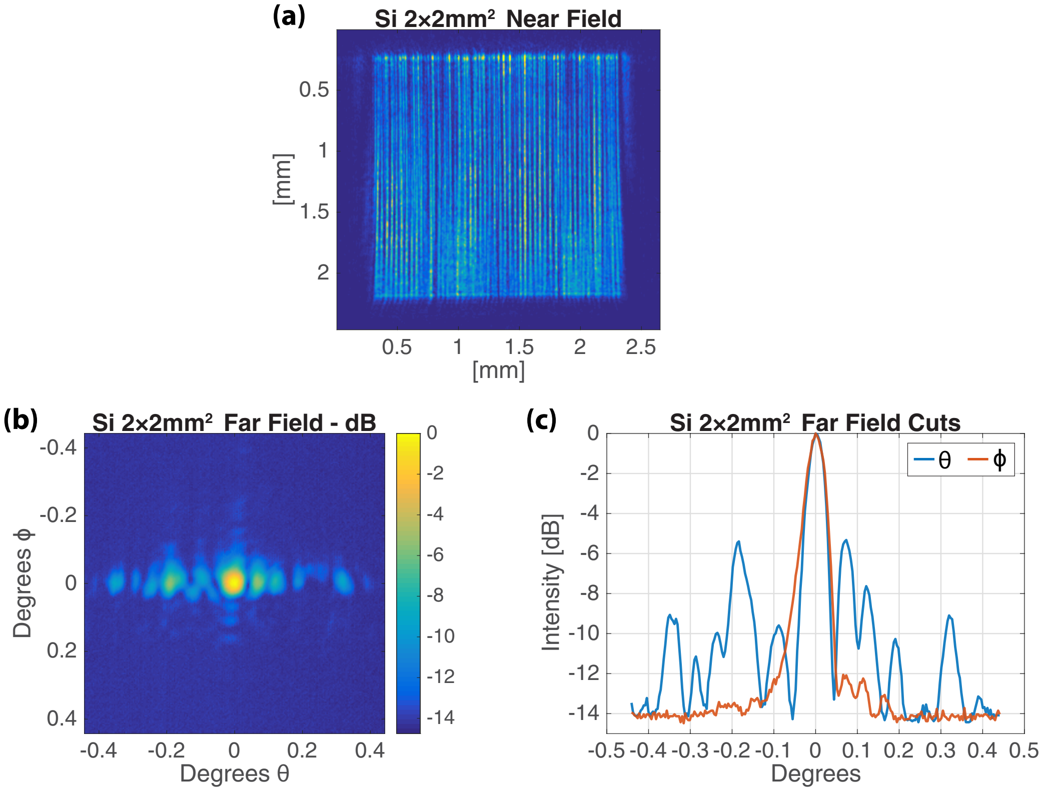

Figure 5-3: (a) Near field and (b) far field of the silicon 2×2 mm^2 phased array. (c) Far field intensity cuts in the array and antenna dimensions.

5.2 Ultra-Large Silicon Nitride Phased Arrays

Because of the phase noise seen in the passive large-scale silicon phased arrays, passive phased arrays in silicon nitride were fabricated. As before, array sizes up to 4×4 mm^2 were fabricated. These phased arrays utilized a tree architecture similar to those in Sec. 4.3.3. Optical micrographs of the silicon nitride 4×4 mm^2 phased array are shown in Fig. 5-4(a-b). The silicon nitride arrays utilized the MMI splitters described in Sec. 4.1. An antenna pitch of 4 μm was used. In the photographed device, there are 1024 antennas so the tree distribution network is ten layers. Because of the large bend radius needed in silicon nitride waveguides, the tree distribution network has a length of ∼4 mm, which is the same size of the array. Utilizing a thicker nitride layer could decrease the needed bend radius, and shorten the tree length.

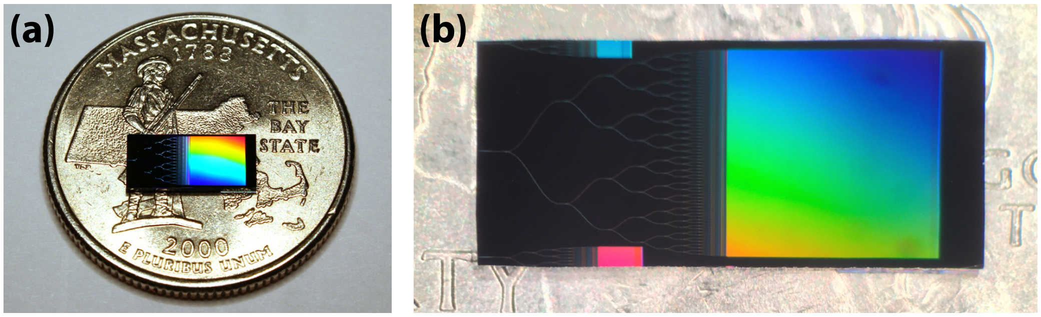

Figure 5-4: (a) Image of the silicon nitride 4×4 mm^2 phased array on top of a quarter. (b) Optical micrograph of the same phased array.

1550nm light was input into the device with a 6.5 μm spot diameter lensed fiber. Fig. 5-5(a) shows the resulting main beam on an IR card. The main beam is clean with no noticeable light on the side which indicates that the silicon nitride tree network has minimal phase noise unlike the silicon tree network. Fig. 5-5(b) shows an InGaAs IR camera image when the camera is placed directly in the path of the main beam at 0.05 m from the phased array. Here, the beam is relatively square because the beam has only propagated a short distance. The Fraunhofer distance of this array, given by $2D^2/\lambda$, where D is the largest dimension of the array, is 20 m so a *sinc*() distribution is not expected at this distance. After a propagation distance of 10 m, the beam closer represents a *sinc*() function (Fig. 5-5(c)). The tested propagation distance was limited by laboratory space. Even after a propagation of 10 m, the beam has not

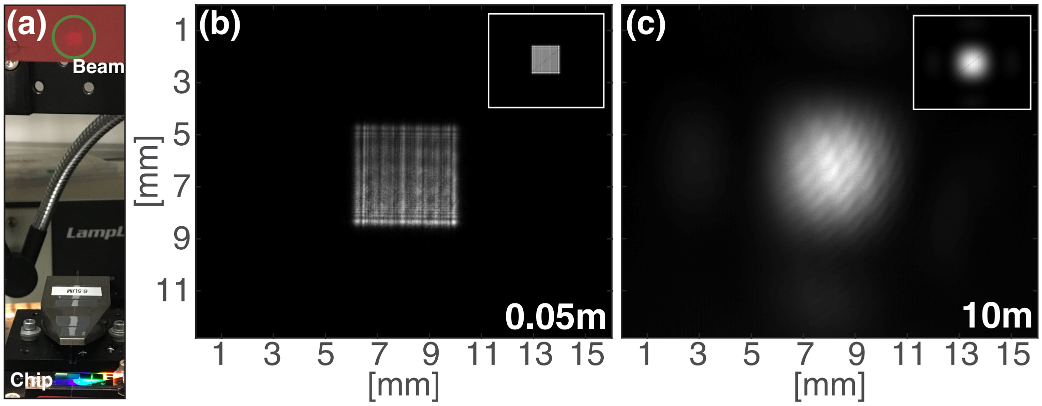

Figure 5-5: (a) Photograph of the main beam of the silicon nitride 4×4 mm^2 array on an IR card. (b) Main beam intensity measurement after approximately 0.05 m and (c) 10 m propagation. Insets show Fresnel propagation simulations in the same domain.

increased greatly in size due to the large aperture of the phased array. The physical FWHM beam size after 10 m is 3.4 mm. This is similar to a Fresnel propagation simulation of a 4×4 mm^2 uniform electric field propagating 10 m, which results in a 3.2 mm FWHM beam size. Fresnel propagation simulations are shown in the insets of Fig. 5-5(b-c) showing good agreement with the experimental measurements.

The far field of the array was measured with an InGaAs IR camera and a two-lens imaging system [21], and is shown in Fig. 5-6(a). A *sinc*() function is observed in both the antenna and the array dimensions, which is expected for a near diffraction limited square aperture. This indicates that little phase noise was accumulated in the silicon nitride tree and that the antenna elements were near identical. The FWHM spot size of the array was measured to be 0.021°×0.021°, whereas the theoretical diffraction limited spot size is 0.019°×0.019°. Intensity cuts of the spot along the array, θ, and antenna, ϕ, dimensions are shown in Fig. 5-6(b). Multiple side lobes are observed at the expected theoretical angular locations. A side lobe suppression of about 10dB is measured. This ultra-small spot size is over an order of magnitude smaller in area than the previous demonstration in [21] and allows for a long-range propagation. For context, after 100 m of propagation, the diameter of the beam should increase by only 3.7 cm based on the experimental spot size.

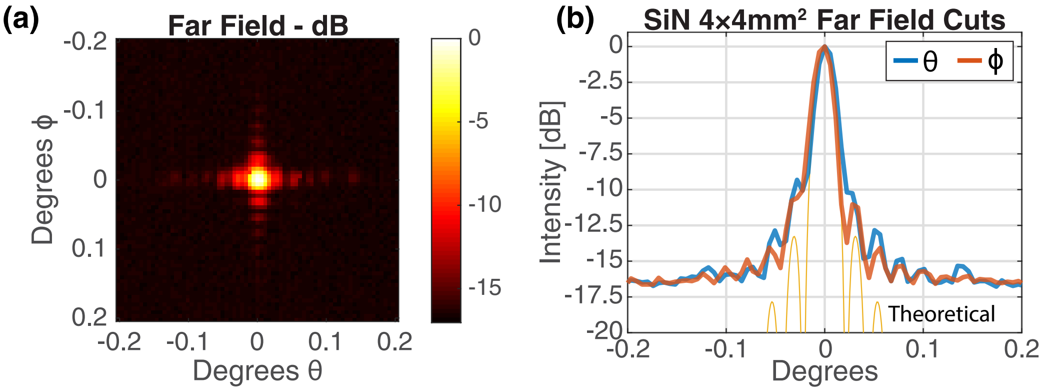

Figure 5-6: (a) Far field of the main beam of the silicon nitride 4×4 mm^2 phased array on a log scale. (b) Far field intensity cuts of the phased array along the array, θ, and antenna, ϕ, dimensions.

5.3 Conclusion

In conclusion, passive ultra-large-scale optical phased arrays in silicon and silicon nitride have been demonstrated. The silicon phase arrays did not have desirable performance with large phase noise in the splitter network. This was due to the high index contrast of the silicon waveguides. The low index contrast silicon nitride phased arrays performed well with a 10 dB side lobe suppression, and a clean double $sinc()$ in the far field. A near diffraction limited spot size of $0.021^\circ \times 0.021^\circ$ was achieved even without active phase tuning. This shows the fidelity of the fabrication process used. The $4 \times 4\,\mathrm{mm}^2$ phased array shown is an order of magnitude in area larger than what has been currently shown in the literature [21]. This demonstration shows the scalability of optical phased arrays and that large aperture sizes can be achieved.

Chapter 6

Phased Arrays for Visible Light Applications

The previous chapters operated at infrared wavelengths. Infrared wavelengths were originally chosen because they are eye safe at high powers, which is desirable for certain LIDAR systems. However, infrared wavelengths attenuate greatly in the presence of water, either within the atmosphere or liquid form. Therefore, LIDAR at visible wavelengths is often used for bathymetric measurements [69] and atmospheric measurements [70]. Furthermore, visible light projection has applications in microscopy [71], optical trapping [72], and holography [73]. The goal of this chapter is to establish the basic building blocks needed for a visible photonic integrated circuit and create passive silicon nitride phased arrays at red, green, and blue wavelengths. Much of this work was in collaboration with Matthew Byrd and Manan Raval, who are also students in the Photonic Microsystems Group.

The use of silicon nitride allows for photonic integrated circuits at visible wavelength. Visible integrated photonics with silicon nitride is a relatively new field. There has been research efforts on characterizing silicon nitride waveguides within the visible domain [74] along with work on a low-loss platform complete with fiber grating couplers and MMI splitters [75]. There have also been demonstrations of high-Q ring resonators at visible wavelengths [76] along with third harmonic generation from IR to green [77]. The bandgap of silicon nitride is approximately 5 eV (248 nm), making it suitable for visible photonic integrated circuits. However, by the Lorentz dielectric material model, there is a resonance at this wavelength and a sharp increase of the real and imaginary part of the refractive index near this wavelength. Depending on the composition of the silicon nitride, this resonance can move slightly which greatly changes the refractive index and loss at visible wavelengths [74].

In order to measure the refractive index of our silicon nitride as a function of wavelength, 500 nm of silicon nitride was deposited on a silicon wafer with a 6 μm buried oxide. The index of this silicon nitride film was measured using a Metricon Model 2010 at wavelengths spanning from red to the near-IR. Unfortunately, a red laser at 633 nm was the shortest wavelength source available for this measurement, so data points could not be taken at green and blue wavelengths. The measured data, a Sellmeier equation fit, and another index of refraction curve from literature [78] are plotted in Fig. 6-1. Although the Sellmeier fit is not perfect, it should be adequate for a first iteration of visible phased array design until this index of refraction measurement can be performed directly with green and blue lasers. We chose our red, green, and blue target wavelengths to be 635 nm, 532 nm, and 445 nm, respectively. These wavelengths were chosen based on available laser sources. The predicted indices

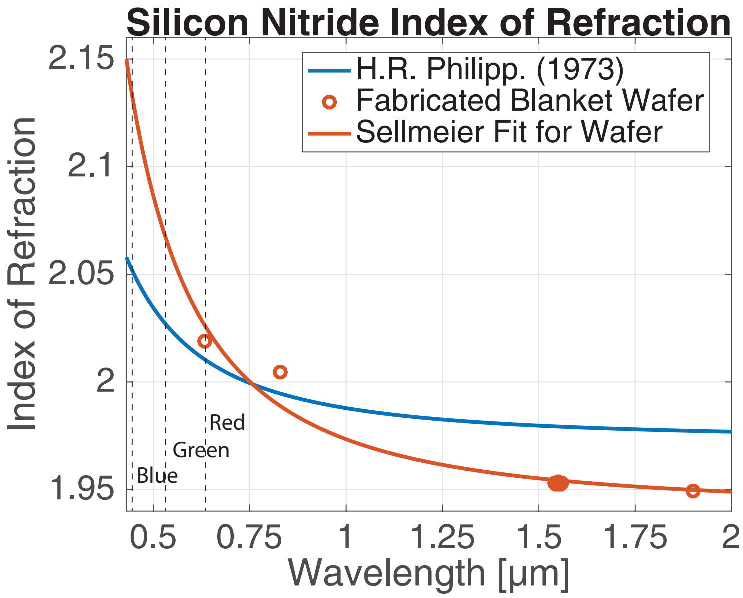

Figure 6-1: Sellmeier fit of the index of refraction of the silicon nitride used in this process.

of refraction for these wavelengths are 2.03, 2.07, and 2.13 for red, green, and blue, respectively.

6.1 On-Chip Coupling and Routing Waveguides

In order to couple visible light on chip, edge-couplers based on inverse-tapers were first investigated. This mechanism works well for telecom wavelengths [79], and was used in previous sections, but is much less effective with visible wavelengths given our silicon nitride thickness and minimum feature size. The available fabrication process has two 200 nm-thick layers of silicon nitride and a minimum feature size of 100 nm. Therefore, the smallest waveguide cross-section dimension available is $100\times200\,\mathrm{nm}^2$. Because the RGB visible wavelengths are 400-700 nm, they are still very confined within this waveguide size. For example, at a green wavelength of 532 nm, the overlap between the TE mode of this waveguide and a visible single-mode fiber (Thorlabs SM450) is 25%. One way to alleviate this issue is to use a very thin layer of silicon nitride to expand the mode. However, if the photonic circuit consists of only this thin layer of silicon nitride, the waveguides will have to be fairly wide after on-chip coupling in order to adequately confine the light. Fiber grating couplers were also investigated with promising simulation results of ∼45% efficiency with a dual layer structure. However, these were not used with the phased arrays because of the risk of crosstalk between substrate reflections and phased array outputs. Overall, it was decided to use $100\times200\,\mathrm{nm}^2$ edge-couplers for this first iteration of visible phased arrays because it presented the least risk and absolute power output of the phased arrays was not a requirement.

Routing waveguides for each wavelength were designed by ensuring that the waveguide was single-mode for TE polarized light. Fig. 6-2(a-c) shows the eigenmode simulations of the waveguide cross-section as a function of width. Waveguide widths of $0.4\,\mu$m, $0.28\,\mu$m, and $0.17\,\mu$m were chosen for the red, green, and blue wavelengths, respectively. For the green and blue waveguides, the aspect ratio is close to square, so the TE and TM modes have similar effective indices. An optimized visible waveguide

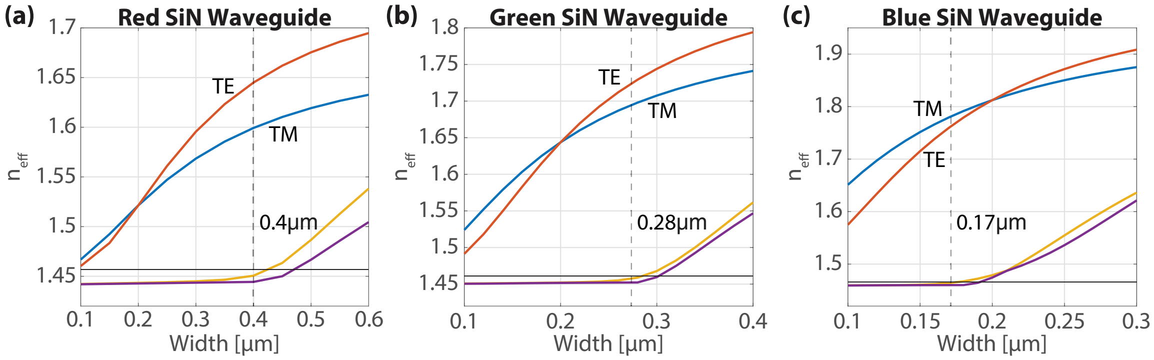

Figure 6-2: Eigenmode simulations of a single layer silicon nitride waveguide as a function of width for (a) red - 635 nm, (b) green - 532 nm, and (c) blue - 445 nm.

in silicon nitride should be thinner than the 200 nm layer available here in order to further split the effective indices of the fundamental TE and TM modes. Furthermore, for the blue wavelength, the routing waveguide is actually taller than it is wide, so the TM mode is more confined and has a higher effective index. This is unconventional for silicon photonics. The bend radius that gives a 99.9% overlap with the straight and bent mode for the chosen waveguides are 25 μm, 15 μm, and 10 μm for red, green, and blue, respectively.

6.2 Visible Splitters and Antennas

The splitter distribution network for the passive visible phased arrays was implemented similarly to the telecom passive silicon nitride arrays, that is, with a tree architecture with MMI splitters as the 1×2 splitter. MMI splitters were designed for red, green, and blue wavelengths utilizing the silicon nitride indices found in the Sellmeier fit of the refractive index. The process of designing these visible MMIs is similar to that of the telecom MMIs presented previously. These designed visible MMIs are very compact with dimensions of $7.5\times2.24\,\mu\text{m}^2$, $5.2\times1.68\,\mu\text{m}^2$, and $2.9\times1.12\,\mu\text{m}^2$ for red, green, and blue, respectively. The FDTD simulations of the MMIs are presented in Fig. 6-3(a-c). Over 99% efficiency is achieved for the red and green MMIs, whereas 98.8% is achieved for the blue MMI. The efficiency curves are also very well centered at the desired visible wavelengths.

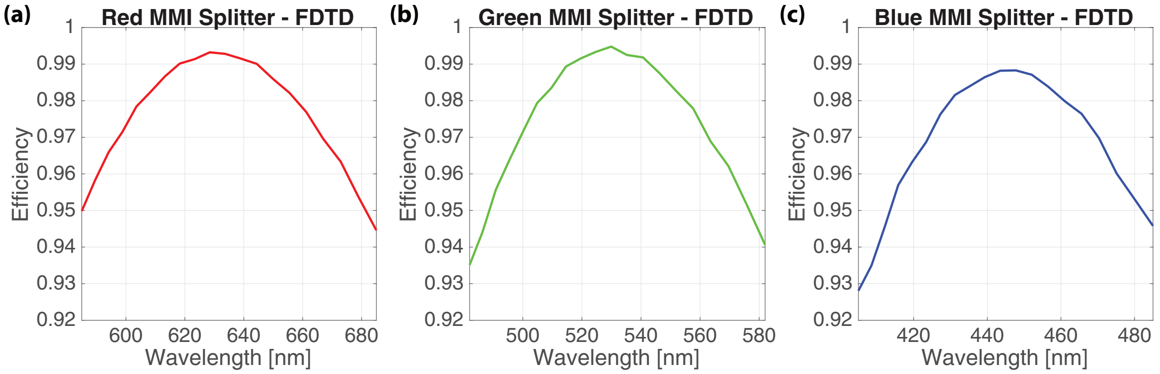

Figure 6-3: FDTD simulation of the efficiency of the (a) red, (b) green, and (c) blue MMI 1×2 splitters.

The visible antennas were designed using a similar procedure as explained previously for the telecom silicon nitride antennas. However, in this case, we did not explore the entire design space with the goal of designing uniform emitting antennas. Instead, we focused on designing antennas with a uniform perturbation (exponential emission). This was because of the uncertainty of the index of refraction for visible wavelengths making it very difficult to get the correct change of pitch as the perturbation strength changes. Having an incorrect change of pitch would be detrimental to the antenna since certain portions of the antenna would emit at different angles. With a uniform perturbation, and also uniform pitch, even if the index of refraction were to deviate slightly, the antenna would still emit at a constant angle, and thus the risk of an uncertain index of refraction would be mitigated.

Two antenna lengths for each color was designed. The goal antenna lengths were 1,000 μm/500 μm for red, 850 μm/425 μm for green, and 700 μm/350 μm for blue. The ratios of the antenna lengths of the different colors are similar to the ratio of the wavelengths of the colors. This was done so that the diffraction limited spot size of different colored arrays were similar. The perturbation strength of the antennas were designed such that 13.5% of the light was present in the waveguide at the end of the antenna (e^{-2} perturbation strength). Finally, the pitch of the antenna was designed such that the light at the goal wavelength was emitted straight upwards. A summary of the antenna designs along with the perturbations values used is shown in Tab. 6.1.

There is not a large change of perturbation between the two antenna lengths for

Color	Antenna Width	Antenna Length	Perturbation
Red (635 nm)	400 nm	1000 μm	27 nm
Red (635 nm)	400 nm	500 μm	37 nm
Green (532 nm)	280 nm	850 μm	18 nm
Green (532 nm)	280 nm	425 μm	24 nm
Blue (445 nm)	230 nm	700 μm	15 nm
Blue (445 nm)	230 nm	350 μm	20 nm

Table 6.1: Parameters of the designed visible antennas.

the green and blue wavelengths (∼5 nm). This is because the waveguide mode is very confined within the waveguide and any perturbation has a strong overlap. A thinner silicon nitride layer would result in less confinement and a less sensitive antenna to fabrication variances. Fig. 6-4(a-c) shows the far field of a portion of the shorter antenna at each wavelength.

For each wavelength, the emission pattern is centered so the main beam of a phased array should have more power than the grating lobes. However, as the wavelength shortens, a more uniform far field pattern arises. This raises the power in the grating lobes. The reason for this increasingly uniform far field pattern is that the two perturbations on the side of the waveguide are getting very close together (<200 nm for blue) and are acting much like a point source with uniform emission. In order to alleviate this issue for the shorter wavelengths in the future, a thinner nitride layer should be used such that the single-mode TE waveguide would be wider and would

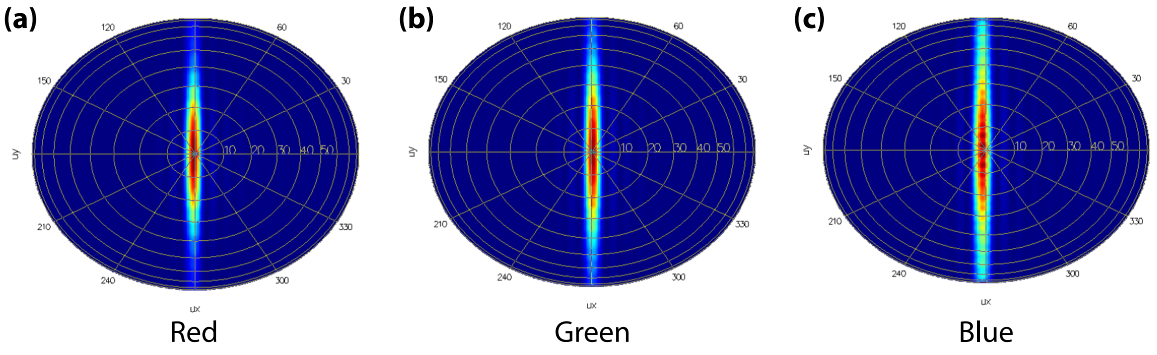

Red Green Blue

Figure 6-4: Far fields of the (a) red, (b) green, and (c) blue antennas.

allow for the perturbations to be more separated. In this way, a point-source-like emission pattern would not emerge. For a first iteration of visible phased arrays with this non-ideal silicon nitride thickness, these antennas will suffice since the far field emission is centered and we should still be able to characterize the main beam.

6.3 Experimental Results

The arrays designed in the previous section were received while writing this thesis and a full characterization could not be done. The red $0.5 \times 0.5\,\mathrm{mm}^2$ phased array is characterized below along with initial comments on the green and blue phased arrays.

Fig. 6-5(a) is an image of the $0.5 \times 0.5\,\mathrm{mm}^2$ red phased array when red light is input into the chip. The power of the input laser is increased in order to saturate the camera and to see the effect of waveguide and MMI scattering. The MMI tree is clearly seen. The light scattered from the waveguide gets weaker after every layer of the MMI tree and is near uniform within a layer. This shows that the MMI splitters are working as expected with balanced splitting. Fig. 6-5(b) shows the near field of

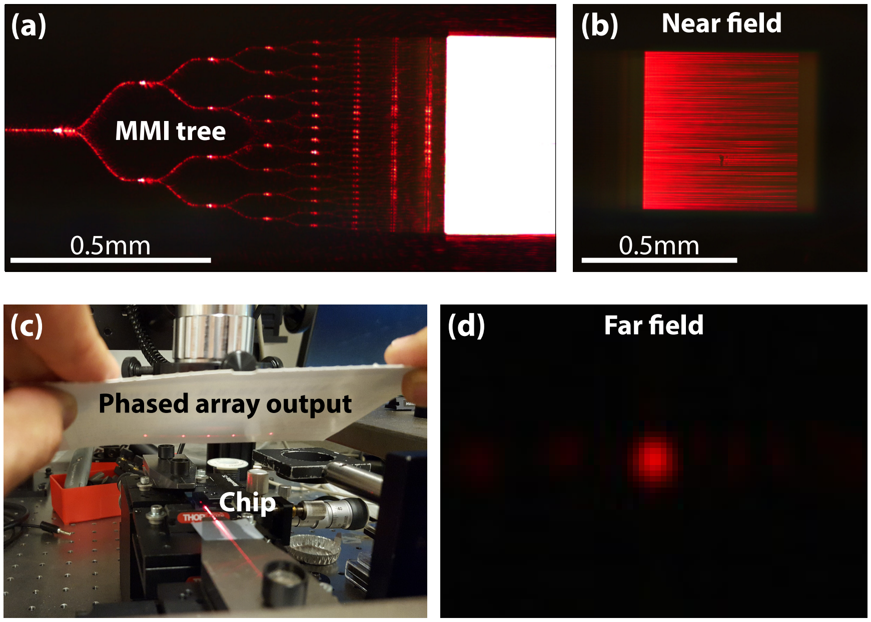

Figure 6-5: (a) Image of the red phased array with input light. (b) Non-saturated image of the near field. (c) Output of the red phased array on a white piece of paper. (d) Far field image.

the array when the camera is not saturated. As expected, exponential decay is seen throughout the antenna because of the uniform perturbation. An estimated 30% of the light remains at the end of the antenna, showing that the perturbation is weaker than designed. This was also the case in the previous section with the telecom silicon nitride arrays. Fig. 6-5(c) shows the output of the phased array. Five red spots are clearly seen on a paper card. Two additional spots emitting at ±73° on the left and the right are not shown on the card output. Finally, Fig. 6-5(d) shows the raw 2D image of the far field of the array from the RGB camera.

Fig. 6-6(a) shows a 3D image of the far field. Periodic side lobes are seen in the array dimension, but have near uniform amplitude, unlike a *sinc*() function. This is most likely because the waveguide mode at 635 nm is very confined within the silicon nitride and any fabrication noise results in a large amount of phase noise. The far field of the array was also measured with a TM polarized input and was found to have weaker side lobes. This is expected since the TM polarization is much

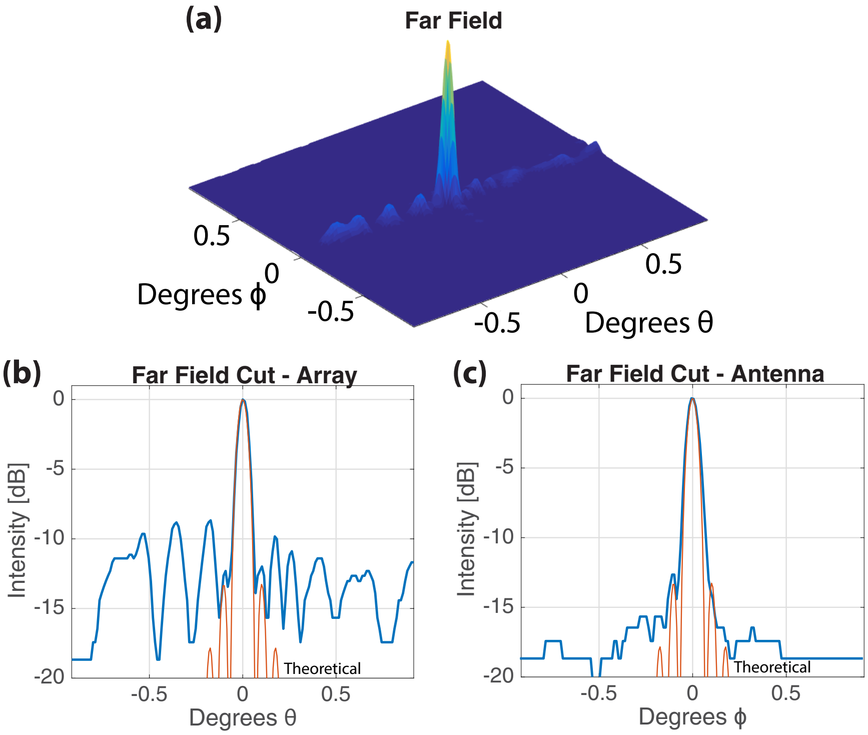

Figure 6-6: (a) 3D image of $0.5{\times}0.5\,\mathrm{mm}^2$ red array far field spot. Cuts of the far field spot in the (a) array and (b) antenna dimensions.

less confined than the TE polarization. This indicates that having a thinner nitride and a smaller waveguide will allow for a better side lobe suppression for a TE input in the future. However, for now, having clear side lobes indicates that the spot is near diffraction limited. Fig. 6-6(b-c) are intensity cuts in the antenna and array dimensions, respectively. A side lobe suppression of 8.7 dB was measured in the array dimension. In the antenna dimension, the side lobe intensities match closely with theory. A FWHM spot size of $0.064° \times 0.074°$ was measured. A spot size of $0.063° \times 0.063°$ is diffraction limited. As expected from the far field, the spot in the array dimension is near diffraction limited. The reason for the increase of spot size in the antenna dimension is because the antennas had a uniform perturbation and thus emit an exponential pattern.

The phased arrays designed at green wavelengths were measured but the coupling efficiency at green was found to be very low. This was because of the mode mismatch between the input fiber and the inverse-taper edge-coupler. This made the green phased arrays difficult to measure accurately. At the time of writing this thesis, a free-space coupling setup was being prepared to help improve the coupling efficiency. Overall, the green phased arrays did output spots in the far field, but currently around the same level of the noise caused by the reflections from the chip facet. We believe that these phased arrays have the possibility of working as designed, but unfortunately, the final experimental results will not be covered here because of lack of time to free-space couple.

Finally, the blue phased arrays were tested but it was found that the silicon nitride used was absorptive at blue wavelengths. Measurements of waveguide loss were not able to be taken because of lack of a power meter within this wavelength band. In the future, the stoichiometric ratio of the silicon and nitride can be altered in the silicon nitride layer to move the bandgap of the film, and reduce the absorption at blue wavelengths [74].

6.4 Conclusion

In conclusion, optical phased arrays at visible wavelengths have been shown, with experimental results at a red wavelength. These phased arrays are the first large-scale visible phased arrays and brings large-scale photonics to the visible spectrum. The red wavelength $0.5\times0.5\,\mathrm{mm}^2$ phased array worked well with clean near and far fields, and was almost diffraction limited with a spot size of $0.064^\circ\times0.074^\circ$. The green phased arrays are believed to be working, but clean images were difficult to take because of the low coupling efficiency. In the future, the coupling efficiency at green wavelengths can be increased by using fiber grating couplers instead of edge-couplers. Finally, within our fabrication process, blue wavelengths are absorbed but this can be mitigated in the future by changing the nitride composition.

Chapter 7

Thesis Conclusion

The work in this thesis demonstrates LIDAR on a chip for the first time. The LIDAR systems shown in the thesis use a coherent detection method: frequency-modulated continuous-wave LIDAR. This method utilizes coherent mixing of the received signal and an on-chip local oscillator in order to boost the power of the observed signal. This allowed for the use of modest germanium photodetectors. The initial system shown employed triangular frequency modulation which allowed for simultaneous distance and velocity measurements with a 2 m range and a resolution of 20 mm. Frequency modulation was achieved by modulating the injection current of an off-chip laser diode. In future work, on-chip tunable lasers should be employed. After the demonstration of this system, optical phased arrays were used as a transmitter and receiver in a LIDAR system. The optical phased arrays here utilized a grouped cascaded phase shifter architecture for simple control. This phased array was shown to have a 46°×36° steering range. This is the first demonstration of a coherent LIDAR system based on optical phased arrays.

In order to increase the performance of this LIDAR on a chip system, the input power and the receiver aperture size must be increased. Looking towards this, this thesis also showed large-scale silicon nitride phased arrays for the first time. These devices were investigated in order to achieve high input powers since silicon nitride is not limited by two-photon absorption. These passive arrays worked very successfully with a main beam power level of 520 mW. Furthermore, aperture sizes up to $4 \times 4\,\mathrm{mm}^2$

were demonstrated with a record spot size of 0.021°×0.021° and a side lobe suppression of 10 dB. This demonstration shows the scalability of optical phased arrays and the diffraction limited performance indicates that even larger apertures are possible.

Finally, visible one-dimensional phased arrays were shown in this thesis for the first time. Near diffraction limited performance was achieved in a $0.5\times0.5\,\mathrm{mm}^2$ phased array at a red wavelength. This is significant because it indicates that large-scale silicon photonics can be achieved in the visible spectrum. The fabrication tolerances for phase coherency in visible phased array structures are much more constricting than for telecom wavelengths. These structures showed the fidelity of our fabrication process and that large-scale visible phased arrays are possible. However, future work will need to be done to lower the absorption of blue wavelengths in the silicon nitride waveguides. Overall, we see visible phased array systems to be very useful for holography applications, and is an exciting emerging field.

In future LIDAR on a chip work, silicon-nitride-on-silicon transmitting phased arrays will allow for high transmission powers. The photodetectors used in future systems should also be designed to allow for a high input power without photocurrent saturation. This will allow for a large local oscillator that ensures that the system is shot noise limited and further boosts the received signal. Because the beat frequency between the received signal and the local oscillator is relatively low, high-speed operation of the high-power photodetectors is not needed.

Thermal phase shifting was primarily used throughout this thesis, but in the future, it is not obvious if thermal phase shifting is a scalable mechanism. Our antenna count is starting to reach to over one thousand antennas, which puts pressure on lowering the power consumption of the phase shifter. Furthermore, thermal crosstalk from the phase shifters was an issue of the LIDAR system shown and may be problematic in the future. Future work must do a detailed analysis of possible phase shifting mechanisms. Plasma-dispersion phase shifting or some other non-linear based phase shifting may lower the power consumption and also allow for high-speed beam steering.

Bibliography

[1] J. Lalonde, N. V., D. F. Huber, and M. Hebert, “Natural terrain classification using three-dimensional ladar data for ground robot mobility,” Journal of Field Robotics **23**, 839–861 (2006).

[2] J. Levinson, J. Askeland, J. Becker, J. Dolson, D. Held, S. Kammel, J. Z. Kolter, D. Langer, O. Pink, V. Pratt, M. Sokolsky, G. Stanek, D. Stavens, A. Teichman, M. Werling, and S. Thrun, “Towards fully autonomous driving: Systems and algorithms,” Intelligent Vehicles Symposium (IV), 2011 IEEE pp. 163–168 (2011).

[3] Y. Lin, J. Hyyppa, and A. Jaakkola, “Mini-UAV-Borne LIDAR for Fine-Scale Mapping,” IEEE Geoscience and Remote Sensing Letters **8**, 426–430 (2011).

[4] J. Shackleton, B. VanVoorst, and J. Hesch, “Tracking People with a 360-Degree Lidar,” Advanced Video and Signal Based Surveillance (AVSS), 2010 Seventh IEEE International Conference on pp. 420–426 (2010).

[5] M. Himmelsbach, A. Müller, T. Luettel, and H.-J. Wünsche, “LIDAR-based 3D object perception,” Proceedings of 1st international workshop on cognition for technical systems **1** (2008).

[6] A. G. Stove, “Linear FMCW radar techniques,” IEE Proceedings - Radar and Signal Processing **139**, 343–350 (1992).

[7] D. Pierrottet, F. Amzajerdian, L. Petway, B. Barnes, G. Lockard, and M. Rubio, “Linear FMCW laser radar for precision range and vector velocity measurements,” MRS Proceedings **1076**, 1076–K04 (2008).

[8] B. F. Aull, “Silicon Geiger-mode avalanche photodiode arrays for photon-starved imaging,” Proc. SPIE **9492**, 94920M–94920M–9 (2015).

[9] C. J. Grund and E. W. Eloranta, “University of Wisconsin High Spectral Resolution Lidar,” Optical Engineering **30**, 6–12 (1991).

[10] B. Schwarz, “LIDAR: Mapping the world in 3D,” Nature Photonics **4**, 429–430 (2010).

[11] E. Timurdogan, C. M. Sorace-Agaskar, J. Sun, E. S. Hosseini, A. Biberman, and M. R. Watts, “An ultralow power athermal silicon modulator,” Nature communications **5** (2014).

[12] D. Patel, S. Ghosh, M. Chagnon, A. Samani, V. Veerasubramanian, M. Osman, and D. V. Plant, “Design, analysis, and transmission system performance of a 41 GHz silicon photonic modulator,” Opt. Express **23**, 14263–14287 (2015).

[13] P. Dong, X. Liu, S. Chandrasekhar, L. L. Buhl, R. Aroca, and Y. K. Chen, “Monolithic Silicon Photonic Integrated Circuits for Compact 100+Gb/s Coherent Optical Receivers and Transmitters,” IEEE Journal of Selected Topics in Quantum Electronics **20**, 150–157 (2014).

[14] C. R. Doerr, L. Chen, T. Nielsen, R. Aroca, L. Chen, M. Banaee, S. Azemati, G. McBrien, S. Y. Park, J. Geyer, B. Guan, B. Mikkelsen, C. Rasmussen, M. Givhechi, Z. Wang, B. Potsaid, H.-C. Lee, E. Swanson, and J. Fujimoto, “O, E, S, C, and L Band Silicon Photonics Coherent Modulator/Receiver,” Optical Fiber Communication Conference Postdeadline Papers p. Th5C.4 (2016).

[15] C. Zhang, S. Zhang, J. D. Peters, and J. E. Bowers, “8×8×40 Gbps fully integrated silicon photonic network on chip,” Optica **3**, 785–786 (2016).

[16] K. V. Acoleyen, W. Bogaerts, J. Jágerská, N. L. Thomas, R. Houdré, and R. Baets, “Off-chip beam steering with a one-dimensional optical phased array on silicon-on-insulator,” Opt. Lett. **34**, 1477–1479 (2009).

[17] J. Sun, E. Timurdogan, A. Yaacobi, E. S. Hosseini, and M. R. Watts, “Large-scale nanophotonic phased array,” Nature **493**, 195–199 (2013).

[18] J. Hulme, J. Doylend, M. Heck, J. Peters, M. Davenport, J. Bovington, L. Coldren, and J. Bowers, “Fully integrated hybrid silicon two dimensional beam scanner,” Optics express **23**, 5861–5874 (2015).

[19] H. Abediasl and H. Hashemi, “Monolithic optical phased-array transceiver in a standard SOI CMOS process,” Opt. Express **23**, 6509–6519 (2015).

[20] F. Aflatouni, B. Abiri, A. Rekhi, and A. Hajimiri, “Nanophotonic projection system,” Opt. Express **23**, 21012–21022 (2015).

[21] D. N. Hutchison, J. Sun, J. K. Doylend, R. Kumar, J. Heck, W. Kim, C. T. Phare, A. Feshali, and H. Rong, “High-resolution aliasing-free optical beam steering,” Optica **3**, 887–890 (2016).

[22] E. Timurdogan, Z. Su, K. Settaluri, S. Lin, S. Moazeni, C. Sun, G. Leake, D. D. Coolbaugh, B. Moss, M. Moresco, V. Stojanovič, and M. R. Watts, “An Ultra Low Power 3D Integrated Intra-Chip Silicon Electronic-Photonic Link,” Optical Fiber Communication Conference Post Deadline Papers p. Th5B.8 (2015).

[23] C. Sun, M. T. Wade, Y. Lee, J. S. Orcutt, L. Alloatti, M. S. Georgas, A. S. Waterman, J. M. Shainline, R. R. Avizienis, S. Lin, B. R. Moss, R. Kumar, F. Pavanello, A. H. Atabaki, H. M. Cook, A. J. Ou, J. C. Leu, Y.-H. Chen, K. Asanovic, R. J. Ram, M. A. Popovic, and V. M. Stojanovic, "Single-chip microprocessor that communicates directly using light," Nature **528**, 534–538 (2015).

[24] S. Emami, R. F. Wiser, E. Ali, M. G. Forbes, M. Q. Gordon, X. Guan, S. Lo, P. T. McElwee, J. Parker, J. R. Tani *et al.*, "A 60GHz CMOS phased-array transceiver pair for multi-Gb/s wireless communications," 2011 IEEE International Solid-State Circuits Conference pp. 164–166 (2011).

[25] D. Detrick and T. Rosenberg, "A phased-array radiowave imager for studies of cosmic noise absorption," Radio Science **25**, 325–338 (1990).

[26] E. Brookner, "Phased-array radars," Scientific American **252**, 94–102 (1985).

[27] A. J. Fenn, D. H. Temme, W. P. Delaney, and W. E. Courtney, "The development of phased-array radar technology," Lincoln Laboratory Journal **12**, 321–340 (2000).

[28] F. Boeuf, S. Cremer, E. Temporiti, M. Fere', M. Shaw, N. Vulliet, bastien orlando, D. Ristoiu, A. Farcy, T. Pinguet, A. Mekis, G. Masini, P. Sun, Y. Chi, H. Petiton, S. Jan, J.-R. Manouvrier, C. Baudot, P. Le-Maitre, J. F. Carpentier, L. Salager, M. Traldi, L. Maggi, D. Rigamonti, C. Zaccherini, C. Elemi, B. Sautreuil, and L. Verga, "Recent Progress in Silicon Photonics R&D and Manufacturing on 300mm Wafer Platform," Optical Fiber Communication Conference p. W3A.1 (2015).

[29] G. H. Duan, C. Jany, A. L. Liepvre, A. Accard, M. Lamponi, D. Make, P. Kaspar, G. Levaufre, N. Girard, F. Lelarge, J. M. Fedeli, A. Descos, B. B. Bakir, S. Messaoudene, D. Bordel, S. Menezo, G. de Valicourt, S. Keyvaninia, G. Roelkens, D. V. Thourhout, D. J. Thomson, F. Y. Gardes, and G. T. Reed, "Hybrid III–V on Silicon Lasers for Photonic Integrated Circuits on Silicon," IEEE Journal of Selected Topics in Quantum Electronics **20**, 158–170 (2014).

[30] E. S. Hosseini, Purnawirman, J. D. B. Bradley, J. Sun, G. Leake, T. N. Adam, D. D. Coolbaugh, and M. R. Watts, "CMOS-compatible 75mW erbium-doped distributed feedback laser," Opt. Lett. **39**, 3106–3109 (2014).

[31] H. Chen, P. Verheyen, P. De Heyn, G. Lepage, J. De Coster, S. Balakrishnan, P. Absil, W. Yao, L. Shen, G. Roelkens *et al.*, "-1 V bias 67 GHz bandwidth Si-contacted germanium waveguide pin photodetector for optical links at 56 Gbps and beyond," Optics Express **24**, 4622–4631 (2016).

[32] A. Yaacobi, J. Sun, M. Moresco, G. Leake, D. Coolbaugh, and M. R. Watts, "Integrated phased array for wide-angle beam steering," Opt. Lett. **39**, 4575–4578 (2014).

[33] R. Waldhäusl, B. Schnabel, P. Dannberg, E.-B. Kley, A. Bräuer, and W. Karthe, “Efficient Coupling into Polymer Waveguides by Gratings,” Appl. Opt. **36**, 9383–9390 (1997).

[34] M. Born and E. Wolf, “Principles of optics: electromagnetic theory of propagation, interference and diffraction of light,” (2000).

[35] J. Komma, C. Schwarz, G. Hofmann, D. Heinert, and R. Nawrodt, “Thermo-optic coefficient of silicon at 1550nm and cryogenic temperatures,” Applied Physics Letters **101**, 041905 (2012).

[36] R. Soref and B. Bennett, “Electrooptical effects in silicon,” IEEE Journal of Quantum Electronics **23**, 123–129 (1987).

[37] M. A. Itzler, U. Krishnamachari, M. Entwistle, X. Jiang, M. Owens, and K. Slomkowski, “Dark Count Statistics in Geiger-Mode Avalanche Photodiode Cameras for 3-D Imaging LADAR,” IEEE Journal of Selected Topics in Quantum Electronics **20**, 318–328 (2014).

[38] D. B. Cole, C. Sorace-Agaskar, M. Moresco, G. Leake, D. Coolbaugh, and M. R. Watts, “Integrated heterodyne interferometer with on-chip modulators and detectors,” Opt. Lett. **40**, 3097–3100 (2015).

[39] T. A. Ramadan, R. Scarmozzino, and R. M. Osgood, “Adiabatic couplers: design rules and optimization,” Journal of Lightwave Technology **16**, 277–283 (1998).

[40] M.-C. Amann, T. Bosch, M. Lescure, R. Myllyla, and M. Rioux, “Laser ranging: a critical review of usual techniques for distance measurement,” Optical engineering **40**, 10–19 (2001).

[41] Y. Jiang, B. Deng, H. Wang, Y. Qin, and K. Liu, “An Effective Nonlinear Phase Compensation Method for FMCW Terahertz Radar,” IEEE Photonics Technology Letters **28**, 1684–1687 (2016).

[42] D. E. Wahl, P. H. Eichel, D. C. Ghiglia, and C. V. Jakowatz, “Phase gradient autofocus-a robust tool for high resolution SAR phase correction,” IEEE Transactions on Aerospace and Electronic Systems **30**, 827–835 (1994).

[43] A. Anghel, G. Vasile, R. Cacoveanu, C. Ioana, and S. Ciochina, “Nonlinearity correction algorithm for wideband FMCW radars,” 21st European Signal Processing Conference (EUSIPCO 2013) pp. 1–5 (2013).

[44] M. Nöding and M.-C. Amann, “FMCW-lidar with widely tunable laser diodes: influence of the tuning behaviour on the distance measurement,” Journal of Optics **29**, 212 (1998).

[45] N. Satyan, A. Vasilyev, G. Rakuljic, V. Leyva, and A. Yariv, “Precise control of broadband frequency chirps using optoelectronic feedback,” Opt. Express **17**, 15991–15999 (2009).

[46] P. Sandborn, N. Quack, N. Hoghooghi, J. B. Chou, J. Ferrara, S. Gambini, B. Behroozpour, L. Zhu, B. Boser, C. Chang-Hasnain, and M. C. Wu, “Linear Frequency Chirp Generation Employing Optoelectronic Feedback Loop andIntegrated Silicon Photonics,” CLEO: 2013 p. CTu2G.5 (2013).

[47] K. Iiyama, L.-T. Wang, and K.-I. Hayashi, “Linearizing optical frequency-sweep of a laser diode for FMCW reflectometry,” Journal of Lightwave Technology **14**, 173–178 (1996).

[48] J. Sun, “Toward accurate and large-scale silicon photonics,” MIT PhD Thesis (2013).

[49] D. Kwong, A. Hosseini, J. Covey, Y. Zhang, X. Xu, H. Subbaraman, and R. T. Chen, “On-chip silicon optical phased array for two-dimensional beam steering,” Opt. Lett. **39**, 941–944 (2014).

[50] J. Doylend, M. R. Heck, J. Bovington, J. Peters, L. Coldren, and J. Bowers, “Free-space Beam Steering in Two Dimensions Using a Silicon Optical Phased Array,” Optical Fiber Communication Conference p. OM2J.1 (2012).

[51] S. V. Deshpande, E. Gulari, S. W. Brown, and S. C. Rand, “Optical properties of silicon nitride films deposited by hot filament chemical vapor deposition,” Journal of Applied Physics **77** (1995).

[52] K. Ikeda, R. E. Saperstein, N. Alic, and Y. Fainman, “Thermal and Kerr nonlinear properties of plasma-deposited silicon nitride/silicon dioxide waveguides,” Opt. Express **16**, 12987–12994 (2008).

[53] D. T. H. Tan, K. Ikeda, P. C. Sun, and Y. Fainman, “Group velocity dispersion and self phase modulation in silicon nitride waveguides,” Applied Physics Letters **96**, 061101 (2010).

[54] A. Gondarenko, J. S. Levy, and M. Lipson, “High confinement micron-scale silicon nitride high Q ring resonator,” Opt. Express **17**, 11366–11370 (2009).

[55] J. F. Bauters, M. J. R. Heck, D. D. John, J. S. Barton, C. M. Bruinink, A. Leinse, R. G. Heideman, D. J. Blumenthal, and J. E. Bowers, “Planar waveguides with less than 0.1 dB/m propagation loss fabricated with wafer bonding,” Opt. Express **19**, 24090–24101 (2011).

[56] L. Wang, L. Chang, N. Volet, M. H. P. Pfeiffer, M. Zervas, H. Guo, T. J. Kippenberg, and J. E. Bowers, “Frequency comb generation in the green using silicon nitride microresonators,” Laser and Photonics Reviews **10**, 631–638 (2016).

[57] Y. Okawachi, K. Saha, J. S. Levy, Y. H. Wen, M. Lipson, and A. L. Gaeta, “Octave-spanning frequency comb generation in a silicon nitride chip,” Opt. Lett. **36**, 3398–3400 (2011).

[58] A. Dutt, S. Miller, K. Luke, J. Cardenas, A. L. Gaeta, P. Nussenzveig, and M. Lipson, "Tunable squeezing using coupled ring resonators on a silicon nitride chip," Opt. Lett. **41**, 223–226 (2016).

[59] A. Arbabi and L. L. Goddard, "Measurements of the refractive indices and thermo-optic coefficients of Si3N4 and SiOx using microring resonances," Opt. Lett. **38**, 3878–3881 (2013).

[60] A. Hosseini, D. Kwong, C.-Y. Lin, B. S. Lee, and R. T. Chen, "Output Formulation for Symmetrically Excited One-to-Multimode Interference Coupler," IEEE Journal of Selected Topics in Quantum Electronics **16**, 61–69 (2010).

[61] S. H. Tao, Q. Fang, J. F. Song, M. B. Yu, G. Q. Lo, and D. L. Kwong, "Cascade wide-angle Y-junction 1 × 16 optical power splitter based on silicon wire waveguides on silicon-on-insulator," Opt. Express **16**, 21456–21461 (2008).

[62] L. B. Soldano and E. C. M. Pennings, "Optical multi-mode interference devices based on self-imaging: principles and applications," Journal of Lightwave Technology **13**, 615–627 (1995).

[63] J. Notaros, F. Pavanello, M. T. Wade, C. Gentry, A. Atabaki, L. Alloatti, R. J. Ram, and M. Popovic, "Ultra-Efficient CMOS Fiber-to-Chip Grating Couplers," Optical Fiber Communication Conference p. M2I.5 (2016).

[64] W. D. Sacher, Y. Huang, L. Ding, B. J. F. Taylor, H. Jayatilleka, G.-Q. Lo, and J. K. S. Poon, "Wide bandwidth and high coupling efficiency Si3N4-on-SOI dual-level grating coupler," Opt. Express **22**, 10938–10947 (2014).

[65] S. Yang, Y. Zhang, T. Baehr-Jones, and M. Hochberg, "High efficiency germanium-assisted grating coupler," Opt. Express **22**, 30607–30612 (2014).

[66] J. D. B. Bradley and E. S. Hosseini, "Monolithic erbium- and ytterbium-doped microring lasers on silicon chips," Opt. Express **22**, 12226–12237 (2014).

[67] W. D. Sacher, Y. Huang, G.-Q. Lo, and J. K. S. Poon, "Multilayer Silicon Nitride-on-Silicon Integrated Photonic Platforms and Devices," J. Lightwave Technol. **33**, 901–910 (2015).

[68] Y. Zhang, S. Yang, A. E.-J. Lim, G.-Q. Lo, C. Galland, T. Baehr-Jones, and M. Hochberg, "A compact and low loss Y-junction for submicron silicon waveguide," Opt. Express **21**, 1310–1316 (2013).

[69] C.-K. Wang and W. D. Philpot, "Using airborne bathymetric lidar to detect bottom type variation in shallow waters," Remote Sensing of Environment **106**, 123–135 (2007).

[70] K. W. Fischer, V. J. Abreu, W. R. Skinner, J. E. Barnes, M. J. McGill, and T. D. Irgang, "Visible wavelength Doppler lidar for measurement of wind and aerosol profiles during day and night," Optical Engineering **34**, 499–511 (1995).

[71] J. Wu, X. Cui, G. Zheng, Y. M. Wang, L. M. Lee, and C. Yang, “Wide field-of-view microscope based on holographic focus grid illumination,” Opt. Lett. **35**, 2188–2190 (2010).

[72] E. R. Dufresne and D. G. Grier, “Optical tweezer arrays and optical substrates created with diffractive optics,” Review of scientific instruments **69**, 1974–1977 (1998).

[73] D. Fattal, Z. Peng, T. Tran, S. Vo, M. Fiorentino, J. Brug, and R. G. Beausoleil, “A multi-directional backlight for a wide-angle, glasses-free three-dimensional display,” Nature **495**, 348–351 (2013).

[74] A. Gorin, A. Jaouad, E. Grondin, V. Aimez, and P. Charette, “Fabrication of silicon nitride waveguides for visible-light using PECVD: a study of the effect of plasma frequency on optical properties,” Opt. Express **16**, 13509–13516 (2008).

[75] S. Romero-García, F. Merget, F. Zhong, H. Finkelstein, and J. Witzens, “Silicon nitride CMOS-compatible platform for integrated photonics applications at visible wavelengths,” Opt. Express **21**, 14036–14046 (2013).

[76] E. S. Hosseini, S. Yegnanarayanan, A. H. Atabaki, M. Soltani, and A. Adibi, “High Quality Planar Silicon Nitride Microdisk Resonators for Integrated Photonics in the VisibleWavelength Range,” Opt. Express **17**, 14543–14551 (2009).

[77] J. S. Levy, M. A. Foster, A. L. Gaeta, and M. Lipson, “Harmonic generation in silicon nitride ring resonators,” Opt. Express **19**, 11415–11421 (2011).

[78] H. R. Philipp, “Optical properties of silicon nitride,” Journal of the Electrochemical Society **120**, 295–300 (1973).

[79] V. R. Almeida, R. R. Panepucci, and M. Lipson, “Nanotaper for compact mode conversion,” Opt. Lett. **28**, 1302–1304 (2003).